TARSUS
UNIVERSITY

T.R.

TARSUS UNIVERSITY

SCHOOL OF GRADUATE STUDIES

DEPARTMENT OF MECHANICAL ENGINEERING

THE IMPACT OF CHANGING OBSTACLE SIZES ON SHOCK WAVE GENERATION FOR VARIOUS FUEL TYPES IN DETONATION ENGINES

MEHMET ALİ ADIGÜZEL

MASTER THESIS

TARSUS – 2023

T.R.

TARSUS UNIVERSITY

SCHOOL OF GRADUATE STUDIES

DEPARTMENT OF MECHANICAL ENGINEERING

THE IMPACT OF CHANGING OBSTACLE SIZES ON SHOCK WAVE GENERATION FOR VARIOUS FUEL TYPES IN DETONATION ENGINES

MEHMET ALİ ADIGÜZEL

Supervisor: Assoc. Prof. Ahmet Alper YONTAR

MASTER THESIS

TARSUS – 2023

To the Directorate of School of Graduate Studies of Tarsus University;

This study has been accepted by the jury as a MASTER'S THESIS in the Department of Mechanical Engineering.

Chair: Assoc. Prof. Ahmet Alper YONTAR

(Supervisor)

Member: Assoc. Prof.

Member: Assoc. Prof.

The above jury decision has been approved by the School of Graduate Studies Board with the decision dated .../.../2023 and numbered ...../....

CONFIRMATION

I confirm that the signatures above belong to the mentioned faculty members.

Date: .../.../2023

Prof. Dr. Osman Murat ÖZKENDİR
Director of the Institute

NOTE: The unauthorized use of citations, tables, figures, and photographs from other sources without proper referencing is subject to the provisions of Law No. 5846 on Intellectual and Artistic Works in this thesis.

ETHICS DECLARATION

In this thesis work that I have prepared in accordance with the Rules of Thesis Writing of Tarsus University School of Graduate Studies:

- I have obtained all the data, information, and documents presented in the thesis in accordance with academic and ethical rules.
- I have presented all information, documents, evaluations, and results in accordance with scientific ethics and moral rules.
- I have properly cited and referenced all the works I have used in the thesis.
- I have not made any alterations to the data used and the results obtained.
- I declare that the work presented in this thesis is original.

I acknowledge that any violation of the above statements may result in the loss of my rights.

.../.../20...

SIGNATURE

Mehmet Ali ADIGÜZEL

ÖZET

DETONASYON MOTORLARINDA ENGEL BOYUTLARI DEĞİŞİMİNİN FARKLI YAKIT TÜRLERİ İÇİN ŞOK DALGASI OLUŞUMUNA ETKİSİ

MEHMET ALİ ADIGÜZEL

Yüksek Lisans, Makine Mühendisliği Ana Bilim Dalı

Danışman: Doç Dr. Ahmet Alper YONTAR

Haziran 2023, 128 sayfa

Bu yüksek lisans tez çalışması kapsamında teorik olarak daha yüksek verime sahip olduğu kanıtlanmış detonasyon motorlarının teorik olarak araştırılması ve HAD analizleri ile bu teorik verilerin desteklenmesi amaçlanmıştır. Detonasyon motorları iki ana bileşen altında incelenmektedir. Bunlardan biri ön-detonatör bir diğeri ise ana-detonatördür. Ön-detonatör detonasyon motorunun şok başlatıcısı olarak kullanılır. Ön-detonatör iki bölümden oluşmaktadır. Bunlardan birincisi yüksek basınç ve sıcaklığa sahip olan sürücü bölgesi, ikincisi ise yanmamış yakıt ve havanın bulunduğu sürünen bölgedir.

Bu tez kapsamında, gaz fazındaki asetilen, etilen, etan, metan, kerosen ve hidrojen yakıtı, 3 farklı ekivalans ve 5 farklı blokaj oranında ön-detonatörde şok dalgası oluşturmak için kullanılmıştır. Geometri içerisinde yanma sonucunda oluşan şok dalgasının yüksek basınç ve sıcaklıklara ulaşması viskoziteyi arttırmaktadır. Viskozitesi artan gazın, Reynolds sayısı dolayısıyla hız değeri azalmaktadır. Ön-detonatörde, gazın viskozitesi nedeniyle azalan hızın yükseltilmesi amacıyla geometri içerisine farklı yüksekliklerde ve genişliklerde (0.5-0.75-1-1.25-1.5) türbülans arttırıcı engeller yerleştirilmiştir. Türbülanslı bu yapının gaz karışımının homojenliğini arttırdığı, bunun sonucunda da engellerin şok dalgasının oluşma süresini kısalttığı tespit edilmiştir.

Tez kapsamında farklı blokaj oranlarına sahip geometrilerin basınç, sıcaklık, hız ve şok dalgasının oluşum süresi gibi parametreler üzerindeki etkileri incelenmiştir. Analizler bilgisayar destekli hesaplama programına kodlanarak farklı blokaj oranlarında otomatik olarak gerçekleştirilmiştir. Elde edilen veriler daha sonra grafikler ve konturlar ile yorumlanmıştır. Yapılan çalışmalar ışığında ön-detonatör tasarımları yapmak kolaylaştırılmıştır. Ön-detonatör çıkışında elde edilen şok dalgası ana-detonatorde beslenerek şok dalgasının sürekliliğinin sağlanmasında bir yaklaşım geliştirilmiştir.

Bu tez kapsamında, yakıt püskürtme süreci ile ilgili enjektör tasarımı, enjektör sayısı ve enjektör konumlandırmaları ile ilgili ön tasarım çalışmaları da gerçekleştirilmiştir. Bu çalışmalar çift faz akış göz önüne alınarak hesaplanmıştır. Çift fazlı akış olması detonasyon motorunun yüksek ısı akısı ve sıcaklığı göz önüne alındığında motorun soğutulması işleminde avantaj olacaktır. Tasarlanan enjektörlerin analizleri 2D ve 3D koşullarda UDF kullanılarak HAD programınca gerçekleştirilmiştir.

Bu tez kapsamında isterler doğrultusunda ön-detonatör ve ana-detonatörün tasarımı

için bir yaklaşım geliştirilmiş ve çalışmalarda kullanılması adına bilimsel literatüre kazandırılmıştır. Bu verilerden faydalanarak geliştirilebilecek detonasyon motorları ile ülkemiz uzay ve havacılık sanayisine araştırma-geliştirme faaliyetleri kapsamında destek sağlanmış olacaktır. Çalışma kapsamında sunulan veriler ışığında deflegrasyon dalgasının detonasyon dalgasına dönüşüm süreçlerinde fiziksel ve kimyasal parametrelerin etkileri üzerine sunulan veriler alev temelli çalışmaların gelişimi açısından önem arz etmektedir.

Anahtar Kelimeler: Atımlı Detonasyon Motorları, Dönel Detonasyon Motorları, Roket Motorları, Alev Dalgasından Patlamaya Geçiş

ABSTRACT

THE IMPACT OF CHANGING OBSTACLE SIZES ON SHOCK WAVE GENERATION FOR VARIOUS FUEL TYPES IN DETONATION ENGINES

MEHMET ALİ ADIGÜZEL

Master Thesis, Department of Mechanical Engineering

Supervisor: Assoc. Prof. Ahmet Alper YONTAR

July 2023, 128 pages

In this master's thesis, the focus is on the theoretical investigation of detonation engines, which have been proven to have higher efficiency, and supporting these theoretical findings with CFD (Computational Fluid Dynamics) analyses. The study examines two main components of detonation engines: the pre-detonator and the main-detonator. The pre-detonator plays the role of a shock initiator for the detonation engine, comprising two sections: the driver region characterized by high pressure, temperature, and the driven region containing unburned fuel and air.

In this thesis, gaseous fuels such as acetylene, ethylene, ethane, methane, kerosene, and hydrogen were used to generate a shockwave in a pre-detonator under three different equivalence ratios and five different blockage ratios. The shock wave resulting from combustion within the geometry leads to elevated pressures and temperatures, thereby increasing viscosity. As the viscosity of the gas increases, it reduces the Reynolds number and, consequently, the velocity. Turbulence-enhancing obstacles were placed within the geometry at different heights and widths (0.5-0.75-1-1.25-1.5) to increase the reduced velocity due to the gas's viscosity in the pre-detonator. It was observed that this turbulent structure enhances the homogeneity of the gas mixture, thus shortening the time required for shock wave formation due to the obstacles.

The effects of geometries with different blockage ratios on parameters such as pressure, temperature, velocity, and the formation time of the shock wave were investigated within the scope of the thesis. The analyses were performed using computer-aided calculation software, automatically varying the blockage ratios. The obtained data were then interpreted using graphs and contours. Based on the conducted studies, the design of the pre-detonator was facilitated. An approach has been developed to ensure the continuity of the shock wave by feeding the pre-detonator output to the main detonator.

As part of this thesis, preliminary design work on the injector design, the number of injectors, and the injection positioning related to the fuel spraying process has also been carried out. These studies were calculated taking into account the two-phase flow. The two-phase flow would be advantageous in cooling the engine, given the high heat flow and temperature of the detonation engine. The analyses of the designed injectors were conducted using User-Defined Functions (UDF) in the CFD program under both 2D and 3D conditions.

In the context of this thesis, an approach for designing pre-detonators and main

detonators in accordance with the requirements was established and contributed to the scientific literature for use in research and development activities in the field. By using these data, our country's aerospace sector will be supported in the chassis of research and development activities for detonation engines that can be produced using this knowledge. The data reported in the chassis of the study, in light of the effects of physical and chemical parameters in the transition stages from deflagration waves to detonation waves, are significant for the advancement of flame-based research.

Keywords: Pulse Detonation Engines, Rotating Detonation Engines, Rocket Engines, Deflagration to Detonation Transition

FOREWORD

I would like to express my gratitude to my advisor, Assoc. Prof. Dr. Ahmet Alper Yontar, whose knowledge and experience have always been by my side throughout this thesis work. His positive attitude has encouraged me, and I take pride in working together and being his student. Thank you for your guidance and support.

I am also grateful to express my gratitude to Prof. Dr. Serap ŞAHİNKAYA and Assoc. Prof. Dr. Deniz Üstün, whose support has helped me elevate my thesis work to a higher level. I also extend thanks to my teacher, Ebru BOZKURT, whose belief in my abilities and encouragement have led me to this point. I am truly grateful for her guidance and support.

I am deeply grateful for extend my gratitude to my dear friends Ayşe Gizem ÖZGÜNER, Tahir AYAZ and Aşkın KİLLİ, who have been my companions on many successful journeys. I am thankful for the strength they bring with their presence. Additionally, I want to thank my mother, Yıldız ADIGÜZEL, and my father, Mehrali ADIGÜZEL, whose unwavering support has been a source of motivation for me. Lastly, I express my thanks to the entire Adıgüzel family for their encouragement and support.

CONTENTS

CHAPTER 3

MATERIAL AND METHOD

CHAPTER 4

FINDINGS

NOMENCLATURE

$\boldsymbol{M_a}$**:** Molecular Weight

0: Denotes Stagnation Condition

1: State 1, Before Detonation Wave

2: State 2, After Detonation Wave

BR: Blockage Ratio

CJ: Denotes Chapman-Jouguet Conditions

$\mathbf{C_p}$**:** Specific Heat Capacity

DDT: Deflagration to Detonation Transition

FJ: Denotes Fickett-Jacobs Cycle

M: Mach Number

P: Pressure

PDE: Pulse Detonation Engine

R: Gas Constant

RDE: Rotating Detonation Engine

T: Temperature

U: Velocity of Flow

V: Volume

$\mathbf{V_{cj}}$**:** Chapman-Jouguet Velocity

ZND: Zeldovich-Von Neumann-Doering

$\boldsymbol{\gamma}$**:** Specific Heat Ratio

$\boldsymbol{\eta_{th}}$: Thermal Efficiency

$\boldsymbol{\lambda}$**:** Detonation Cell Width

ρ: Density

Φ: Air Excess Coefficient

φ: Ekivalance Ratio

LIST OF FIGURES

Page

LIST OF TABLES

Page

APPENDIX

Page

INTRODUCTION

In the globalized world, the defence industry ranks among the top priorities of countries. The thrust force plays a significant role in the defence industry of nations. Recently, advancements in aviation and space have become a subject of competition among countries, leading to an increase in efforts and accelerating developments in the aerospace field. Rockets can be referred to as missiles, depending on their areas of application. They have high energy requirements to serve their intended purposes, ranging from space travel to emerging cargo-carrying rockets. Sustainable provision of this energy is achievable through the development of alternative fuels, improvement of manufacturing processes, or advancements in rocket cycles.

In the 1960s, the Cold War between the USA and the USSR played a significant role in the development of traditional rocket engines. The race to be the first to set foot on the moon laid the foundation for today's space exploration. After the moon landing, human curiosity did not wane, and this competition continued to drive progress. Over time, not only governments but also private companies have made advancements in this field. Currently, many countries and private companies send vehicles to planets to search for signs of life and gather geological and atmospheric information. They also deploy satellites into orbit to monitor and study various aspects of Earth, such as resource detection and tracking climate changes.

Orbiting satellites have also been utilized for potential defence or offensive observations in case of a war. Telescopes placed in space not only search for signs of life but also gather data for future space-mining endeavors. With the increasing popularity of space tourism, the achievements of various companies' efforts have accelerated research and development. Space tourism and exploration missions to other planets require significant amounts of energy. Even a 1% increase in energy efficiency can yield substantial benefits.

During the 1960s, while traditional rocket engines were advancing, research was also conducted on detonation engines. Detonation engines are a type of propulsion that utilizes a controlled shock wave to generate thrust. However, due to some engineering challenges such as the high temperature and heat flux of the shock wave and the limitations in material science, detonation engines have lagged behind traditional rocket engines. Although improvements have been made in traditional rocket engines to approach the efficiency provided by the cycle, and manufacturing methods have been enhanced, the increase in efficiency has been relatively small. In this context, it has been theoretically proven that

detonation engines are 1% to 20% more efficient compared to traditional rocket engines (Kumar,2019). This finding has led to a resurgence of research on detonation engines due to the advancements in technology, improved material properties, and developments in various CFD (Computational Fluid Dynamics) programs.

The ability of detonation engines to achieve hypersonic speeds has rapidly increased both experimental and theoretical research in this field. Many countries, including the USA, Russia, and Poland, are currently conducting military studies or research in university laboratories. Within the scope of this study, the aim is to design detonation engines with advanced thrust capabilities, which are essential for Turkey's needs in the aerospace and aviation fields.

The data obtained from this thesis aims to serve as a significant source of information in the literature and contribute to the space studies conducted in our country. The progress of Turkey in this field can enhance its independence and competitiveness in space technologies. Domestic designs related to detonation engines can contribute to the advancement of our country's space research and establish it as a key player in the field of space technology. These efforts can foster the development of local capabilities, advance scientific and technological knowledge, and strengthen national defence and space programs.

The content of the thesis includes four chapters of CFD (Computational Fluid Dynamics) studies. The first chapter covers the thesis's purpose, significance, and literature review. The second chapter provides information about the shock wave structure. In the third chapter, explanations are given about materials, methods, the fuels used within the scope of the thesis, and CFD analyses. The final chapter comprehensively evaluates the results obtained from the CFD studies.

CHAPTER 1

GENERAL INFORMATION

In this chapter, the thesis aims to provide information about its objectives, scope, the importance of detonation engines, and a literature review.

1.1. Purpose of the Thesis

Rocket motors are the most crucial propulsion systems of today, serving as a key element in various fields ranging from civil aviation to defence industry. The rising costs and excessive fuel consumption of rockets have led to an increasing focus on rocket motor technologies. Improving traditional rocket motors can be achieved through two approaches: cycle and production precision. Improving production methods without changing the cycle has shown limited improvements in rocket performance. Therefore, there is a need for a higher-performing cycle. Today's technological advancements have made it easier to address instability issues and have also led to significant progress in analysis programs. Observing Figure 1.1, it becomes apparent that the detonation cycle (Fickett-Jacobs) exhibits a higher compression ratio when compared to the Brayton-Joule and Humphrey cycles. In each case, the efficiency of the cycle is more than 20%, with an average increase of approximately 23%. One of the main motivations for the research on applying propulsion combustion to the propulsion system is the possibility of a significant increase in cycle efficiency (Kindracki,2008). Detonation engines are divided into Pulse Detonation Engines (PDE) and Rotating Detonation Engines (RDE), and they operate based on the concept of Deflagration to Detonation Transition (DDT), where the flame wave transforms into a detonation wave (Tsuboi et al.,2017). The position, number, blockage ratio, geometric dimensions, and fuel diversity of obstacles in the pre-detonator play a crucial role in generating an effective shock wave. In addition to creating the shock wave, high pressure and temperature must be achieved during the transition to the main detonator. Combustion based on detonation compresses the gas and ignites the mixture, resulting in both heat release and higher pressure. A high-temperature and high-pressure ignition system leads to improved performance. Explosion waves exert some compression effect on the gas mixture, which means that less turbo machinery will be required for the compression process before combustion. This leads to a generally lighter or smaller-sized engine design (Cao,2013). A pre-detonator consists of two different regions, which are the driver region and the driven region. They are separated by a diaphragm (Lee, 2008). The driver region contains a burnt fuel-air mixture, while the driven region contains an unburnt fuel-air mixture. By removing the diaphragm or igniting

with a spark plug, the high-temperature gas reacts with the unburnt fuel in the driven region to create a regular shock wave.

Using spark plugs, the formation time of the detonation can be quite stochastic; however, increasing the ignition energy can reduce the formation time of the explosion wave (Yang et al.,2016). This shock wave compresses and ignites the unburnt fuel ahead at high pressure and temperature. The high-temperature and high-pressure gas is then fed into a main detonator through injectors and expanded in the nozzle to obtain thrust force.

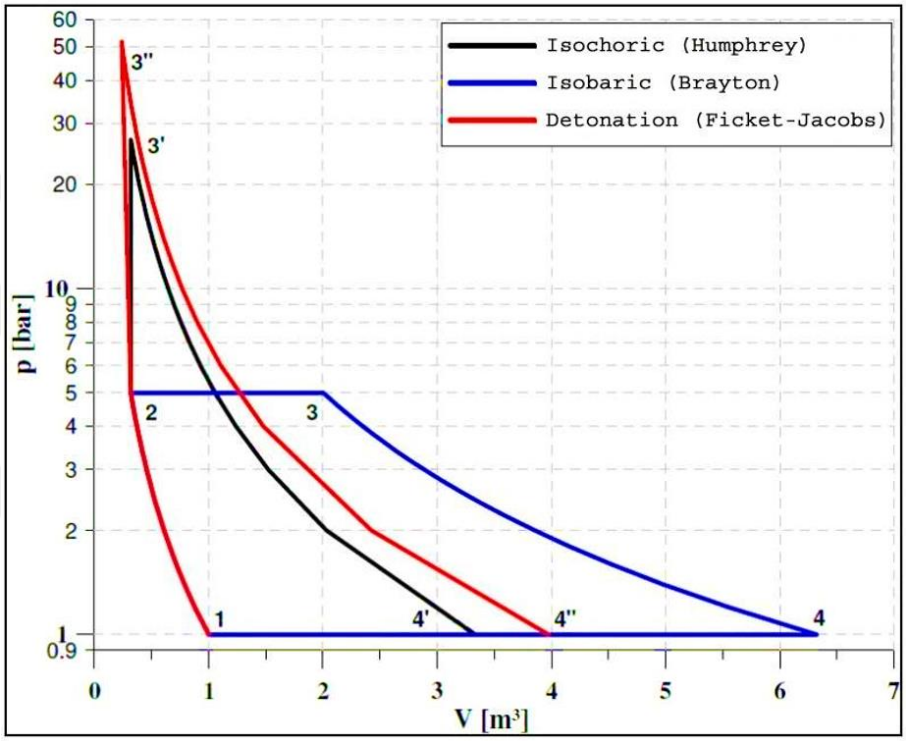

Figure 1.1. Thermodynamics Brayton-Joule, Humphrey, and Fickett-Jacobs cycles

Source: Wolański,2011:515-521.

In this thesis for optimal pre-detonator is to investigate the pressure, temperature, velocity, and shock formation times of fuels with different C/H ratios, as shown in Table 1.1, with three different equivalences and five different blockage ratios. The aim of this study is to design detonation engines with advanced thrust force, fulfilling the needs of our country in the field of aerospace and aviation. The results of this thesis are expected to make a significant contribution to the literature and serve as a valuable reference for the aerospace industry research in our country. Considering the advancements in detonation engines, it is evident that an increase in studies related to the design of detonation engines in our country will enable us to be part of the space technology race.

Table 1.1. Analysis Matrix

Fuels	Equivalence Ratios	Blockage Ratios
Acetylene	0.5 1 1.5	0.229 0.344 0.459 0.573 0.688
Kerosene		
Ethylene		
Ethane		
Methane		
Hydrogen		

1.2. Importance of Thesis

Considering the tons of fuel consumed for carrying massive payloads into orbit in the aerospace industry, even a 1% improvement in efficiency can lead to significant cost and emission reductions. Additionally, due to the higher efficiency of the detonation engine cycle compared to the Brayton rocket cycle, detonation engines have the potential to provide greater thrust than traditional rocket motors. Indeed, detonation engines have a simpler structure compared to other propulsion systems, as they do not require complex geometries or rotating shafts for power transmission. This simplicity makes their production easier. In this thesis, the impact of factors such as the location, number, blockage ratio, geometric dimensions, and fuel variety of obstacles will be investigated on the results of CFD analysis. The study will facilitate the design process through a parametric code developed in MATLAB 9.4 program, enabling easier and faster implementation of any design. By using this approach, the effects of different parameters on the design can be quickly evaluated. With the insights gained from this data, the developed detonation engines can be of critical importance to our country's defence industry.

1.3. Literature

Detonation engines have recently emerged as an intriguing propulsion technology of interest in the aerospace industry. These engines operate on the principle of supersonic combustion of fuel, generating thrust through the formation of a shock wave. Compared to traditional jet engines, these engines have the potential for higher efficiency and thrust. Below are some literature studies on the working principles, performance advantages, and industrial applications of detonation engines.

In this study, Lee et al. aimed to investigate the Deflagration to Detonation Transition (DDT) process of ethylene-air mixtures within a square tube and explore the impact of obstacles on the flame propagation rate. Various obstacle configurations, distances between

obstacles, and lengths of obstacle sections were examined to assess their influence on flame velocity. The results indicated that an obstacle should increase the flame velocity by approximately half of the Chapman-Jouguet (CJ) detonation speed to approach the minimum flame velocity. It was shown that creating both small and large-scale turbulence played a significant role in enhancing the flame acceleration caused by the obstacles.

The findings of this research emphasize the significance of obstacles in the Deflagration to Detonation Transition (DDT) process of pulse detonation engines, offering an alternative solution for such applications. The use of obstacles can enhance the shock wave formation process and lead to more efficient combustion (Lee et al.,2000).

In another study conducted by Liu et al., a 3-D numerical analysis of a premixed rotating detonation engine was carried out using a stoichiometric hydrogen-air mixture. They combined the single-step Arrhenius chemical model with the Euler equations in the computational study. It was observed that shock waves around the combustion chamber rotated counterclockwise. Furthermore, the reflected shock waves did not adversely affect the thrust performance of rotating detonation engines, unlike traditional engines (Liu et al.,2020).

In the literature studies on detonation engines, Liu and colleagues conducted an investigation on a two-dimensional rotating detonation engine, analyzing the flow field and pressure gain performance. They performed the analysis using the open-source software OpenFOAM. The results showed that when the inlet area ratio was less than 1, triangular-shaped gas layers exhibited different-sized striped distributions, which in turn reduced the pressure gain ratio in the combustion chamber (Liu et al.,2019).

Nikitin et al. conducted theoretical research on the fundamental operating cycle of pulse detonation engines (PDEs), investigating the transition from a propagating flame to detonation (DDT) process in combustible gas mixtures and the transmission of detonation into large chambers. The results of their studies suggest that for a successful initiation of detonation, a DDT should be initiated in a narrow gap and then transmitted into a larger chamber, which allows for a reduction in the length of the pre-detonation zone, thus shortening the required length of the engine (Nikitin et al.,2009).

The specific impulse measurements conducted for rotating detonation engines and pulse detonation engines, using hydrogen/air and ethylene/air mixtures, have shown quantitatively similar results. These findings indicate that rotating detonation engines, while

operating with gaseous hydrocarbon fuels, can achieve similar fuel efficiency and generate thrust power comparable to pulse detonation engines. Additionally, the combination of a rotating detonation engine with a turboshaft engine marks a promising development, offering new opportunities for more efficient and powerful utilization of rotating detonation engines. Rotating detonation engines can track the performance of gas turbine engines over a wide range of operating conditions and, at times, even outperform traditional gas turbine engines. The potential to leverage the advantages of pressure-gain combustion in these engines opens up opportunities for new combustion system designs. This situation supports the development of more efficient and sustainable power and propulsion technologies. Rotating detonation engines hold the potential to achieve higher efficiency and lower emissions in energy conversion, thereby promoting progress in the energy sector. The advancements in this field encourage the development of more efficient and sustainable power and propulsion technologies (Rankin et al.,2017).

The compressible Euler equations (D-scheme) are used to conduct a sensitivity analysis for a hydrogen/oxygen rotating detonation engine (RDE). These equations serve as a computational tool to evaluate the engine's performance. In this study, the program used was first compared to experimental data obtained by Kindracki and Wolanski. The calculated average pressure values were found to be close to the experimental values shortly after injection and generally ranged between 0.2 to 0.4 MPa. Sensitivity analyses indicate that the input pressure, Mach number, and temperature significantly affect the performance of the rotating detonation engine. Variations in these parameters have a pronounced impact on the engine's efficiency and power output. The results highlight the importance of having specific ranges of input conditions to achieve high performance with the rotating detonation engine. It demonstrates the need for certain input pressure, Mach number, and temperature ranges for the engine to operate stably. This analysis provides essential insights to comprehend and optimize the performance of rotating detonation engines. Such studies contribute to the development of approaches used to enhance the design and efficiency of rotating detonation engines (Hayashi et al., 2009).

In this study, Ge and colleagues experimentally investigated the influence of the blockage ratio on the formation of multiple detonation waves in a rotating detonation engine. Experimentally, under different blockage ratios and mass flow rates of air, four typical modes of detonation propagation were observed: single wave, hybrid mode with a combination of single and double waves, double waves, and longitudinally pulsating

detonation. The results indicate that as the blockage ratio increases, the critical mass flow rate for the formation of multiple waves decreases. An increased blockage ratio results in the formation of a hybrid mode, characterized by the coexistence of single and double waves, along with the stabilization of a bidirectional rotating detonation wave. The increased blockage ratio elevates the average pressure in the combustion chamber, intensifying the effect of reflected oblique shock waves on fresh reactants, which plays a significant role in the formation of multiple waves. Additionally, the increased blockage ratio raises the pre-combustion pressure. The high pre-combustion pressure leads to the presence of volumetric detonation immediately after ignition and consequently prolongs the formation time of the rotating detonation wave. These findings illustrate the impact of the blockage ratio on the formation of multiple waves in a rotating detonation engine, providing valuable insights for a better understanding of the engine's design and performance. Moreover, it contributes to the development of design approaches to enhance the efficiency and reliability of rotating detonation engines (Ge et al.,2019).

Korytchenko and colleagues conducted a study on shock wave initiation in pulse detonation engines. In this study, two spark discharges were used as a simultaneous igniter that can ignite concurrently. The spark discharges were fired at a distance that provided intense gas-dynamic interactions between the discharges. In the regions between the spark gaps, an increase in gas temperature occurred due to the collision of incoming shock waves. The impact of dual spark ignition on the ignition duration and length of flame propagation along the combustion tube was investigated by comparing transition parameters for both single-spark and dual-spark ignition cases, with all other conditions being kept equal. The study utilized a combustion tube with a length of 2.3 m and an internal diameter of 22 mm. The spark plugs were located at the closed end of the tube. A stoichiometric mixture of propane and oxygen diluted with 50% nitrogen at an initial pressure of 50 kPa was used. The tube was equipped with 22 ionization sensors to record the flame front propagation time and measure the flame speed. The distance between the ignition sources was 6 mm, and the discharge gap length for each ignition source was 2.5 mm. The spark plug-shaped ignition sources were connected to high-voltage units with a total discharge energy of 3.3 J. The results of the study showed that the transition distance from the flame front to detonation decreased by 1.6 to 2 times, and the transition time reduced from 3.9 ms for single-spark ignition to 1.2 ms for dual-spark ignition. The findings of this study provide valuable insights that can be used in the design of ignition systems for pulse detonation engines (Korytchenko et al.,2019).

Peng and other researchers conducted experiments using ethylene-air and hydrogen-air mixtures to examine the effect of the relationship between deflagration and detonation on continuous rotating detonations. In the experiments, different tests were conducted by varying the length of the inner cylinder. In the ethylene-air mixture, the continuous rotating detonation wave was sustained in a hollow cavity region near the terminal of the inner cylinder. Prior to this continuous rotating detonation wave, a deflagration occurred, which eliminated the accumulation of the combustible mixture, and this deflagration is referred to as "parasitic combustion." As the intensity and longitudinal range of the parasitic combustion increased, the frequency and stability of the detonation wave propagation decreased. In the case of the hydrogen-air mixture, the detonation wave could sustain itself, but it failed to hold a five mm-wide annulus, resulting in discrete structures of the detonation wave that increased the overall combustion rate. It was suggested to rapidly initiate the continuous rotating detonation within a short distance and maintain the structural integrity of the detonation wave to reduce the impact of parasitic combustion. Additionally, a longitudinally pulsed combustion mode was discovered and analyzed. As a result, this study has helped us understand the characteristics of continuous rotating detonations and provided design recommendations to mitigate the effects of parasitic combustion (Peng et al.,2020).

Ahumada and colleagues conducted experiments on the flame propagation and DDT (Deflagration to Detonation Transition) of stoichiometric premixed hydrogen-oxygen mixtures in a closed tube. They used circular obstacles with increasing, decreasing, and equivalent blockages, at obstacle distances of 1D, 2D, and 3D, and with three different blockage ratios (%25, %40, and %80). Based on the tested conditions, obstacles with higher blockage ratios at the second obstacle resulted in stronger combustion. Different spreading characteristics and explosion strengths were observed for obstacles with equivalent blockages (Ahumada et al.,2020).

In this study, Cheng and colleagues explored a new method using a non-reactive gas jet (CO_2) to facilitate the formation of shock waves and flame propagation speed in a stoichiometric methane-oxygen mixture. They found that high jet pressure and prolonged jet duration increased the local CO_2 concentration, negatively affecting the occurrence of the explosion. Consequently, they determined the most suitable injection conditions with an injection pressure ratio of 15, a jet delay time of 20 milliseconds, and a jet location of 0.6m. These parameters were confirmed to have significant effects on DDT (Deflagration to Detonation Transition), and the underlying mechanisms were investigated and explained in

this study. The research provided new experimental evidence supporting the theory that increasing turbulence enhances the initiation of an explosion (Cheng et al.,2021).

In this study conducted by Zheng and their team, the effects on the formation and propagation of shock waves were investigated. Experiments were performed using three-dimensional numerical simulations, where the mass flow rate of hydrogen was varied to achieve lean and rich mixture ratios while keeping the air mass flow rate constant. The research identified that the equivalence ratio played a critical role in the formation and propagation of shock waves and had a significant impact on the thrust of the rotating detonation engine. The experiments were conducted at different equivalence ratios (0.6, 0.8, 1.0, and 1.4) and in the single wave mode (equivalence ratio: 1.2). The study found that when the equivalence ratio was 1.0, the rotating detonation engine exhibited the shortest formation time, best propagation stability, moderate thrust, and specific impulse, indicating excellent operational performance. Furthermore, the equivalence ratio and mass flow rate of hydrogen were identified as key mechanisms in determining the probability and propagation of shock formation during the re-initiation process (Zheng et al.,2020).

In this study, Alam and their colleagues conducted an analysis of a Pulsed Detonation Engine (PDE) tube with variable spaced obstacles and a fixed blockage ratio. Three-dimensional reactive Navier-Stokes equations and the realizable k-ε turbulence model were used to simulate the combustion process of a hydrogen-air mixture. The research focused on the flame propagation and Deflagration-to-Detonation Transition (DDT) process. Based on the normal propagation regime, the working length was determined. As the gap between the inner surface of the obstacle and the outer diameter increased, the flame spreading area decreased near the combustor axis. This led to an increase in the momentum loss of turbulent combustion particles and unburned fuel particles (gaps) behind the obstacle, resulting in a decrease in the shock wave velocity and total blast pressure. Similarly, the thrust generated by the PDE also decreased as the obstacle diameter decreased. Moreover, the study found that the DDT flame formation time was extended along the combustor axis at lower temperatures produced by the PDE (Alam et al.,2020).

This thesis aims to contribute to the literature by examining the effects of different equivalence ratios and blockage ratios on the pressure, temperature, and velocity values generated by fuels with different C/H ratios in detonation engines.

CHAPTER 2

DETONATION ENGINES AND FUNDAMENTALS

Combustion can be explained as the emission of heat and light energy resulting from the fuel's oxidation reaction with oxygen. Flame can be divided into two forms: Deflagration and Detonation. Deflagration is commonly seen in daily life, such as in internal and external combustion engines. Deflagration occurs at subsonic speeds and under constant pressure conditions. Compared to detonation, deflagration produces energy at a lower rate. Detonation, on the other hand, rapidly generates a large amount of energy, which can lead to significant damage, like knocking, in internal combustion engines. Long-distance pipelines between cities are also at risk of experiencing these detonations. However, when harnessed effectively, the high-speed energy from controlled detonation can lead to significant advancements, especially in aviation, by creating thrust or shaft power. The controlled and efficient utilization of combustion processes is essential for various applications. In everyday life, deflagration is commonly used for its practical applications in engines. Meanwhile, detonation needs to be handled with great care due to its potential risks. Proper engineering and safety measures are critical to ensuring the safe and efficient use of detonation, particularly in the context of internal combustion engines and long-distance pipelines. Effectively harnessed, the high-speed energy generated by detonation has the potential to propel advancements across various fields. Aviation, in particular, can benefit from this energy, using it to generate thrust or shaft power, thus paving the way for innovative technological and industrial breakthroughs. In this chapter, general information about detonation engines, detonation models, thermodynamic cycles, and the structure of shock waves are given.

2.1. Pulsed Detonation Engine

Pulsed Detonation Engine (PDE) is a type of motor system where fuel injection is performed in pulses. In these engines, fuel is sprayed into the combustion chamber at regular intervals by fuel injectors. After each injection pulse, the fuel-air mixture rapidly ignites, resulting in the formation of a detonation wave. These waves spread rapidly, allowing the engine to continuously produce thrust. One of the primary advantages of pulsed detonation engines is that they offer a more efficient combustion process. Injecting fuel in pulses enables precise control and optimization of the combustion process, resulting in higher thrust intensity and lower fuel consumption. ADMs also have the potential to achieve higher power

and performance levels. The rapid spread of detonation waves leads to a more intense energy release, resulting in a more powerful thrust production.

The pulsed detonation engines consist of two sections: the driver and the driven sections, separated by a region known as the diaphragm. The driver section contains high-pressure and high-temperature gases, while the driven section contains a mixture of unburned fuel and air. In the driven section, turbulence-enhancing obstacles are used to accelerate the formation of shock waves. Upon removal of the diaphragm, an ignition flame propagates between these two sections, undergoing transformation into a shock wave as it traverses the turbulence-enhancing obstacles. Instantaneous pressure and temperature values are measured using sensors installed on the PDE.

Figure 2.1 shows a representative illustration of this engine. This motor has potential applications in various fields, such as space exploration, rocket technology, and air and sea vehicles. The development and optimization of PDEs are continuously pursued to achieve more efficient and powerful propulsion. These engines hold significant potential for future advancements in technology and performance.

Figure 2.1. PDE Engine

Source: Tate,2015:33.

2.2. Rotating Detonation Engine

Rotating Detonation Engines (RDE) are motors that operate with a circular combustion chamber and rotating combustion rings. These engines have a combustion process where the gas mixture continuously rotates, forming combustion rings. The

combustion rings are arranged in a rotating manner within the combustion chamber and undergo sequential combustion.

The rotating detonation engines (RDE) have a different operating principle compared to traditional linear detonation engines. The rotation of the combustion rings enables a more efficient combustion process and allows for higher thrust generation. Additionally, the rotation of the combustion rings ensures a more stable combustion process and reduces vibrations. There are some challenges to consider in the design of these engines. Firstly, the regular rotation and timing of the combustion rings are crucial. Accurate timing and speed are required to control the combustion process effectively. Furthermore, achieving a homogenous distribution of fuel and air mixture in the circular chamber and increasing combustion efficiency are important design objectives.

The detonation engines maintain the continuity of the shock wave created in the pre-detonator through the fuel injected from the injectors. The sustenance of the shock wave is the most critical parameter for the continuity of thrust force. High-pressure and high-temperature gas is expanded through a nozzle to obtain thrust force. Figure 2.1 shows a visual representation of a rotating detonation engine.

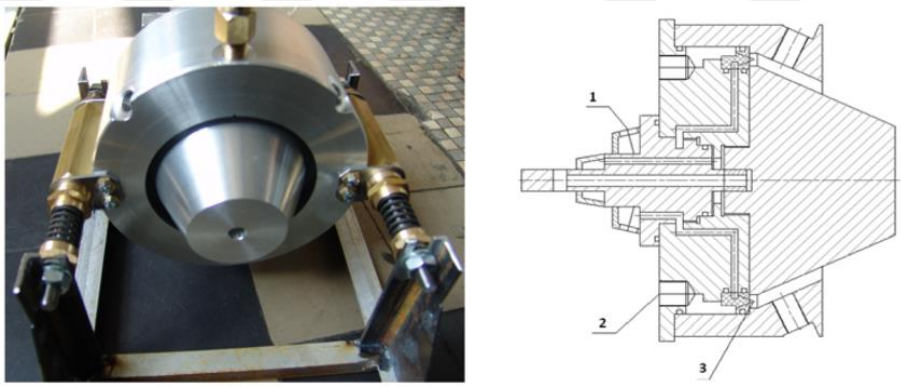

Figure 2.2. Rotating Detonation Engine 1- Fuel, 2- Oxygen and 3- Injection Point of Both Components

Source: Wolański,2021:623-636.

The rotating detonation engines are considered the next-generation engines expected to play a significant role in the aviation and aerospace industries in the future. These engines have the potential to offer higher performance, improved fuel efficiency, and more reliable operation. However, further research and development are required in this field, as rotating detonation engines are not yet fully ready for commercial applications.

2.3. Deflagration

Reactants ignite in subsonic combustion circumstances and go via a process known as "flame propagation" or "flame ignition." In open volumes, there is a negligible pressure drop during combustion, allowing the combustion process to be modelled as isobaric. However, a significant increase in temperature occurs during this process, particularly at the moments when fuel and oxidizer are ignited. The thermodynamic cycles of internal combustion engines, such as the Brayton cycle for Diesel and Otto engines, can exemplify this process. In a structure with both ends open, for most hydrocarbon-air mixtures, the flame propagation velocity typically ranges from 0.2 to 2 m/s (Glassman & Yetter,2008). Depending on the length of the tube where combustion initiates, a shock wave can occur, indicating the transition from the flame wave inside the tube to a detonation.

2.4. Detonation

The detonation wave is an exothermic reaction that forms and sustains a shock wave in the region where the fuel and oxidizer mixture are present. Flame waves typically exhibit speeds ranging from 0.2 to 2 m/s, whereas detonation waves can attain velocities as high as 2000 m/s. Unlike the flame wave, the speed, heat conduction, and radical diffusion do not control the detonation; instead, the supersonic shock wave structure raises the temperature and pressure to a level that leads to energy release in explosive reactions, sustaining the wave propagation (Glassman & Yetter,2008). The formation and propagation of the detonation wave compress the gas upwards along with combustion, causing extreme pressure and temperature. This process is explained through the one-dimensional Chapman-Jouguet theory and the Zel'dovich-von Neumann-Döring model. Combustion is modelled in one-dimensional constant-volume cycles such as Fickett-Jacobs, Humphrey, and Brayton Rocket cycles. The efficiency and combustion method in these cycles produces 1.3-1.5 times the efficiency of the isobaric combustion cycle at an equivalent pressure ratio. If mechanical efficiencies are maintained, it can lead to an increase in fuel efficiency as well (Bussing & Pappas,1994).

2.4.1. CJ Model

The earliest and fundamental theory of detonation waves was developed by Chapman (1899) and Jouguet (1905). This theory assumes that the detonation wave is steady, planar, and one-dimensional. The detonation wave is analyzed using a control volume that surrounds the shock wave and the reaction zone, as shown in Figure 2.3.

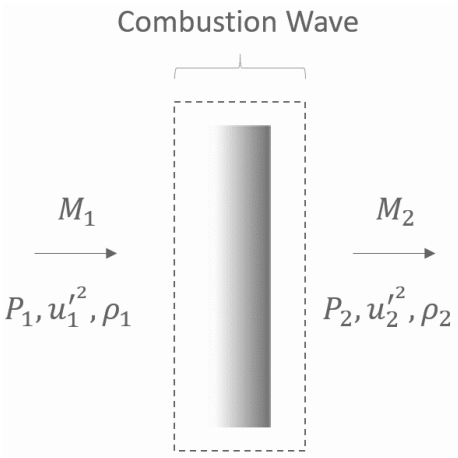

Figure 2.3. Control Volume Used in Chapman-Jouguet Theory

Source: Wintenberger,2004:2.

The equations of mass, momentum and energy conservation are applied to this control volüme, respectively.

$$\rho_1 u_1' = \rho_2 u_2' \tag{2.1}$$

$$P_1 + \rho_1 u_1'^2 = P_2 + \rho_2 u_2'^2 \tag{2.2}$$

$$h_1 + u_1'^2/2 = h_2 + u_2'^2/2 \tag{2.3}$$

Case 1 corresponds to reactants upstream of the wave, and case 2 corresponds to products downstream of the wave. From these equations, the Hugoniot relation can be obtained. Hugoniot finds possible outcomes for state 2 with a given release of energy from a given state 1. If Hugoniot is plotted on a pressure and specific volume diagram. Figure 2.4 shows the Hugoniot curve with energy oscillation and the shock Hugoniot scheme (no energy oscillation). The Rayleigh line for case 1 and case 2 is given as follows:

$$h_2 - h_1 = \tfrac{1}{2}(P_2 - P_1)\left({}^{1}/_{\rho_1} + {}^{1}/_{\rho_2}\right) \tag{2.4}$$

$$P_2 - P_1 = -(\rho_1 u_1')^2\left({}^{1}/_{\rho_2} - {}^{1}/_{\rho_1}\right) \tag{2.5}$$

Region III in Figure 2.4 is out of the solution range as it does not represent real solutions. It is obvious that the solutions in regions I and II are supersonic (explosions), and the solutions in regions IV and V are subsonic waves (deflagrations).

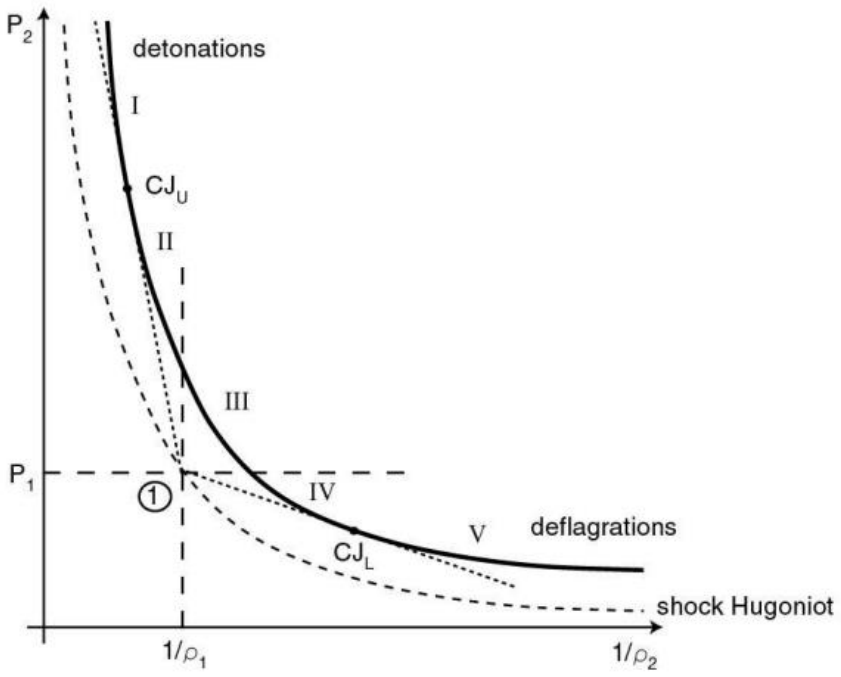

Figure 2.4. Energy Release, Shock Hugoniot and Hugoniot Curve

Source: Wintenberger,2004:3.

These evaluations were independently made by Jouguet (1905) and Chapman (1899). As a result of their work, they proposed that detonation waves and shock waves in the detonation wave all travel at a certain minimum speed. Chapman (1899) assumed that the Hugoniot and Rayleigh lines are tangent at the solution point. From these evaluations, it can be shown that the flow behind the wave is sonic relative to the wave, meaning $M_2 = 1$. The point where the Hugoniot, Rayleigh line, and isentrope are tangent to each other is called the Chapman-Jouguet (CJ) point. There are two CJ points on the Hugoniot curve. The upper CJ point (CJ_U) is located in the detonation zone, while the lower CJ point (CJ_L) is in the deflagration zone. These points divide the Hugoniot into four regions (Region III is eliminated as it is outside the realm of real solutions). The fourth region, Region IV, corresponds to weak deflagration waves (subsonic flow to supersonic flow) and includes laminar flame solutions. The fifth region, Region V, corresponds to strong deflagration waves (subsonic flow to supersonic flow), and it is not physically possible to go beyond the sonic condition with a constant addition of heat in a fixed area (Anderson,1990). Therefore, Region V is disregarded as it does not provide a physically plausible steady solution. Strong detonation waves (supersonic flow to subsonic flow) correspond to Region I. These waves are unstable. They become unstable due to rarefaction waves that move behind the detonation wave. These rarefaction waves result from factors like friction, heat loss, turbulence, and other similar phenomena. These rarefaction waves effectively catch up with

the detonation front, causing a shift in the solution point. This shift occurs towards the CJU (Chapman-Jouguet Upstream) point. Finally, Region II corresponds to weak detonations (supersonic flow to supersonic flow) and, except for exceptional cases with very specific constraints on the reaction mechanism, speeds, and thermodynamics, it can be disregarded considering the structure of the reaction zone. Region III (Rayleigh lines intersecting with imaginary intersections in Region III) is impossible due to conservation laws. Regions II and V seem to be exotic possibilities that appear only in exceptional cases where there are very specific constraints on the reaction mechanism, velocities, and thermodynamics ("eigenvalue" solutions). There is no gas dynamic solution for subsonic waves (Region IV). Here, other processes, such as turbulence and molecular diffusion, need to be considered. For supersonic waves (Region I), there is a single special thermodynamic solution, CJ_U. If there is a kind of piston following the wave, it is possible to remove the detonation waves to higher speeds than U_{CJ} (Upstream of CJ_U).

2.4.1.1. Characteristics of the CJ Top Point

NASA Glenn Research Center has developed the Chemical Equilibrium with Applications (CEA) program, which has an explosion function, to easily calculate the parameters at the CJ point. Common hydrocarbons containing both air and oxygen have been analyzed using CEA, and the results are shown in Table 2.1. Upon reviewing Table 2.1, one can notice that oxygen results in elevated values of pressure, temperature, velocity, and Mach number in comparison to air.

Table 2.1. Chapman-Jouguet Parameters of Some Hydrocarbons (100kPa, 298K)

Mixture	P/P_1	T/T_1	ρ/ρ_1	M_{CJ}	U_{CJ} (m/s)
Methane-Air (CH_4)	17.4	9.4	1.8	5.1	1800
Propane-Air (C_3H_8)	18.4	9.6	1.8	5.3	1796
Ethylene-Air (C_2H_4)	18.5	9.6	1.8	5.3	1821
Acetylene-Air (C_2H_2)	19.3	10.6	1.8	5.4	1864
Methane-O_2(CH_4)	29.6	12.6	1.9	6.8	2390
Ethylene-O_2(C_2H_4)	33.8	13.3	1.9	7.3	2374
Acetylene -O_2(C_2H_2)	34.2	14.3	1.8	7.4	2426
Propane-O_2(C_3H_8)	36.6	13	1.9	7.7	2357

Source: Tate,2015:20.

The rate of change of entropy along the Hugoniot is given by

$$T_2\left[\frac{ds_2}{d\left(1/\rho_2\right)}\right]_H = \frac{1}{2}\left(1/\rho_1 - 1/\rho_2\right)\left(-\frac{P_1 - P_2}{1/\rho_1 - 1/\rho_2} + \left[\frac{dP_2}{d\left(1/\rho_2\right)}\right]_H\right) \tag{2.6}$$

In this context, H is used to emphasize the differentiation along the Hugoniot curve (Courant and Friedrichs, 1967). At the CJ point, the Hugoniot, Rayleigh line, and isentrope are all tangent, and thus $\frac{ds_2}{d\left(\frac{1}{\rho_2}\right)} = 0$. Therefore, CJ points correspond to the extrema of entropy along the Hugoniot. When the previous equation is differentiated at CJ points, the following result is obtained.

$$\left[\frac{d^2 s_2}{d(1/\rho_2)^2}\right]_H = \frac{\frac{1}{\rho_1} - \frac{1}{\rho_2}}{2T_2}\left[\frac{d^2 P_2}{d(1/\rho_2)^2}\right]_H \tag{2.7}$$

Since the Hugoniot is convex everywhere, i.e., $[d^2P_2/d(1/\rho_2)^2]_H > 0$, at the upper CJ point, $[d^2s_2/d(1/\rho_2)^2]_H > 0$, and entropy reaches a minimum (Courant and Friedrichs,1967). Similarly, the lower CJ point represents the highest level of entropy. Therefore, the upper CJ point denotes the lowest entropy point for the combustion product along the Hugoniot curve.

2.4.2. Ideal Gas Model

In CJ detonation, analytical solutions for the upper CJ point (CJ_U) can be obtained by making assumptions about the specific heat ratios and the perfect gas constant for the reactants and products at different values.

The heat of combustion q_c can be calculated using the equations $h_1 = h_1^0 + C_p T_1$ ve $h_2 = h_2^0 + C_p T_2$, where $q_c = h_1^0 - h_2^0$. By utilizing the conservation equations (Equations 2.1-2.3) and the CJ condition (M2 = 1), two γ models (Thompson,1988) can be derived.

$$M_{CJ} = \sqrt{H + \frac{(\gamma_1 + \gamma_2)(\gamma_2 - 1)}{2\gamma_1(\gamma_1 - 1)}} + \sqrt{H + \frac{(\gamma_2 - \gamma_1)(\gamma_2 + 1)}{2\gamma_1(\gamma_1 - 1)}} \tag{2.8}$$

Here, the non-dimensional heat of combustion H is given as follows;

$$'\mathrm{H} = \frac{(\gamma_2-1)(\gamma_2+1)q_c}{2\gamma_1 R_1 T_1} \tag{2.9}$$

Other CJ properties can be found by substituting them into the conservation equations.

$$U_{CJ} = M_{CJC_1} \tag{2.10}$$

$$\frac{P_2}{P_1} = \frac{\gamma_1 M_{CJ}^2 + 1}{\gamma_2 + 1} \tag{2.11}$$

$$\frac{\rho_2}{\rho_1} = \frac{\gamma_1(\gamma_2+1)M_{CJ}^2}{\gamma_2\left(\gamma_1 M_{CJ}^2 + 1\right)} \tag{2.12}$$

$$\frac{T_2}{T_1} = \frac{R_1}{R_2}\frac{P_2}{P_1}\frac{\rho_1}{\rho_2} \tag{2.13}$$

$$u_2 = U_{CJ}\left(1 - \frac{\rho_1}{\rho_2}\right) \tag{2.14}$$

To further simplify the model, if we assume a common specific heat ratio and perfect gas constant for both reactants and products, we can derive the equations for the single-γ model (Fickett and Davis,2001).

$$\mathrm{M_{CJ}} = \sqrt{'\mathrm{H}+1} + \sqrt{'\mathrm{H}} \tag{2.15}$$

$$'\mathrm{H} = \frac{(\gamma^2-1)q_c}{2\gamma R T_1} \tag{2.16}$$

CJ relations are given below,

$$\frac{P_2}{P_1} = \frac{\gamma M_{CJ}^2 + 1}{\gamma + 1} \tag{2.17}$$

$$\frac{\rho_2}{\rho_1} = \frac{(\gamma+1)M_{CJ}^2}{1+\gamma M_{CJ}^2} \tag{2.18}$$

$$\frac{T_2}{T_1} = \frac{\left(1+\gamma M_{CJ}^2\right)^2}{(\gamma+1)^2 M_{CJ}^2} \tag{2.19}$$

$$M_{CJ} = \left[\frac{2(\gamma+1)}{C_p T_1}\left(\frac{q}{\dot{m}}\right)\right]^{\frac{1}{2}} \tag{2.20}$$

Another approach is to assume that the Mach number during the detonation is much larger, and this assumption is closely related to the "strong detonation" solution (Fickett and Davis,2001). In this approach, it has been found that the detonation propagation speed is proportional to the square root of energy release, the CJ pressure varies with the product of initial mixture density and energy release, and the CJ temperature is directly proportional to the energy release.

$$U_{CJ} \approx \sqrt{2(\gamma_2^2 - 1)q_c} \tag{2.21}$$

$$\rho_2 \approx \frac{\gamma_2 + 1}{\gamma_2} \rho_1 \tag{2.22}$$

$$P_2 \approx \frac{1}{\gamma_2 + 1} \rho_1 U_{CJ}{}^2 \approx 2(\gamma_2 - 1)\rho_1 q_c \tag{2.23}$$

$$T_2 \approx \frac{2\gamma_2(\gamma_2 - 1)}{\gamma_2 + 1} \frac{q_c}{R} \tag{2.24}$$

$$u_2 \approx \frac{U_{CJ}}{\gamma_2 + 1} \tag{2.25}$$

2.4.3. ZND Model

Zel'dovich (1940), von Neumann (1942), and Döring (1943) independently worked on the structure of detonation waves and developed a theory known as the ZND theory. This theory combines the detonation wave with a reaction zone to model a strong shock wave.

Chemical reactions are initiated in the Von Neumann condition, causing the planar shock wave to transform the gas into the post-shock or Von Neumann state. Immediately after the shock, there is an induction zone characterized by the formation of radicals in chain-branching reactions. This region is generally thermally neutral. Following the induction zone, the temperature rises due to the energy release from the reaction, while the pressure and density decrease due to the expansion of hot products. This expansion sustains the strength of the precursor shock front. The induction and energy release zones together form the reaction zone. The reaction zone ends at the Chapman-Jouguet plane, where the flow velocity becomes sonic with respect to the shock wave, and chemical equilibrium is achieved. The ZND model considers the flow's one-dimensional shock wave with discontinuities and neglects transport effects. The model includes chemical kinetics with a finite reaction rate. The reaction zone, including thermodynamic properties and

concentrations of chemical species, is solved using reactive Euler equations within the framework of the shock wave.

$$\frac{D_\rho}{D_t} = -\rho \frac{du}{dx} \tag{2.26}$$

$$\frac{D_u}{D_t} = -\frac{1}{\rho}\frac{dP}{dx} \tag{2.27}$$

$$\frac{D\left(h + \frac{u^2}{2}\right)}{D_t} = \frac{1}{\rho}\frac{\partial P}{\partial x} \tag{2.28}$$

We can rewrite the Euler equations in the wave reference frame as follows.

$$u' = \frac{d\rho}{dx} = -\frac{\rho\dot{\sigma}}{1 - M^2} \tag{2.29}$$

$$u' = \frac{dw}{dx} = \frac{u'\dot{\sigma}}{1 - M^2} \tag{2.30}$$

$$u' = \frac{dP}{dx} = -\frac{\rho u'^2\dot{\sigma}}{1 - M^2} \tag{2.31}$$

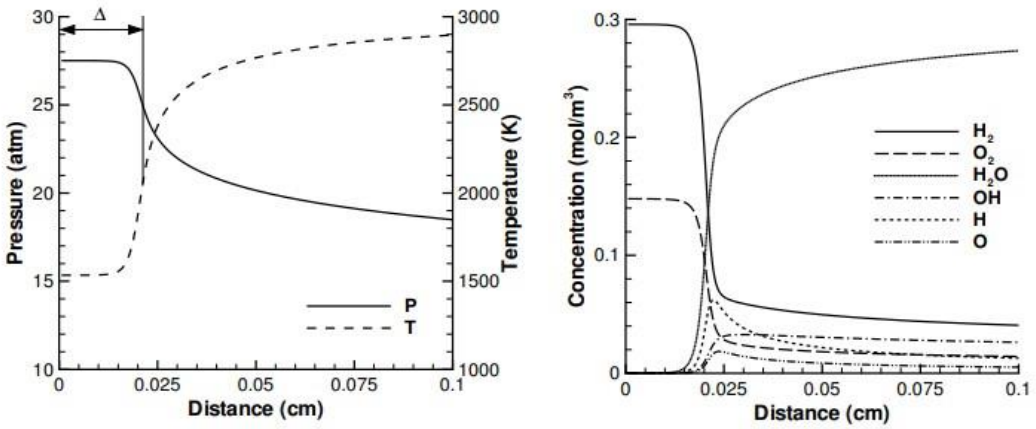

Figure 2.5. Konnov's ZND Profile, Left: Pressure and Temperature Profiles. Right: Species Concentration Profiles.

Source: Konnov,1998:122.

Thermodynamic properties and species concentrations behind the shock front can be calculated using a numerical solution of the ZND model. The induction zone starts after the shock front and ends with a sharp increase in radical concentration and temperature

corresponding to the beginning of the energy release zone. As the main products form, the energy release zone is characterized by a substantial decrease in radical concentration. These regions can be analyzed using numerical solutions of the ZND model to determine the structural characteristics of the detonation wave.

Pressure, temperature, and species concentrations approach equilibrium values at the end of the energy release zone. The length of the induction zone, denoted as Δis typically defined as the distance from the leading shock front to the point of maximum heat release. It depends on the mixture composition, initial conditions, and chemical kinetic rate and is a vital function of post-shock temperature. The length of the induction zone serves as a length scale that can be used to characterize the thickness of the detonation front.

2.5. Thermodynamic Cycles

Pulse detonating engines and detonation are categorized as either constant volume combustion or pressure-gain combustion mechanisms. These can be closely modeled by the Humphrey and Fickett-Jacobs cycles, still, even though they can be modeled closely, they exhibit differences in terms of overall efficiency and theoretical work.

2.5.1. Brayton Rocket Cycle

The Brayton cycle is a simple gas turbine (GT) cycle and consists of four fundamental stages:

a) Compression: It takes in outside air and compresses it using a high-pressure compressor. In this stage, the air's entropy decreases, and its temperature increases.

b) Heating: The compressed air is sent to a combustion chamber and burns with fuel. This combustion process increases the air's temperature and expands its volume.

c) Expansion: The gases exiting the combustion chamber are directed toward a high-speed turbine rotor. The gases rotate the turbine rotor, providing power output on a shaft at the turbine's exit.

d) Cooling: This stage is used to lower the exit temperature of the gases and extend the turbine's lifespan. Typically, air or water is used for this cooling process.

The Brayton cycle is utilized in various applications. For instance, jet engines used in aeroplanes and gas turbine generators used to produce electricity employ this cycle.

2.5.2. Humphrey Cycle

The Humphrey cycle, also known as the Atkinson cycle, is commonly used to assess the efficiency of explosions. Figures 2.6 and 2.7 show the P-v diagram and T-s diagram, respectively, comparing the Humphrey cycle to the Brayton cycle. The Humphrey cycle consists of four stages: isentropic compression (1-2), constant volume heat addition (2-3), isentropic expansion (3-4), and constant pressure heat rejection (4-1) to complete the cycle.

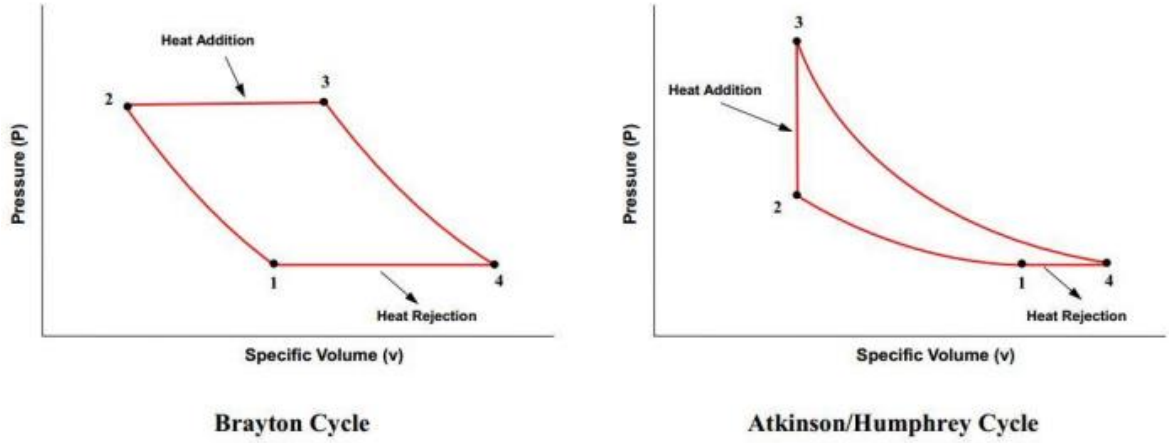

Figure 2.6. P-v Diagrams of Brayton and Humphrey Cycles

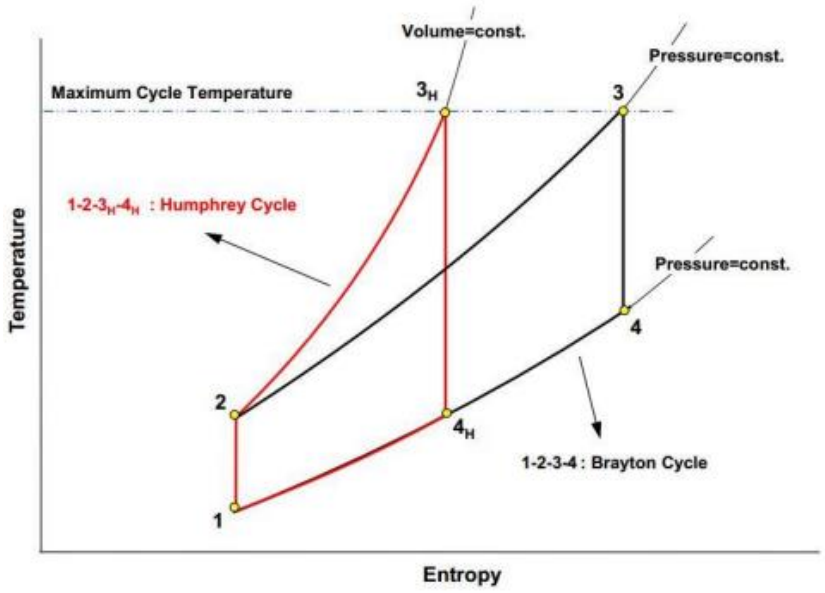

Figure 2.7. T-s diagrams of Brayton and Humphrey Cycles

Source: Bussing & Pappas,1994:263.

The Humphrey cycle is very similar to the Brayton cycle and is often compared in terms of efficiency. The constant volume heat addition in the Humphrey cycle increase

pressure, which is the main advantage over the Brayton cycle. This advantage leads to a much larger expansion ratio in the Humphrey cycle compared to the compression ratio. As a result, engines using the Humphrey cycle at the same inlet conditions can produce more power than those using the Brayton cycle. Additionally, the constant volume heat addition generates less entropy than in the Brayton cycle, providing an efficiency advantage to the Humphrey cycle.

According to the reference to the study by Bussing & Pappas in 1994, it is explained that the Humphrey cycle has an additional term that is always smaller than one when compared to the Brayton cycle. Therefore, considering the same temperature ratios and specific heat values, the Humphrey cycle will have a higher efficiency compared to the Brayton cycle. This suggests that the Humphrey cycle can potentially offer improved performance and higher efficiency in certain applications.

Humphrey Thermal Cycle Efficiency

$$\eta_{th,\text{Humphrey}} = 1 - \left(\frac{T_0}{T_1}\right)\gamma \left[\frac{\left(\frac{T_2}{T_1}\right)^{\frac{1}{\gamma}} - 1}{\left(\frac{T_2}{T_1}\right) - 1}\right] \tag{2.32}$$

Brayton Thermal Cycle Efficiency

$$\eta_{th,\text{Brayton}} = 1 - \frac{T_0}{T_1} \tag{2.33}$$

2.5.3. Fickett-Jacobs Cycle

The Fickett-Jacobs (FJ) cycle is a conceptual thermodynamic cycle used to calculate the maximum amount of work that can be obtained from detonating a mass (Wintenberger & Shepherd,2005). The FJ cycle is based on the piston-cylinder arrangement shown in Figure 2.8.

The physical steps of this conceptual cycle are as follows:

1) Reactants are in the initial state.

2) The reactants are compressed isentropically.

3) An external force is applied to the left piston, initiating the detonation.

4) As the detonation wave propagates inside the cylinder, the resulting products move with the piston at velocity U_p.

5) The products resulting from the detonation move with adiabatic and reversible expansion, converting the piston's mechanical energy into work.

6) The products are expanded isentropically back to the initial pressure.

7) Heat is removed reversibly at constant pressure to cool the products until they reach the initial temperature.

8) After completing the cycle, the same steps are repeated for the next one.

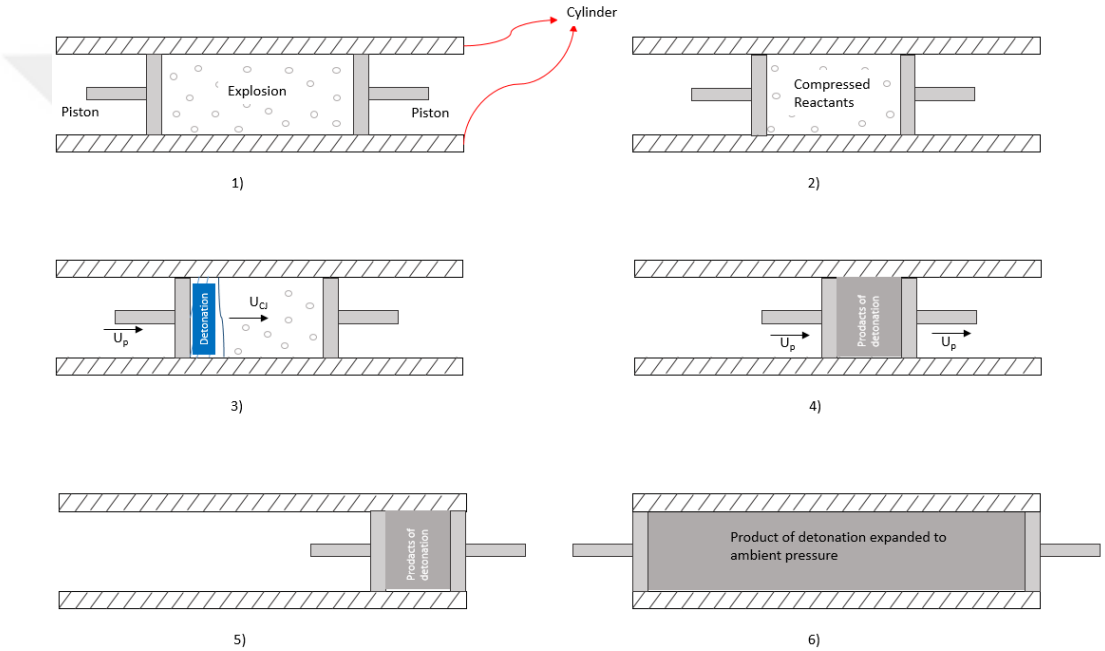

Figure 2.8. Steps that Make Up the Fickett-Jacobs Cycles

Source: Wintenberger & Shepherd,2006:694-698.

Figure 2.7 compares this cycle with the Brayton and Humphrey cycles. Thermal efficiency values are calculated using a one-dimensional γ detonation model, considering a perfect gas model, and related to the CJ Mach number associated with the specific heat of combustion (Wintenberger & Shepherd,2006). The thermal efficiency of the Fickett-Jacobs cycle is defined as a function of the expansion ratio of the products, which increases proportionally with the CJ Mach number and is cooled at a constant pressure.

$$\eta_{th,\mathrm{FJ}} = 1 - \frac{C_p T_1}{q_c}\left[\frac{1}{M_{cj}^2}\left(\frac{1+\gamma M_{cj}^2}{1+\gamma}\right)\right. \tag{2.34}$$

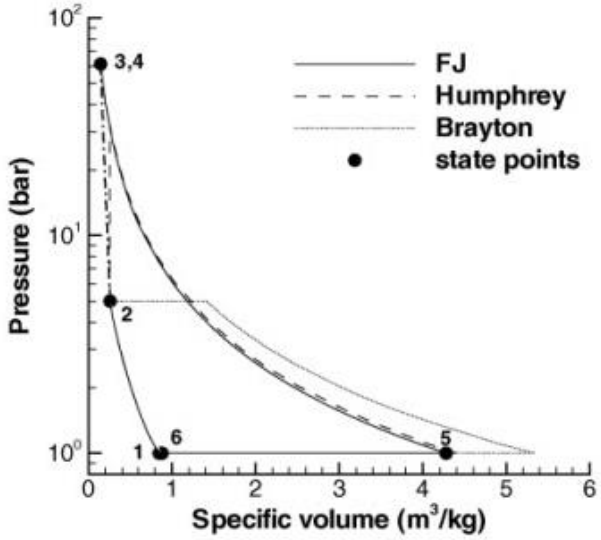

Figure 2.9. P-v Diagram of Fickett-Jacobs Cycle with Humphrey and Brayton

Source: Wintenberger & Shepherd,2006:694-698.

2.6. Detonation Wave Cell Structure

The one-dimensional CJ and ZND detonation theories, which we assume, provide values close to experimental results. Albeit, the real detonation is far from being one-dimensional. Immediately behind the precursor shock, there are transverse shocks, and these shocks create triple points when they intersect with the precursor shock. These triple points are localized regions of high pressure and temperature, and they contribute to the stabilization of the detonation wave. Additionally, these triple points accelerate local reaction rates. The detonations that occur are far from being one-dimensional. Behind the precursor shock, there are transverse shocks that intersect with the precursor shock, forming triple points. These triple points represent localized regions of high pressure and temperature, aiding in the stabilization of the detonation wave. Furthermore, these triple points accelerate local reaction rates.

The traces of triple points in a stable detonation are shown in Figure 2.10. These traces form a "Fish Scale" pattern.

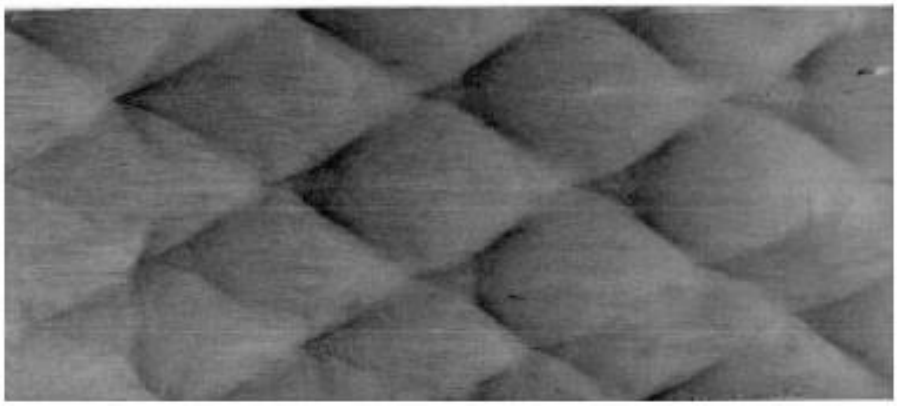

Figure 2.10. Fish Scale pattern of $2H_2$-O_2-17Ar at 20kPa ve 295K Temperature

Source: Austin & Shepherd,2003:73-90.

On the other hand, there is also unstable detonation, as shown in Figure 2.11 taken from (Khokhlov, Austin, Pintgen, & Shepherd,2004).

Figure 2.11. Fish Scale with Unstable Detonation

Source: Khokhlov vd.,2004:792.

The unstable behavior described above can be observed in all experimentally conducted explosion waves (Fickett and Davis,2001). The reason for this instability is that the explosion front in the ZND model (Figure 2.5) is not assumed to be one-dimensional but three-dimensional, exhibiting oscillatory motion.

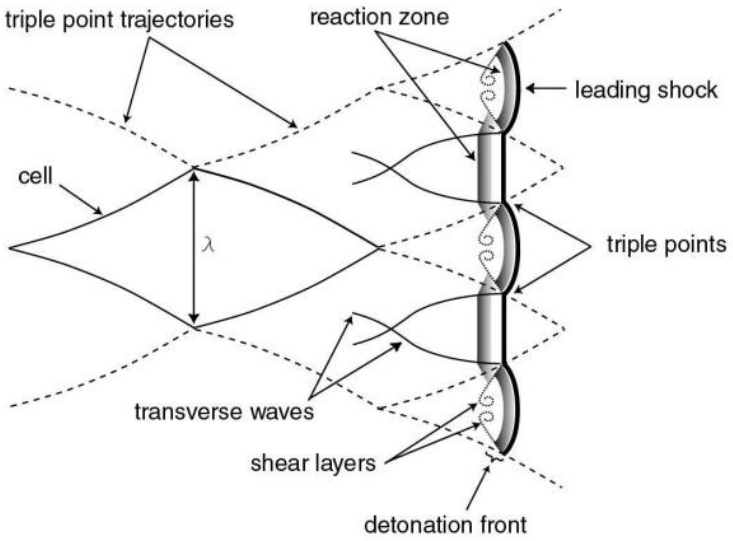

Figure 2.12. Cellular Structure of the Detonation Front

Source: Wintenberger,2004:11.

The main parameter that describes the dynamic properties of detonation waves is claimed to be the cell width λ (Lee,1984). The cell width (λ) is considered a characteristic length scale of the mixture and measures the transverse wave spacing. As seen in Figure 2.12, the triple point traces form a cellular pattern that defines the cell width λ. The leading shock front at the beginning of the cell is stronger than the shock front at the end of the cell because there are fewer transverse wave collisions. The high-temperature chemical processes behind the leading shock accelerate, shortening the reaction zone. The cell width (λ) provides the critical tube diameter, the minimum energy required for direct initiation of the detonation, and the minimum tube diameter for sustaining a stable detonation. Critical conditions can be estimated using correlations obtained experimentally or observationally based on the cell width (λ) (Lee,1984).

2.7. Detonation Wave Content

Let us consider a tube filled with a combustible gas mixture and closed at one end. A laminar flame wave with a certain flame speed is formed upon ignition at the closed end. This creates fluctuations and vortices at the flame front, increasing the combustion surface area. Consequently, the speed and acceleration of unburned gases are further increased, leading to the formation of strong compression waves. Subsequently, a small explosion occurs, and the shock wave automatically ignites the reactants, creating a powerful shock.

The unstable detonation wave transforms into a stable wave with automatic ignition. At this point, the energy obtained from shock compression and heating-induced chemical

reactions is sufficient to sustain the explosion (Glassman & Yetter,2008). The transition to detonation can occur in a straight-walled tube of sufficient length, but it is possible to shorten this transition both in length and time. Adding various obstacles and rough walls increases turbulence, significantly reducing the transition time to detonation.

2.8. Detonation Transition

Detonation waves can be created directly or through a transition to detonation. This is typically achieved by high-energy spark discharges, detonating cords, solid or gas explosives, or through flame acceleration methods. Direct initiation requires significant energy requirements, making it impractical for applications where power and weight are crucial, such as in aviation and aerospace. Therefore, research on detonation engines has shifted towards using shock initiation, where the explosion is directed through obstacle-shock wave interactions, as a shock initiator for the transition to detonation.

Deflagration to detonation transition (DDT) is a commonly used method that initiates an explosion with less energy compared to direct initiation. DDT is an event where a subsonic combustion wave is accelerated to become a supersonic combustion wave. Typically, the initial flame front is ignited with a relatively low-energy spark, then a flame develops. The flame increases the energy release rate, leading to the formation of powerful shock waves. One or more localized detonations are formed when these shock waves reach the critical ignition energy. These detonations interact with the shocks generated by flame acceleration, eventually coalescing to form a self-sustaining detonation wave.

2.9. Flame Acceleration Method

Various obstacles placed in the explosion tube have been found to expedite the transition to detonation and reduce the time and distance required. These obstacles introduce turbulence and pressure fluctuations into the flow, creating an effect. This accelerates the transition to detonation, lowering the shock formation time. The Shchelkin spiral is the most common method used to partially block the combustion chamber to accelerate DDT. The blockage ratio (BR) is the most crucial parameter for the spiral. The blockage ratio is shown in Figure 2.13 and is defined as the percentage of the blocked passage area by the obstacle in the explosion tube. Orifice plates are also designed to provide the same blockage ratio. However, they consist of spaced discs placed inside the explosion tube instead of a continuous spiral.

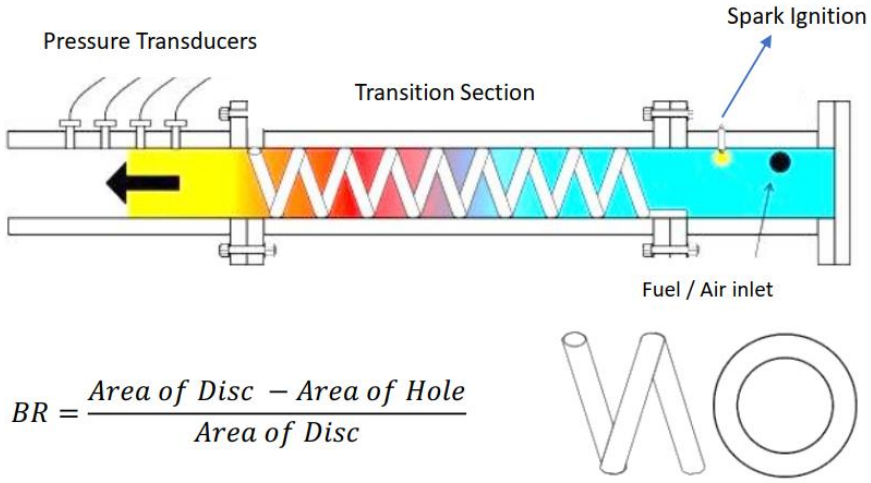

Figure 2.13. Shchelkin Spiral Scheme

Source: Tate,2015:29.

2.10. Effect of Obstacles on DDT Performance

Ongoing studies are being conducted to gain a deeper understanding of how obstacles influence performance and to enhance DDT. A study specifically examining the influence of the blockage ratio revealed that obstacles have discernible effects on DDT (Gamezo et al.,2009). The research demonstrated that obstacles of different shapes and sizes exert distinct influences on flames and shock waves.

Studies investigating the blockage ratio's impact have shown that larger obstacles generate a more accelerated flow and flame propagation due to creating a less homogeneous flow field. This accelerated flow produces shock waves that reflect from the obstacles and eventually become strong enough to trigger the detonation. On the other hand, numerical evidence has demonstrated that more considerable obstacles weaken shock waves through diffraction, leading to hindrance in DDT (Gamezo et al., 2009).

Apart from Shchelkin spirals and orifice plates, the Naval Postgraduate School has conducted improvement studies on detonation wave initiation using vortex generator-like sweeping ramp obstacles. Interestingly, simulations and tests have shown that when a pair of 180-degree rotated sweeping ramp obstacles is used in equally spaced sets at each axial location, it results in 50% less pressure loss compared to using spirals and consistently achieves successful detonation (Brophy et al.,2012).

CHAPTER 3

MATERIAL AND METHOD

In this section, the chemical properties of the fuels used in the thesis study and the methods to be applied within the scope of the thesis are given.

3.1. Fuels

In this thesis, commonly used fuels in aerospace propulsion systems such as Acetylene, Ethylene, Ethane, Methane, Kerosene, and cryogenic Hydrogen have been selected. The chemical kinetic properties of the fuel play a significant role in determining the formation time, pressure, temperature, and velocity parameters of the shock wave.

3.1.1. Acetylene

Acetylene is the simplest alkyne hydrocarbon with the chemical formula C_2H_2. This gas ignites at high temperatures during the combustion process and reacts with oxygen, producing combustion products such as CO_2 and H_2O. Due to its high energy yield during the combustion process, it is used as a fuel.

Acetylene gas is widely used in welding, cutting, and thermal processing industries due to its high heat resistance, corrosion resistance, and ability to provide a dense heat source. It is commonly employed in applications such as metalworking, where its intense flame temperature is highly valuable. Additionally, acetylene is extensively used in oxyacetylene welding and cutting torches, serving as fuel and oxygen sources for the combustion process, making it a versatile and widely used gas in industrial applications.

Table 3.1. Properties of Acetylene Fuel

Molecular formula	C_2H_2
Molecular weight	26.04 g/mol
Boiling point	-84°C (-119°F)
Freezing point	-80.8°C (-113.4°F)
Density	1.096 g/L (1 atm, 25°C)
Vapour pressure	1.0 MPa (21.1°C)
Ignition temperature	305°C (581°F)
Calorific value	49.5 MJ/kg or 1.38 MJ/L (0°C, 1 atm)

Source: NCBI, PubChem Acetylene, 2023, a.g.i.s

3.1.2. Ethylene

Ethylene is a hydrocarbon with a chemical formula of C_2H_4, and it is one of the simplest alkenes. It is a gas that is insoluble in water and lighter than air, and is used as a fuel (Saputra & Mahaputra,2022).

Ethylene can be naturally produced by plants, but it is primarily obtained from crude oil or natural gas through processes such as ethylene cracking in the petrochemical industry. The gas finds widespread use in various industries, including plastic production, agricultural chemicals, resins, oils, perfumes, the textile industry, and electrostatic coating processes (Simmons et al.,2009).

Table 3.2. Properties of Ethylene Fuel

Molecular formula	C_2H_4
Molecular weight	28.05 g/mol
Boiling point	-103.7°C (-154.7°F)
Freezing point	-169.4°C (-272.9°F)
Density	1.1785 g/L (1 atm, 25°C)
Vapour pressure	5.5 MPa (25°C)
Ignition temperature	450°C (842°F)
Calorific value	47.7 MJ/kg or 33.4 MJ/m³ (0°C, 1 atm)

Source: NCBI, PubChem Ethylene, 2023, a.g.i.s

3.1.3. Ethane

Ethane (C_2H_6) is the simplest alkane molecule making up about 90% of natural gas. It is a colorless, odorless, flammable gas and is lighter than air. Ethane is used as a fossil fuel and is also a by-product of crude oil, making it a raw material for the petrochemical industry in the production of ethylene.

Due to its low ignition temperature, ethane is an efficient fuel, resulting in less waste and exhaust gas. Additionally, the amount of carbon dioxide produced during its combustion is lower compared to other fuels. Because of these advantages, the automotive industry is researching ethane as an alternative fuel to replace gasoline and diesel. Ethane is also used in the production of polymers, serving as the primary material for plastics like polyethylene, polypropylene, and polyvinyl chloride.

Table 3.3. Properties of Ethane Fuel

Molecular formula	C_2H_6
Molecular weight	30.07 g/mol
Boiling point	-88.6°C (-127.5°F)
Freezing point	-182.8°C (-297°F)
Density	1.356 g/L (1 atm, 25°C)
Vapour pressure	4.88 MPa (25°C)
Ignition temperature	635°C (1175°F)
Calorific value	51.9 MJ/kg or 25.5 MJ/m³ (0°C, 1 atm)

Source: NCBI, PubChem Ethane, 2023, a.g.i.s

3.1.4. Methane

Methane (CH_4) is the main component of natural gas and the simplest alkane hydrocarbon. It is a colorless, odorless, and flammable gas. Methane is not only found in natural gas but is also produced during the decomposition of organic matter.

Due to its high energy content and low emission levels, methane can be used as an alternative fuel for vehicles. However, it should be noted that the combustion of methane also releases carbon dioxide gas, contributing to the greenhouse effect. Without reducing carbon dioxide emissions, the sustainable use of methane as an alternative fuel is not possible. Methane gas is used in electricity generation, heating, and cooking in homes, as well as in various industries.

Table 3.4. Properties of Methane Fuel

Molecular formula	CH_4
Molecular weight	16.04 g/mol
Boiling point	-161.5°C (-258.7°F)
Freezing point	-182.5°C (-296.5°F)
Density	0.717 g/L (1 atm, 25°C)
Vapour pressure	4.6 MPa (25°C)
Ignition temperature	537°C (999°F)
Calorific value	55.5 MJ/kg or 794 kJ/m³ (0°C, 1 atm)

Source: NCBI, PubChem Methane, 2023, a.g.i.s

3.1.5. Kerosene

Kerosene is a petroleum-derived fuel. It is synthesized by a very fine distillation of petroleum between 150°C and 270°C. Kerosene fuel is widely used in the aviation sector,

especially in jet engines of aircraft. It is also utilized for domestic heating and lighting purposes.

Table 3.5. Properties of Kerosene Fuel

Molecular formula	$C_{12}H_{23}$ (typical composition)
Surface tension	20-30 mN/m
Boiling point	150-300°C
Density	0.78-0.81 g/cm³
Ignition temperature	210°C (410°F)
Calorific value	43.1 MJ/kg or 37.6 MJ/L (20°C, 1 atm)

Source: NCBI, PubChem Kerosene, 2023, a.g.i.s

3.1.6. Hydrogen

Hydrogen is the most basic and common element in the universe. It is an odorless, colorless, and non-toxic gas. Hydrogen has the highest energy content per unit mass of all known fuels. Hydrogen fuel is considered an environmentally friendly energy source because during combustion, it only releases water vapor into the atmosphere. However, there are various challenges in storing and transporting hydrogen gas as it has a lower density than air. Additionally, the environmental impacts of the energy sources used to produce hydrogen gas should be taken into account. Hydrogen gas liquefies under 1 atm pressure and at a temperature of 20.23K. One advantage of liquid hydrogen is its higher energy density compared to hydrogen gas. This means that more energy can be stored in a smaller volume. However, storing and transporting liquid hydrogen can be difficult and expensive.

Table 3.6. Properties of Hydrogen Fuel

Molecular formula	H_2
Surface tension	0.072 J/m²
Boiling point	-252.8°C (1 atm)
Density	0.08988 g/L (0°C, 1 atm)
Ignition temperature	500°C (932°F)
Calorific value	141.8 MJ/kg or 39.4 MJ/L (25°C, 1 atm)

Source: NCBI, PubChem Hydrogen, 2023, a.g.i.s

3.2. Air Excess Coefficient

The mass ratio with air/fuel mixture was calculated and defined on the 2D model.

$$\boldsymbol{\Phi} = \frac{\boldsymbol{Actual\ Amount\ of\ Air\ Entering\ the\ Cylinder}}{\boldsymbol{Minimum\ Amount\ of\ Air\ Required\ to\ Enter\ the\ Cylinder}} \qquad (\mathbf{3.1})$$

$H_{act} < H_{min}$ $\Phi < 1$ (Fuel rich mixture; less air, more fuel)

$H_{act} = H_{min}$ $\Phi = 1$ (Stoichiometric mixture; Normal mixture)

$H_{act} > H_{min}$ $\Phi > 1$ (Fuel-poor mixture; too much air and not enough fuel)

$$nC_xH_y + O_{min} * \Phi * O_2 \rightarrow aCO_2 + bH_2O + cO_2 \quad (3.2)$$

$$O_{min} = x + \frac{y}{4} \quad (3.3)$$

$$\Phi = \frac{1}{\varphi} \quad (3.4)$$

$$KOC_xH_y = \frac{(x * n * M_{a,C}) + (y * n * M_{a,H})}{(x * n * M_{a,C}) + (y * n * M_{a,H}) + (O_{min} * \lambda * 2 * M_{a,O})} \quad (3.5)$$

$$KOO_2 = \frac{(O_{min} * \lambda * 2 * M_{a,O})}{(x * n * M_{a,C}) + (y * n * M_{a,H}) + (O_{min} * \lambda * 2 * M_{a,O})} \quad (3.6)$$

3.3. Pre-Detonator

In this thesis, the pre-detonator was analysed using 5 different blocking ratios, 6 different fuels and 3 different equivalence ratios.

3.3.1. Geometry

The geometry used in this thesis study is depicted in Figure 3.1. The geometry is divided into two sections with a diaphragm, namely the driver and the driven section. The variation of the obstacle's blockage ratio is conducted at a and b values. These a and b values are shown in Table 3.7.

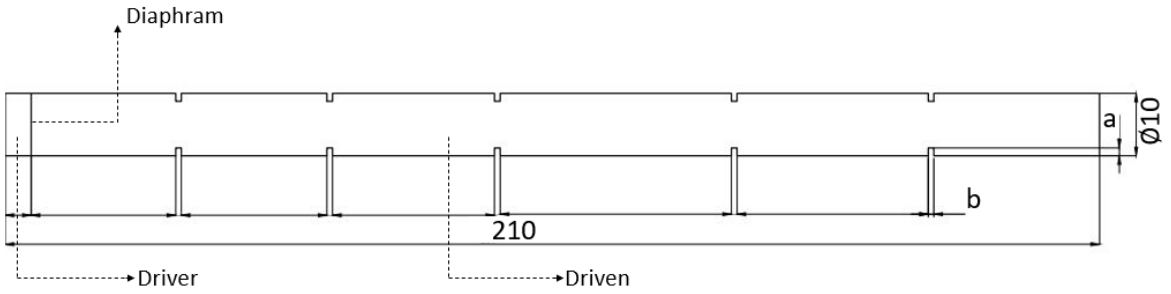

Figure 3.1. The Geometry of the Pre-Detonator

Table 3.7. The Geometry Features

Blockage Ratio	
a (mm)	b (mm)
0.50	2.18
0.75	2.18
1.00	2.18
1.25	2.18
1.50	2.18

3.3.2. Mesh

Meshing is a concept used to discretize the geometry of an engineering problem solved using numerical methods such as the Finite Element Method (FEM) or the Finite Volume Method (FVM). Using these methods, a mathematical model of an object, structure, or system is constructed. In this model, the object, structure, or system is divided into small elements (e.g., triangles, rectangles, or quadrilaterals) or cells (e.g., cubes or cylinders). This mathematical model can then be analyzed using different physical laws and equations. Meshing helps in preparing the discretized geometry for numerical analysis and ensures accurate modeling of the engineering problem.

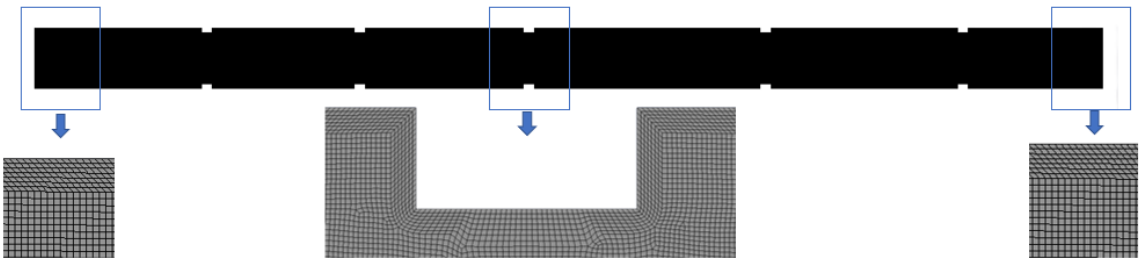

Figure 3.2. The Geometry Mesh Structure

3.3.2.1. Mesh Independence

A mesh independence study is used in finite element analysis to identify sources of errors and ensure accurate results from the finite element model. Determining the optimal values of discretization parameters for the finite element model helps improve the accuracy of the analysis. In this thesis, the mesh independence study was conducted at three different levels, and the changes in pressure values were used as the basis for the assessment. The comparative values of pressure, temperature, velocity, and Mach number for the geometry

with the highest blockage ratio are presented in Table 3.8. These values were obtained using the number of elements corresponding to the first row to save cost and time.

Table 3.8. Mesh Independence

Number	Node	Elements	P[Pa]	T[K]	V[m/s]	M
1	1170925	1165411	4207950	8831.94	1268.6	1.09
2	1541351	1532011	4207870	8915.33	1259.55	1.08
3	2740934	2732498	4207940	8843.48	1276.10	1.10

3.3.2.2. Mesh Quality Values

Mesh quality values are criteria used to evaluate the geometric quality of the mesh in numerical methods such as the finite element method or the finite volume method. Mesh quality affects the accuracy, stability, and precision of calculations in finite element analysis.

Aspect Ratio: The aspect ratio of each triangle or quadrilateral element in the mesh is calculated by dividing the longest side by the shortest side. The lower the aspect ratio, the higher the quality of the element.

Skewness: Skewness measures the differences in interior angles of triangles or quadrilateral elements in the mesh and is used to evaluate asymmetry. The lower the skewness, the higher the quality of the element.

Orthogonal Quality: Orthogonal quality measures whether the elements in the mesh are well-aligned. It takes the highest value when the edges of the elements are perpendicular to each other. This criterion can be used to create a smoother mesh.

Element Quality: The element's quality is assessed based on factors such as its surface area, volume, corner angles, and edge lengths, which determine its geometric accuracy.

The acceptable ranges of mesh quality values can vary depending on the type of application and the accuracy requirements. Although different sectors may have different acceptable ranges, the general ranges are as follows:

- Element Quality: 0.3-0.9

- Aspect Ratio: 0.1-10

- Skewness: 0-0.95

- Orthogonal Quality: 0.1-0.7

The mesh quality values for the geometry performed in this thesis are available in Table 3.9.

Table 3.9. Geometry Mesh Quality

Mesh Parameters	Value
Element Quality	0.422
Aspect Ratio	2.81
Skewness	0.64
Ortagonal Quality	0.574
Elements	1165411
Nodes	1170925

3.3.3. Setup Steps

The models and methods used in this work are explained below.

3.3.3.1. Solver Type

The base flow solver types are numerical simulation methods used in the field of Fluid Mechanics. These methods model the motion of fluids through mathematical equations and computational techniques. This introduction aims to provide an overview that will help in understanding the density-based velocity-density coupling (coupled solver) and density-based velocity-density segregation (segregated solver) models. (Fluent,2021:891-955)

3.3.3.1.1. Pressure Based

The pressure-based solver type utilizes the relationships between pressure and velocity fields to calculate fluid flow. This solver type is based on an iterative loop, where the pressure field is iteratively solved to update the fluid velocities. In the pressure-based solver, the pressure and velocity fields are interdependent. Initially, the pressure field is predicted, and using this prediction, the velocity field is calculated. Then, the velocity calculations are corrected to ensure the velocity field returns in a compatible manner to the pressure field, based on the continuity equation. The iteration loop continues until a balance is achieved between the pressure and velocity fields. In each iteration, the velocity field is updated, and these updates have an effect on the pressure field. This process is repeated until the flow stabilizes and achieves correct velocity and pressure distributions. The pressure-based solver is commonly used for incompressible flows. It assumes a constant fluid density and calculates the pressure field accurately to determine fluid velocities. Pressure-based

solvers are widely used in various industrial flow problems and offer an effective approach to solve most of them. (Fluent,2021:892-926).

3.3.3.1.2. Density Based

The density-based solver utilizes the relationships between density and velocity fields to calculate fluid flow. This solver type takes into account changes in fluid density and calculates pressure and velocity fields together. Density-based solvers are primarily used for compressible flows, where the fluid density is affected by variables such as pressure and temperature. Therefore, density-based solvers simultaneously calculate other flow variables such as velocity, pressure, and temperature, in addition to density. These solvers accurately model the compressibility of the fluid, making them suitable for analyzing high-speed gas flows and shock waves. Density-based solvers are commonly used in fields like aviation, rocket engines, and supersonic flows.

Density-based solvers employ different mathematical methods to solve the relationships between fluid density and velocity. Among them, there are approaches such as density-based coupled solver and density-based segregated solver. These methods are chosen based on the flow problem and requirements. (Fluent,2021:926-954).

3.3.3.2. Turbulence Model Selection

The selection of a turbulence model will depend on various factors such as the physical characteristics of the flow, the desired level of accuracy, available computational resources, and the time available for the simulation. To choose the most suitable model for your application, it is essential to understand the characteristics and limitations of different turbulence models. It's impossible to definitively declare the best model for a specific application, but there are general guidelines that can aid in selecting the correct turbulence model for flow simulation. Reynolds-Averaged Navier-Stokes (RANS) models offer an economical approach to calculate complex turbulent industrial flows. Typical examples of these models include various forms of k-ε or k-ω models. RANS models cover a wide range of applications, from low-speed to high-speed flows. These are suitable for many engineering applications, including surface friction, heat transfer, and pressure drop calculations, and they generally provide the required level of accuracy. By understanding the flow physics and the specific needs of your simulation, you can make an informed decision on which turbulence model to use. It is also common practice to perform sensitivity

analyses using different turbulence models to assess the impact on results and choose the most appropriate one for your specific case. (Fluent,2021:41-157).

3.3.3.2.1. One Dimensional Spalart-Allmaras Model

The Spalart-Allmaras model is a one-equation model for kinematic eddy (turbulence) viscosity that solves a modeled transport equation. It is specifically designed for aerospace applications involving wall-bounded flows, and it has been found to produce good results for boundary layers exposed to adverse pressure gradients. The model is also widely used in turbomachinery applications. However, it is not recommended for general-purpose use as it is not well-calibrated for free flows (e.g., it may produce significant errors for jet flows). The Spalart-Allmaras model is automatically computed for values corresponding to the logarithmic layer from wall functions in the range of $1<y+<30$ (Enhanced Wall Treatment - EWT), and from the viscus sublayer formulations (Launder, et al.,1975,68(3),537-566.; Fluent,2021:44-49).

3.3.3.2.2. K-ε Model

The k-epsilon model is a type of Reynolds-averaged Navier-Stokes (RANS) equation used in the modeling of turbulent flows. These equations are fundamental equations that describe the motion of fluids, and since their direct solutions are not feasible, numerical methods are employed as solution techniques for these equations. In the modeling of turbulent flows, the k-epsilon model calculates the values of turbulent kinetic energy (k) and turbulent dissipation rate (epsilon) of the fluid. The kinetic energy (k) represents the kinetic energy of the moving particles in the fluid, while turbulent dissipation (epsilon) represents the energy loss due to turbulence. The k-epsilon model calculates the effect of turbulence using two equations: k and epsilon. The kinetic energy (k) equation defines the fluid's kinetic energy and calculates the turbulence intensity. The turbulent dissipation (epsilon) equation, on the other hand, calculates the turbulence's energy loss. In the k-epsilon model, the values of k and epsilon are computed using transport equations. These equations enable the values of k and epsilon to be written in a form that can be solved alongside the Navier-Stokes equations, which describe the fluid motion along with other fluid properties. (Wilcox,1998,pp.103-207;Fluent,2021:49-60).

3.3.3.2.3. K-ω Model

The K-omega model is a type of turbulence model used in the software to simulate the behavior of turbulent flows. This model has a wide range of applications depending on the variations of turbulence in the flow field. It is particularly effective in simulating swirling flows, unstable flows, and flows in regions with high turbulence intensity. The K-omega model attempts to model the characteristic features of turbulent flow by considering the viscosity effects of the flow. In this model, the turbulence intensity and turbulence viscosity are calculated based on the flow's velocity gradients, aiming to accurately simulate the turbulent characteristics of the flow. The K-omega model uses two additional variables, k and omega (ω), to represent the turbulence effects. The variable k represents the turbulent kinetic energy, indicating the magnitude of fluctuations in the fluid's velocity. On the other hand, omega (ω) is used to represent the dissipation of turbulence kinetic energy. By accounting for the effects of viscosity and turbulence, the K-omega model provides an effective way to simulate turbulent flows accurately. It is a valuable tool for various applications in which turbulent flows play a significant role in determining the flow behavior. (Fluent,2021:61-77).

3.3.3.3. Species

The "species" combustion section refers to the part where fuel and oxygen blend, initiating combustion reactions that result in the formation of products. This section is used to perform the simulation of the combustion process. In the species combustion section, chemical reactions and combustion models representing the combustion process of fuel and oxygen are defined. These definitions are made based on the type of fuel, the method of oxygen supply, the properties of the combustion environment, and other parameters. Combustion modeling typically employs chemical kinetic models, which include the mathematical expressions of chemical reactions to calculate the reaction rates and product formation during combustion. In addition, the mixture of fuel and oxygen is utilized along with defining mixture fractions, heat values, combustion products, and other relevant parameters. The species combustion section is used to calculate combustion rates, temperature distributions, emissions, and other combustion characteristics of the fuel combustion process. This allows for the analysis of combustion performance and emission profiles of different fuels and the optimization of combustion systems. (Fluent,2021:221-271).

3.3.3.3.1. Species Transport

Software can model the mixture and transport of chemical species by solving conservation equations that define convection, diffusion, and reaction sources for each species type. The Species transport model is used to model the transport of different species in multi-component fluid systems. For instance, it is important to model the transport of different species in scenarios such as fuel-air mixtures, combustion reactions, or chemical reactions. The Species transport model solves separate mass and energy equations for each species to determine their concentration distributions. This model takes into account the effects of diffusion (transport) and convection (transport dependent on flow). As a result, the impact of different species on density, temperature, and other properties can be examined. The Species transport model finds applications in various industrial processes. For example, it plays a crucial role in analyzing combustion and gasification processes, emission control, chemical reactions, and catalysis. It serves as a powerful tool to understand and optimize the distribution and interactions of species in fluid systems (Fluent,2021:221-271).

3.3.3.3.2. Non-Premixed Combustion

The fuel and oxidizer reach the reaction zone through distinct injectors or zones in non-premixed combustion. This is the opposite of premixed systems, where reactants are mixed at the molecular level before combustion. In this case, the fuel and oxygen do not mix directly before combustion; instead, the combustion mechanism occurs as a result of the interaction between the fuel and oxygen within the combustion zone, leading to the formation of products. The non-premixed combustion model finds applications in various industrial processes. For instance, it is used in simulations of fuel combustion in systems such as pulverized coal furnaces, diesel internal combustion engines, pool fires, gas turbines, furnaces, boilers, combustion chambers, and combustion engines. This model is utilized to evaluate the effects of fuel and air mixing conditions on combustion performance and emissions (Fluent,2021:271-309).

3.3.3.3.3. Premixed Combustion

The fuel and oxidizer are molecularly combined before ignition in premixed combustion. Combustion happens as a flame front propagates towards the unburned reactants. Spark-ignited internal combustion engines, lean premixed gas turbine combustors, and gas leakage explosions are all examples of premixed combustion. Modeling premixed combustion is more challenging compared to non-premixed combustion. This is because

premixed combustion typically involves thin, stretched, and wrinkled flames generated by turbulence. For subsonic flows, the overall flame propagation speed is determined by both laminar flame speed and turbulent eddies. The laminar flame speed is controlled by the spreading and burning rates of species and heat upwards towards the reactants. Capturing the laminar flame speed requires resolving detailed chemical kinetics and molecular diffusion processes, as well as the inner structure of the flame. The practical laminar flame thickness is in the millimeter range or even smaller, which makes it difficult to meet the resolution requirements. The effect of turbulence is to wrinkle and stretch the spreading laminar flame, increasing its surface area and, consequently, the effective flame speed. Modeling premixed combustion accurately requires accounting for these complexities (Fluent,2021:309-319).

3.3.3.3.4. Partially premixed combustion

Partially Premixed Compression Ignition (PCCI) is a combustion strategy used in internal combustion engines. In this strategy, the fuel and oxidizer do not fully mix, and the combustion process occurs partially premixed. One of the advantages of PCCI is achieving lower combustion temperatures and reduced NO_x emissions. Additionally, it aims to achieve high combustion efficiency and lower fuel consumption, similar to diesel engines. Partially premixed combustion systems involve non-uniform fuel-oxidizer mixtures (equivalence ratios) in premixed flames. These types of flames may include quiescent premixed jets, diffusion pilot flames, and/or cooling air jets in lean premixed burners. PCCI is a crucial step toward improving fuel economy and lowering emissions from internal combustion engines. However, its implementation and control are complex processes, requiring careful consideration of engine design and operating parameters. (Fluent,2021:319-336).

3.3.3.4. Solution

In this thesis study, the analyses were performed using second-order discretization equations. Second-order discretization equations provide better convergence and accurate results compared to first-order discretization equations. Below are various solution methods available in the software. In this thesis, the Simple method was used for the analyses. The Hybrid Initialization method was selected as the initialization method (Fluent,2021:891-898; Versteeg, Malalasekera:2-9).

3.3.3.4.1. Simple

The SIMPLE acronym stands for "Semi-Implicit Method for Pressure-Linked Equations." The SIMPLE method is a simplification technique used to obtain simple and sufficient results. It is based on the Navier-Stokes equations but uses fewer equations and makes certain assumptions. This method is suitable for cases where the flow is two-dimensionally planar, turbulence is neglected, or pressure drop is not considered. In the SIMPLE method, the momentum equations in the x, y, and z directions are solved separately. Then, the continuity equation is solved. Because it solves the continuity and momentum equations separately, it is called a segregated method. The advantages of the SIMPLE method include faster computation times, lower memory requirements, and the use of fewer grid points. However, it may be insufficient for more complex flow problems. Overall, the SIMPLE method is a practical approach for cases where its assumptions are valid, and it provides satisfactory results for many engineering applications (Fluent,2021:916-917; Versteeg, Malalasekera:186-191).

3.3.3.4.2. Simplec

The SIMPLEC (SIMPLE-Consistent) algorithm developed by Van Doormal and Raithby follows the identical steps as the SIMPLE algorithm, with the sole change being the manipulation of momentum equations. In the SIMPLEC algorithm, the momentum equations are manipulated to remove less important terms in the SIMPLE velocity correction equations. The discretized pressure correction equation remains the same as in the SIMPLE method. The goal of the SIMPLEC algorithm is to improve the convergence and stability of the solution while still providing efficient and accurate results. By modifying the momentum equations, the algorithm aims to achieve better consistency and convergence properties compared to the original SIMPLE method. Overall, the SIMPLEC algorithm is a modification of the original SIMPLE method and is used to solve the pressure-velocity coupling in computational fluid dynamics simulations (Fluent,2021:917-918; Versteeg, Malalasekera:193).

3.3.3.4.3. PISO

The PISO (Pressure-Implicit with Splitting of Operators) algorithm, coined by Issa in 1986, is a pressure-velocity calculation procedure developed specifically for the non-steady compressible flows to be solved without iterations. It has also been successfully adapted for iterative solutions of steady-state problems. PISO algorithm can be seen as an

extension of the SIMPLE algorithm, with an additional corrector step to further improve its performance. The algorithm consists of a predictor step and two corrector steps, making it more robust and accurate than the SIMPLE method. The pressure correction equation is solved twice in the PISO algorithm, which requires additional storage space to compute the source term for the second pressure correction. Although the PISO algorithm requires extra computational effort due to the double solution of the pressure correction, it has been observed to be efficient and fast. To stabilize the calculation process, low relaxation factors are still necessary, as in previous methods. Overall, the PISO algorithm is a powerful tool for simulating non-steady compressible flows with improved accuracy and convergence, and it provides a valuable approach to solve various fluid flow problems (Fluent,2021:918-919; Versteeg, Malalasekera:193-196).

3.3.3.4.4. Coupled

The Coupled method is a solution technique used to simulate fluid-solid interactions. In this method, the interactions between the fluid and solid materials are fully computed. It simultaneously solves the momentum and continuity equations, allowing for the exchange of momentum, heat, and mass between the fluid and solid domains. The movement and properties of the fluid are linked with the motion and heat transfer of the solid material, and they are calculated together. The Coupled method is employed to model complex fluid-solid interactions. For instance, the pressure effect exerted by the fluid on a solid surface affects the surface deformation, which in turn impacts the flow characteristics of the fluid. The Coupled solver is utilized to fully account for these interactions and obtain accurate results. In Fluent, the Coupled method can be used in combination with many other solution methods, depending on the requirements of the problem. Other approaches include loosely coupled or tightly coupled methods. By employing the Coupled method, Fluent users can accurately analyze fluid-solid interactions and apply it in various industrial applications such as automotive, aerospace, energy, and turbine design (Fluent,2021:919-926; Versteeg, Malalasekera:186-197).

3.3.3.5. Initialization Method

Before commencing a CFD simulation, it is essential to input an "initial guess" for the solution field within the software. In many cases, extra care is required to provide an initial solution that leads to the desired final solution. For example, in a real-life supersonic wind tunnel, if the back pressure is reduced only to the operating value, the flow will not

"start"; it will choke at the throat and not transition to a supersonic state. The same applies to numerical simulations: the flow must be initiated as a supersonic flow; otherwise, it will choke and remain subsonic. To overcome this, it is essential to carefully set up the initial conditions for the simulation. The initial guess should reflect an approximate representation of the physical flow and enable the numerical algorithm to appropriately adjust the initial conditions to fit the flow field. Ideally, the initial guesses should be based on information reflecting the physical reality, such as experimental data, previous simulation results, or analytical solutions. However, in some cases, it may be necessary to start with initial guesses that are far from the physical reality. In such cases, additional effort is required to iteratively refine the initial guesses to obtain an accurate solution. In conclusion, providing an appropriate initial guess is crucial for a successful CFD simulation. The initial guesses significantly impact the accuracy, stability, and convergence speed of the simulation, ensuring that the flow is initiated correctly to achieve the desired final solution (Fluent, 2013:1445).

3.3.3.5.1. Standard Initialization

This method uses default values for initializing the simulation. The values are usually set to zero or can be user-defined initial values. For example, in a flow simulation, initial values for variables such as pressure, velocity, and temperature can be set using the standard initialization. This method provides a simple and quick option for initialization compared to more complex initialization methods. However, in some cases, more precise and accurate initial values may be required, and in such situations, the standard initialization method may not be sufficient. In such cases, special initialization methods or more detailed adjustments to the initial conditions may be necessary.

3.3.3.5.2. FMG Initialization

FMG (Full Multigrid) initialization is a method developed in the Fluent software to provide a faster and more stable start for challenging convective flows, such as expanding, contracting, or spiralling flows in circular moving machinery, and in nonlinear flow problems. This method efficiently performs solution iterations to generate initial predictions for the variables in the flow field, aiming to achieve more accurate results. FMG initialization is particularly useful for large and complex geometries or flows with high Reynolds numbers. By applying FMG initialization, flow simulations can converge more quickly, helping to optimize time and computational resources. To access the FMG initialization

procedure through the text user interface (TUI), you can do so by entering the following commands: "solve," "initialize," "fmg-initialization," and responding with "yes" when prompted.

By executing these commands in the console, you can enable the FMG initialization method and benefit from its advantages in starting your flow simulation (Fluent,2013:1449-1450).

3.3.3.5.3. Hibrit initialization

Hybrid initialization is another initialization method available in Fluent. In addition to standard initialization and FMG initialization, hybrid initialization is used to determine velocity and pressure fields by solving the Laplace equation. For other variables such as temperature, turbulence, species fractions, volume fractions, and similar, values are automatically patched based on the area-averaged values or a specific interpolation scheme (Fluent,2013:1451-1452). Hybrid initialization offers a combination of approaches to efficiently initialize the flow field and ensure a stable start for the simulation. By using the Laplace equation to determine velocity and pressure, and applying appropriate interpolation for other variables, the hybrid initialization method can provide a good initial guess for the flow field, which helps in achieving convergence and accurate results in the subsequent simulations.

CHAPTER 4

FINDINGS

In this chapter, the CFD results and findings of this thesis will be discussed.

4.1. Acetylene

This chapter examines the CFD results for acetylene fuel. In our analysis, the transport of acetylene-oxygen fuel species was performed using 3 different equivalence ratios and 5 different blockage ratios with the use of patching. The results were obtained using CFD post-processing. For equivalence ratios of 0.5, 1, and 1.5, shock waves occurred with average durations of 0.131, 0.036, and 0.149 milliseconds, respectively. The time it took for the shock wave to form and exit the tube was determined to be 0.076, 0.067, and 0.070 milliseconds, respectively. Based on the analysis, it was found that the shock wave formation and tube exit times were more efficient for the equivalence ratio of 1 compared to the other ratios. Although the shock wave formed faster for an equivalence ratio of 0.5, the tube exit time was slower compared to the equivalence ratio of 1.5. It was observed that the lower equivalence ratio led to lower temperatures and pressures.

The pressure, temperature, and velocity values obtained from the acetylene-oxygen analysis are presented in Table 4.1. Upon examination of the data in the table, it is observed that the highest pressure, temperature, and velocity values belong to the equivalence ratio of 1. On the other hand, the lowest pressure, temperature, and velocity values are determined to be for the equivalence ratio of 0.5. Examining Table 4.1 for the equivalence ratio of 0.5 reveals the following maximum values: pressure at 3377.70 kPa, temperature at 6304.78 K, and velocity at 1059.45 m/s. These peaks are reached at obstacle heights of 1.25 mm, 0.5 mm, and 1.25 mm, respectively. For the equivalence ratio of 1, the pressure of 4227.71 kPa, temperature of 8940 K, and velocity of 1256.09 m/s are observed at an obstacle height of 1.5 mm. For the equivalence ratio of 1.5, these values are 3699.86 kPa, 7355.49 K, and 1133.51 m/s, respectively, occurring at obstacle heights of 0.5 mm, 1.25 mm, and 1 mm, respectively.

Table 4.1. Pressure, Temperature, and Velocity Values for Acetylene-Oxygen

Geometric Features		Molar Mass		Acetylene [0.5]		
a	b	$[C_2H_2]$	0.140	P[kPa]	T[K]	V[m/s]
0.5	2.18	$[O_2]$	0.860	3361.90	6304.78	1056.72
0.75	2.18			3341.00	6290.75	1059.35
1	2.18			3344.64	6289.71	1058.85
1.25	2.18			3377.70	6293.39	1059.45
1.5	2.18			3335.80	6303.09	1058.49
Geometric Features		Molar Mass		Acetylene [1]		
a	b	$[C_2H_2]$	0.245	P[kPa]	T[K]	V[m/s]
0.5	2.18	$[O_2]$	0.755	4209.00	8928.42	1243.03
0.75	2.18			4186.10	8920.02	1234.63
1	2.18			4187.79	8925.16	1255.16
1.25	2.18			4227.71	8927.19	1254.48
1.5	2.18			4180.62	8940.00	1256.09
Geometric Features		Molar Mass		Acetylene [1.5]		
a	b	$[C_2H_2]$	0.327	P[kPa]	T[K]	V[m/s]
0.5	2.18	$[O_2]$	0.673	3729.03	7351.08	1122.12
0.75	2.18			3687.12	7355.49	1132.21
1	2.18			3691.59	7348.05	1133.51
1.25	2.18			3689.35	7348.52	1111.26
1.5	2.18			3699.86	7349.57	1122.31

The curves for the equivalence ratios of 0.5 are presented in Figures 4.1, 4.2, and 4.3, respectively. These figures represent the time elapsed until shock wave formation. The figures 4.4, 4.5, and 4.6 presented illustrate the changes caused by the shock wave as it progresses through the tube towards the exit. The curves for the equivalence ratios of 1 are presented in Figures 4.7, 4.8, and 4.9, respectively. These figures show the time elapsed until the shock wave formed. The figures 4.10, 4.11, and 4.12 presented illustrate the changes caused by the shock wave as it progresses through the tube towards the exit. The curves for the equivalence ratios of 1.5 are presented in Figure 4.13, Figure 4.14, and Figure 4.15, respectively. These figures represent the time elapsed until shock wave formation. The figures 4.16, 4.17, and 4.18 presented illustrate the changes caused by the shock wave as it progresses through the tube towards the exit. From the figures, it is evident that the shock wave increases the pressure, temperature, and velocity of the unburned fuel as it propagates. Furthermore, the contour plots of CFD results are shown in Table 4.2, Table 4.3, Table 4.4, Table 4.5, Table 4.6, and Table 4.7. Examining Table 4.2, Table 4.4, and Table 4.6, it can be observed that the shock wave formation occurs before the first obstacle.

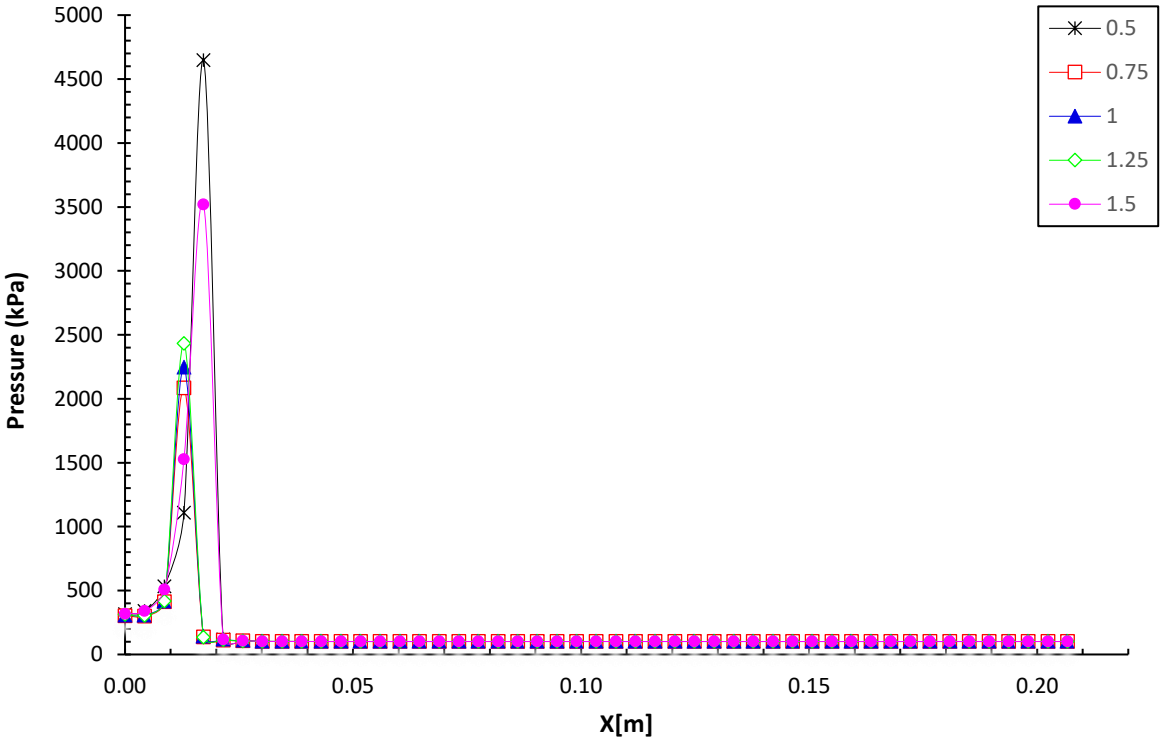

Figure 4.1. Acetylene-Oxygen Pressure Equivalence 0.5 Shockwave Starting Point

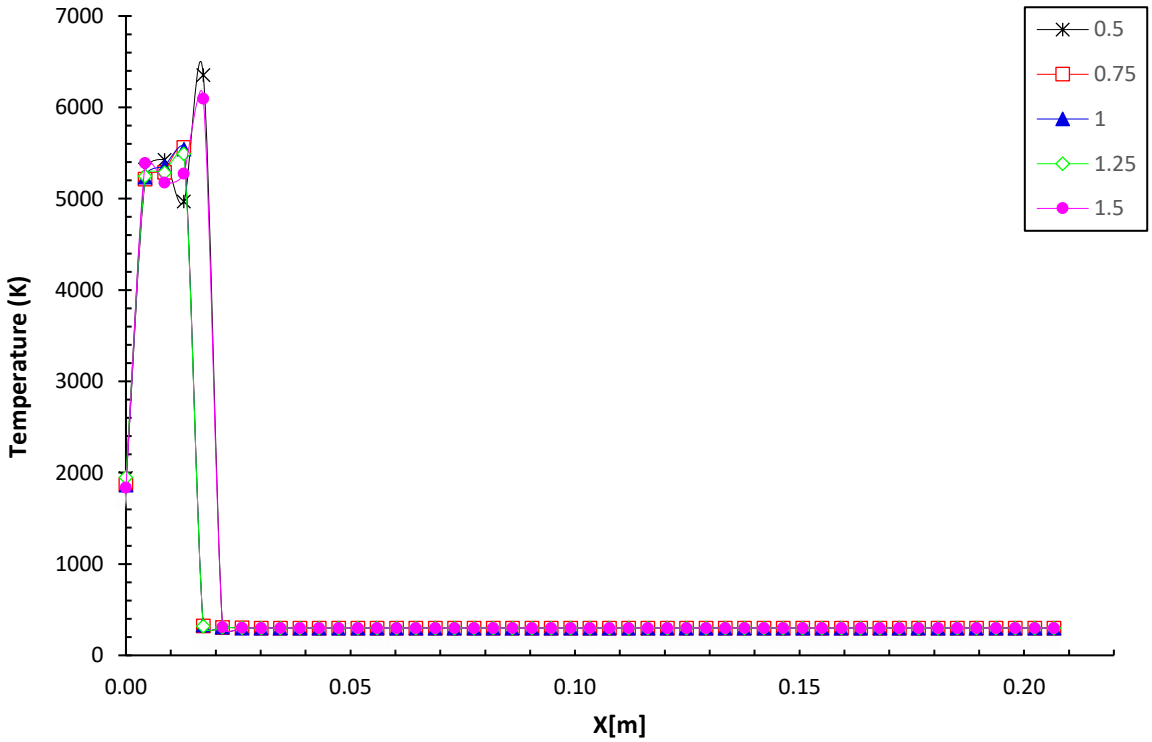

Figure 4.2. Acetylene-Oxygen Temperature Equivalence 0.5 Shockwave Starting Point

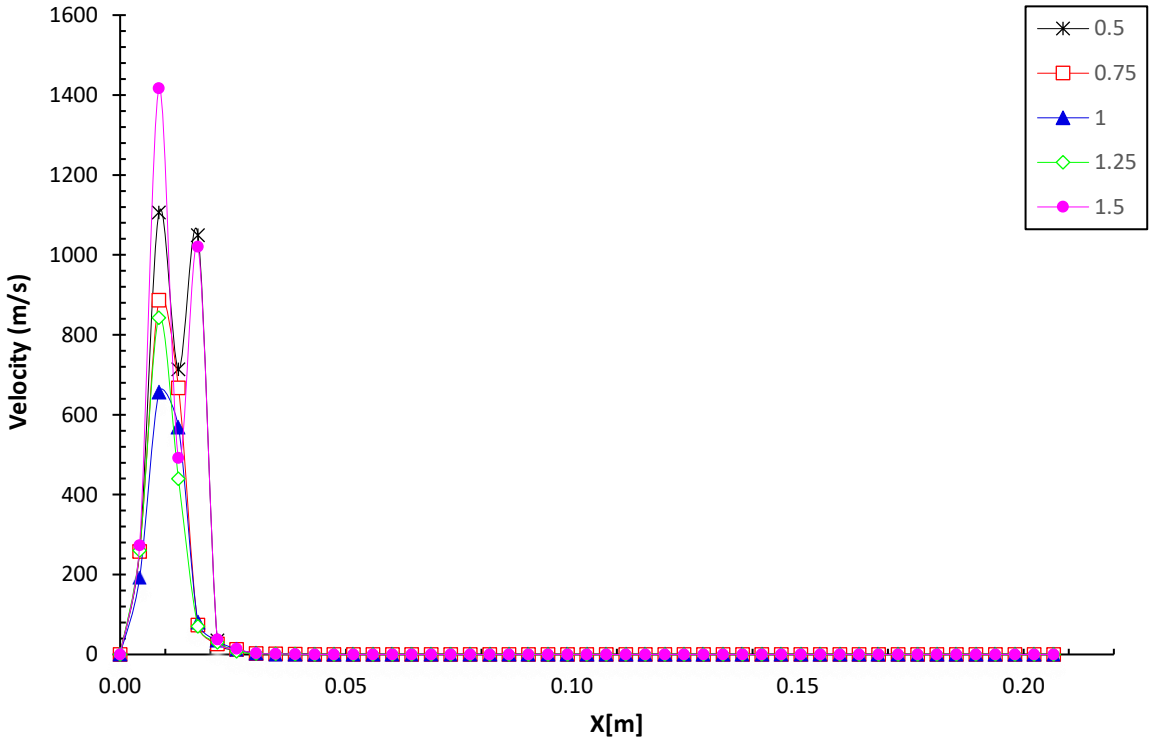

Figure 4.3. Acetylene-Oxygen Velocity Equivalence 0.5 Shockwave Starting Point

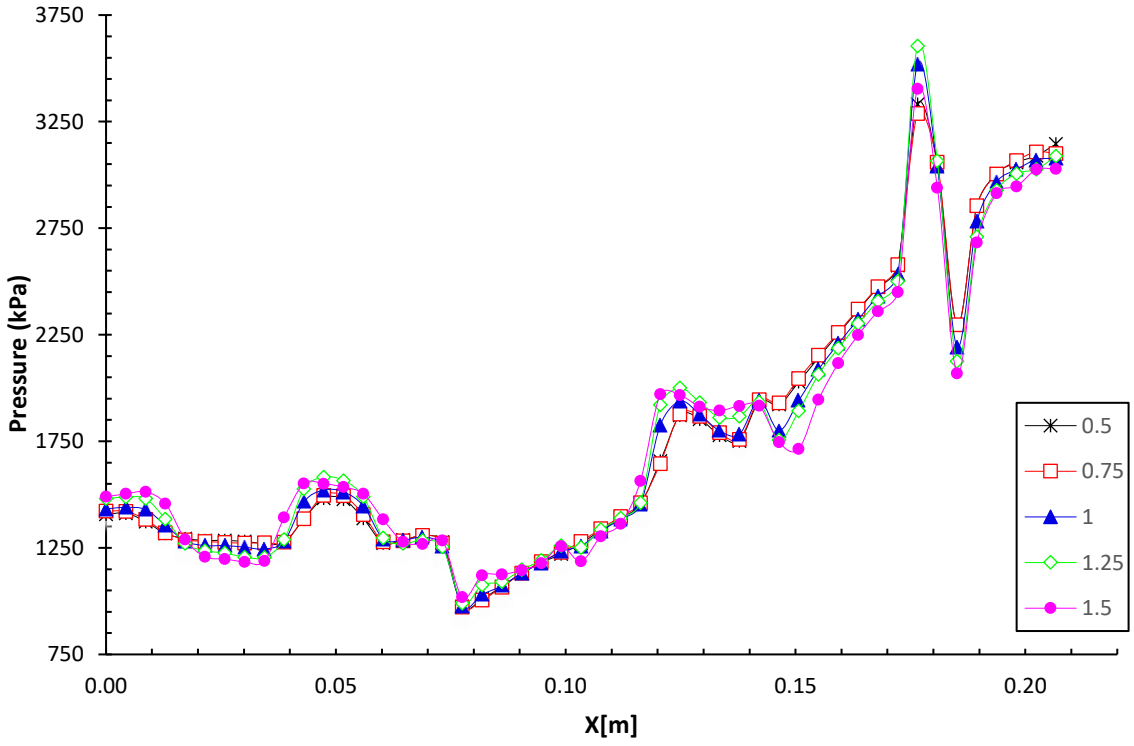

Figure 4.4. Acetylene-Oxygen Pressure Equivalence 0.5 Shockwave at the Exit of Tube

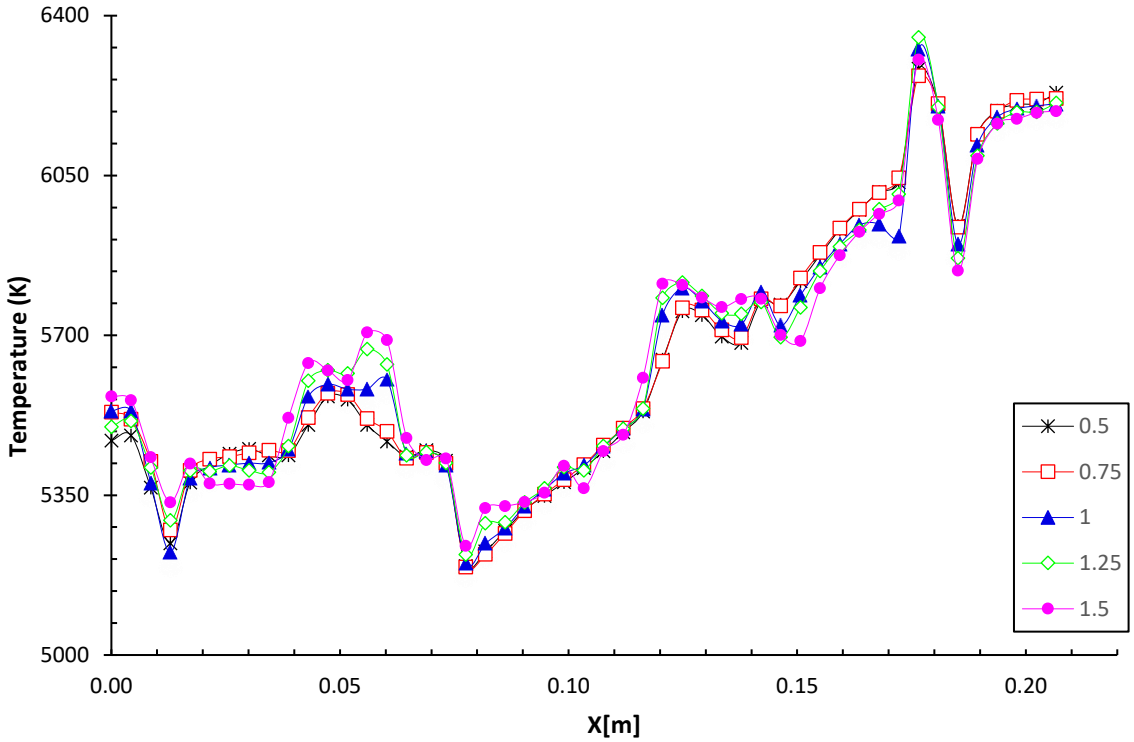

Figure 4.5. Acetylene-Oxygen Temperature Equivalence 0.5 Shockwave at the Exit of Tube

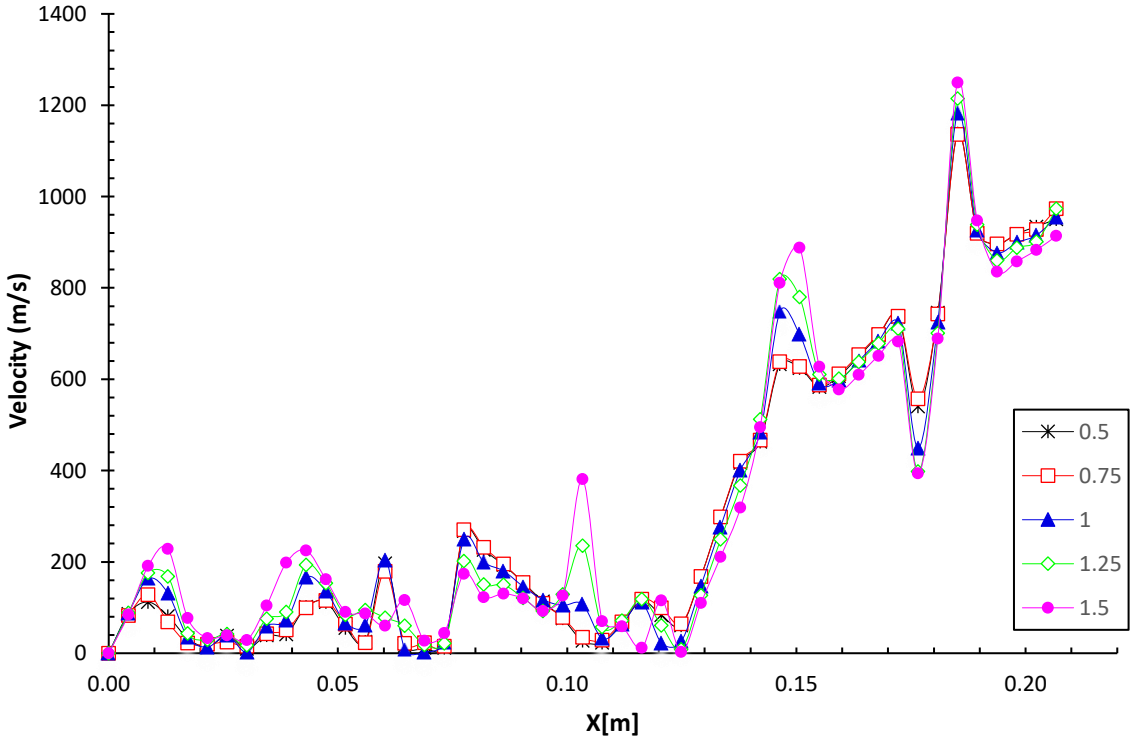

Figure 4.6. Acetylene-Oxygen Velocity Equivalence 0.5 Shockwave at the Exit of Tube

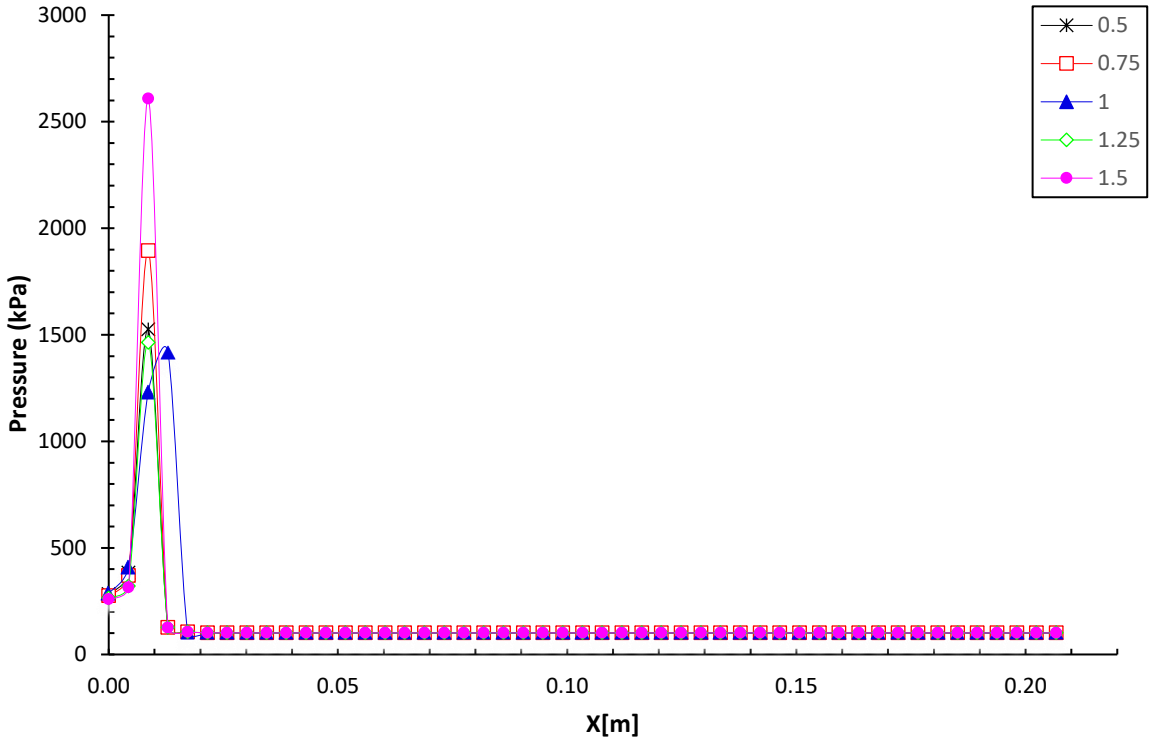

Figure 4.7. Acetylene-Oxygen Pressure Equivalence 1 Shockwave Starting Point

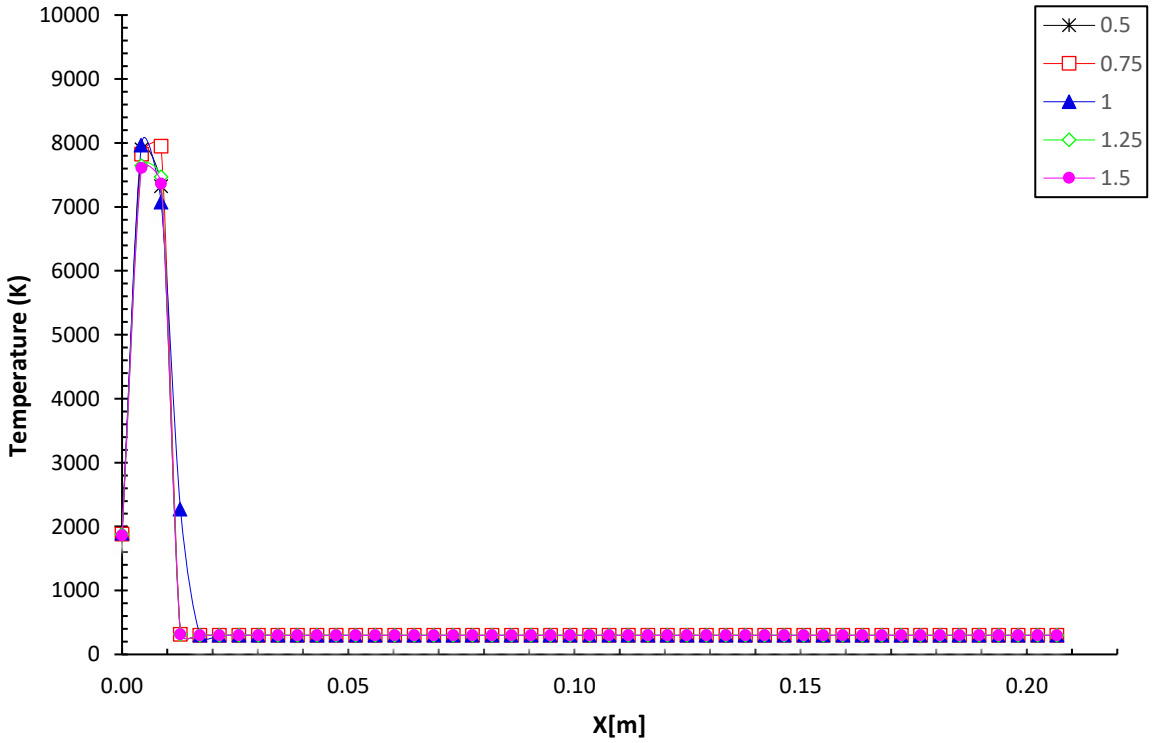

Figure 4.8. Acetylene-Oxygen Temperature Equivalence 1 Shockwave Starting Point

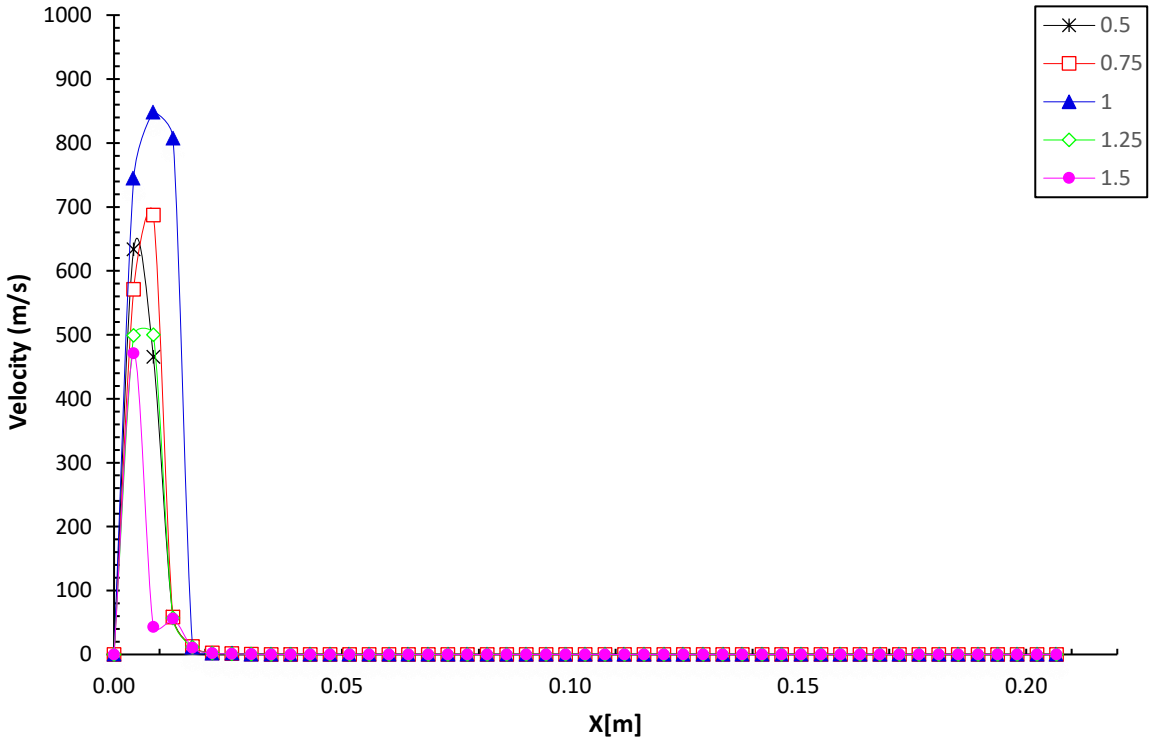

Figure 4.9. Acetylene-Oxygen Velocity Equivalence 1 Shockwave Starting Point

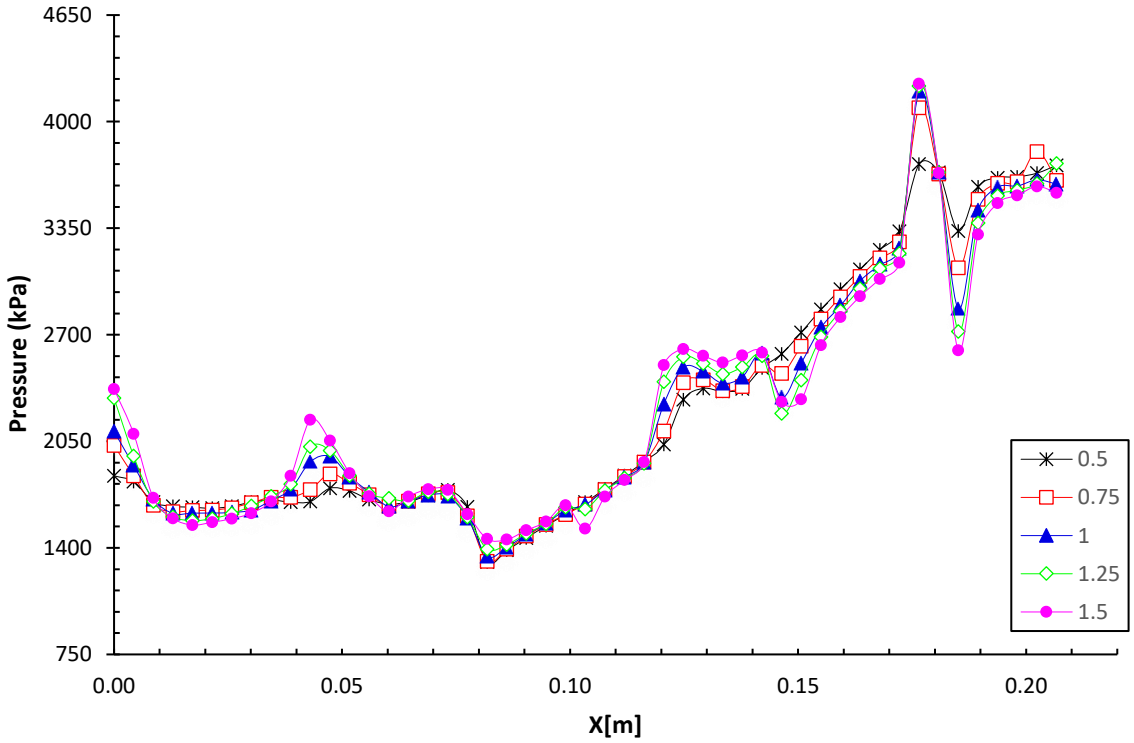

Figure 4.10. Acetylene-Oxygen Pressure Equivalence 1 Shockwave at the Exit of Tube

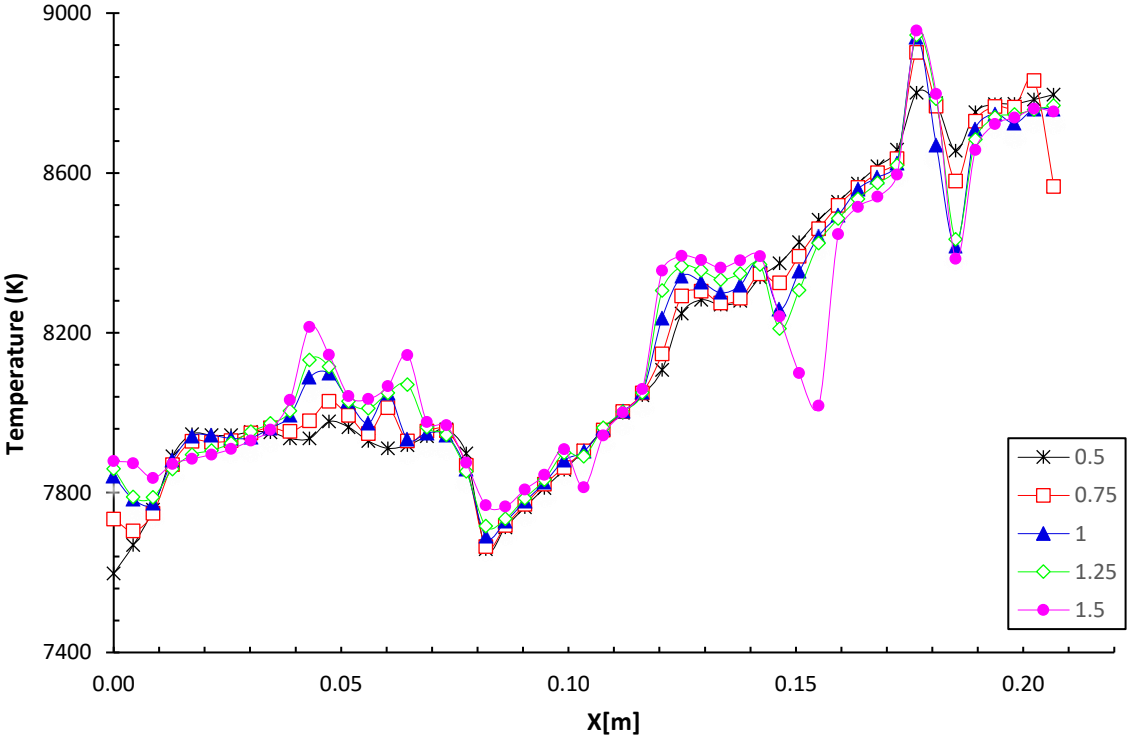

Figure 4.11. Acetylene-Oxygen Temperature Equivalence 1 Shockwave at the Exit of Tube

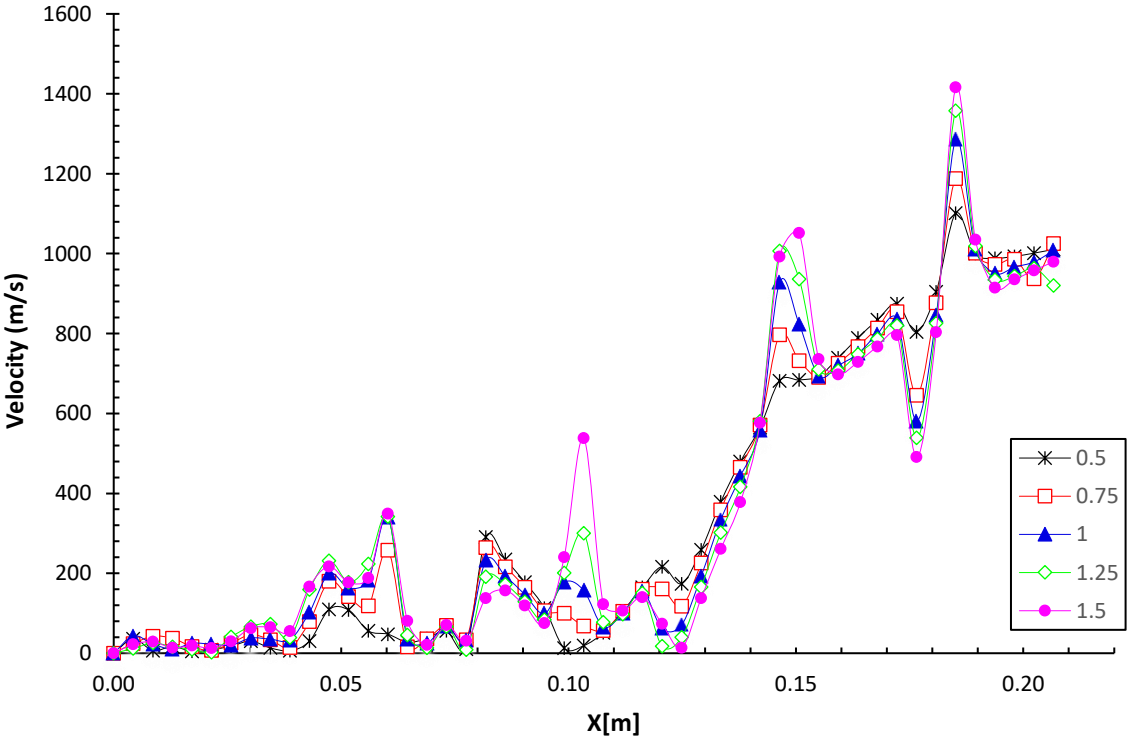

Figure 4.12. Acetylene-Oxygen Velocity Equivalence 1 Shockwave at the Exit of Tube

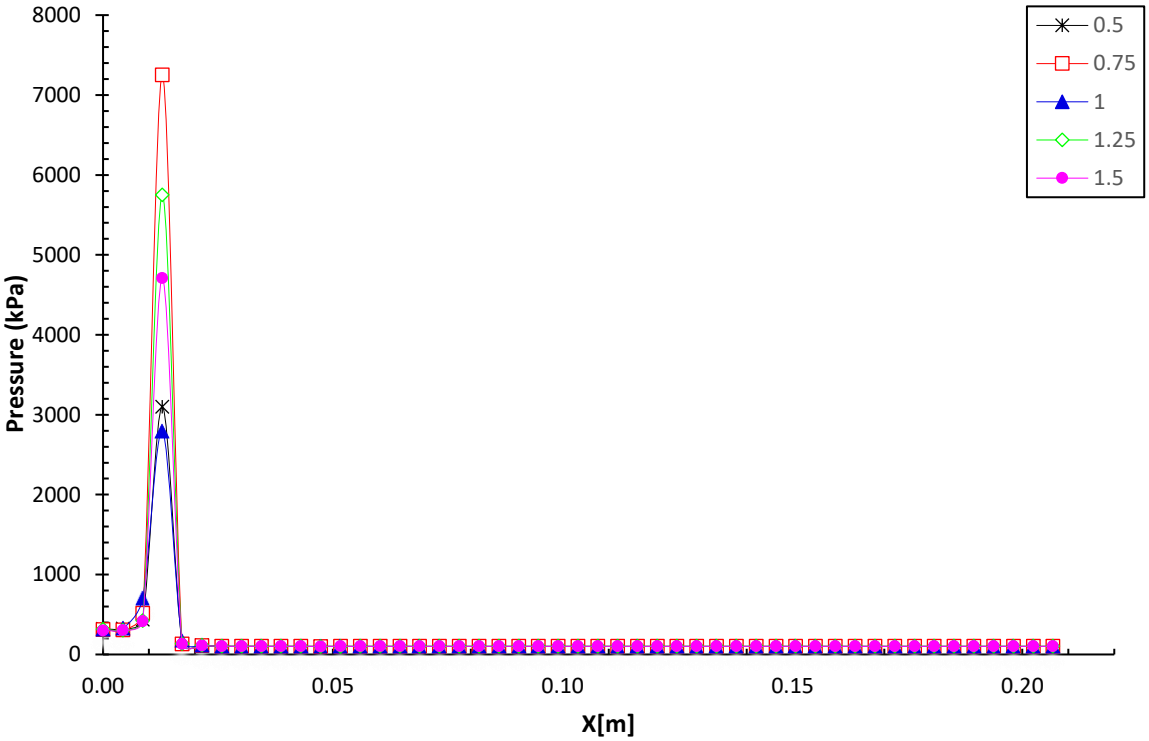

Figure 4.13. Acetylene-Oxygen Pressure Equivalence 1.5 Shockwave Starting Point

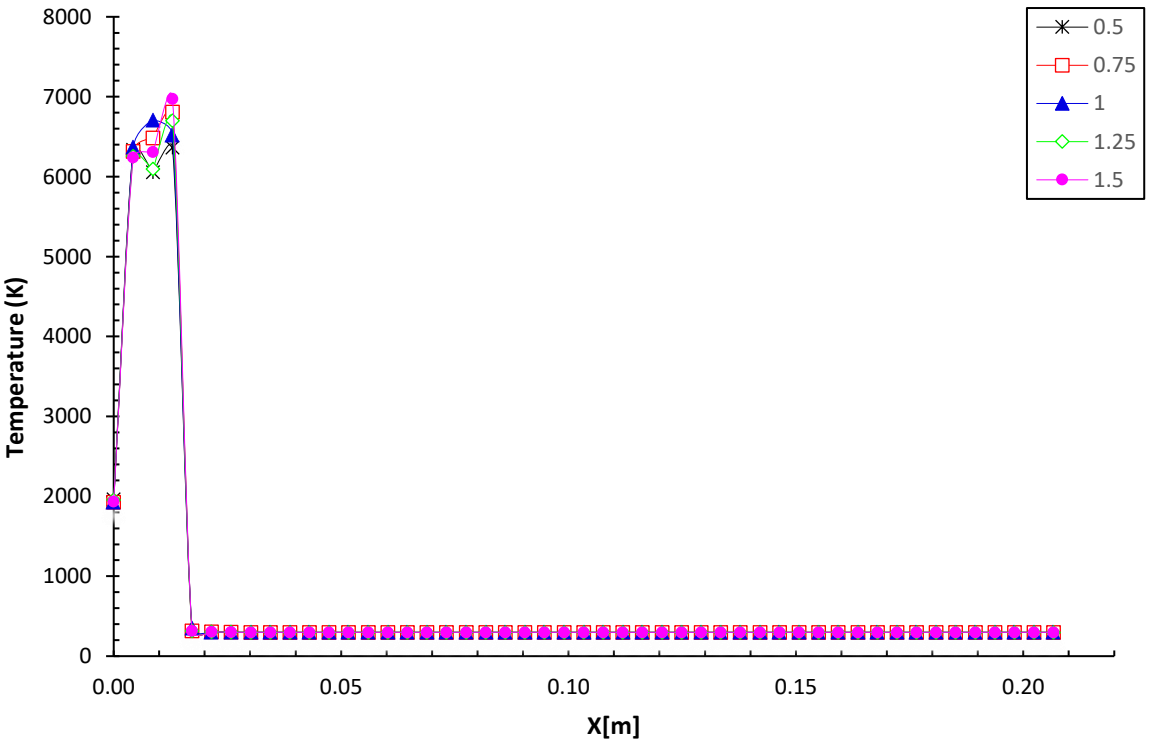

Figure 4.14. Acetylene-Oxygen Temperature Equivalence 1.5 Shockwave Starting Point

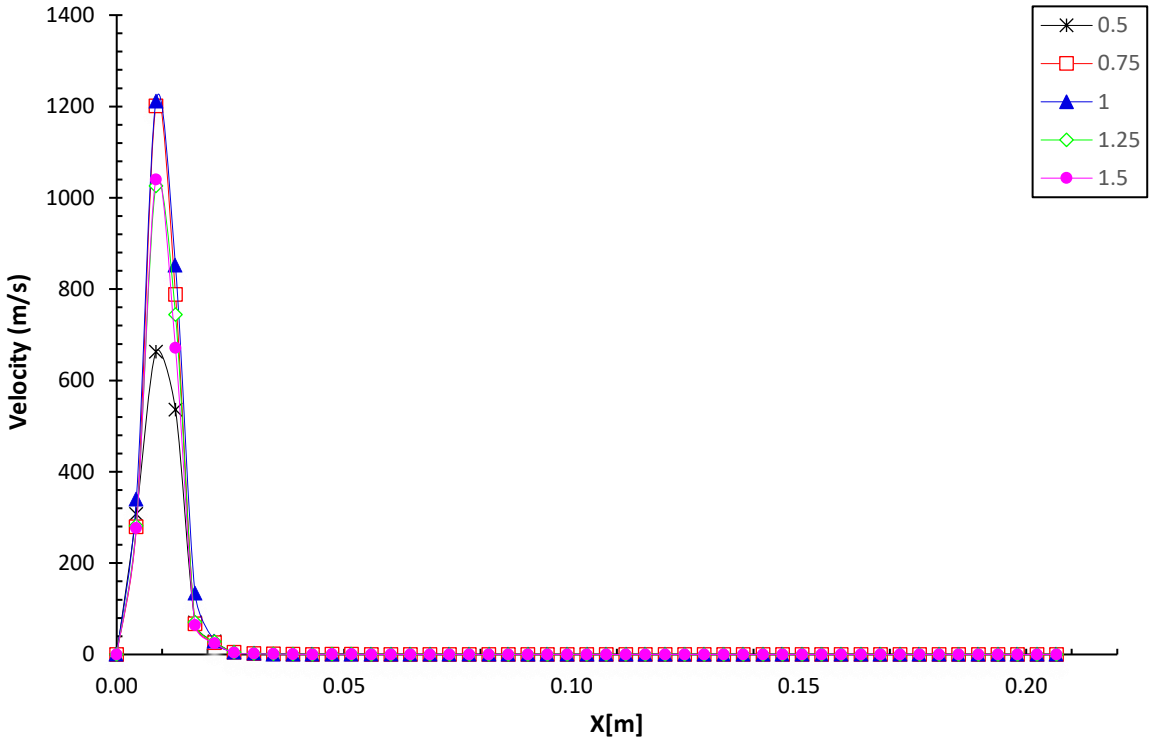

Figure 4.15. Acetylene-Oxygen Velocity Equivalence 1.5 Shockwave Starting Point

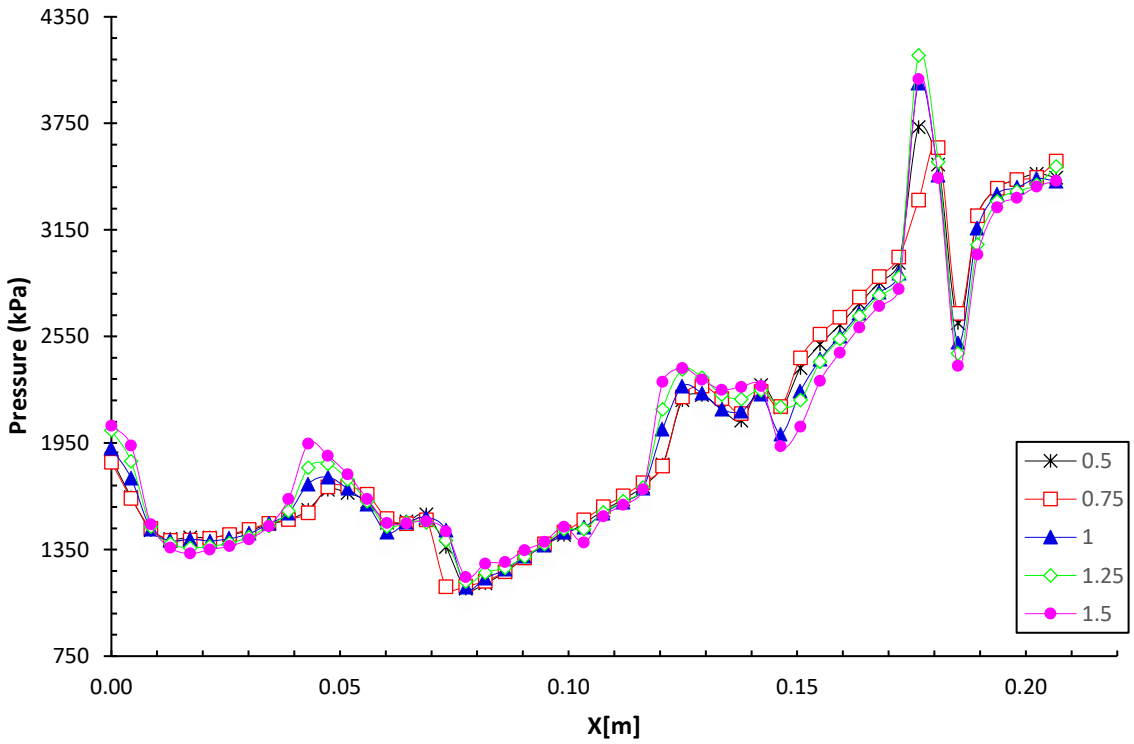

Figure 4.16. Acetylene-Oxygen Pressure Equivalence 1.5 Shockwave at the Exit of Tube

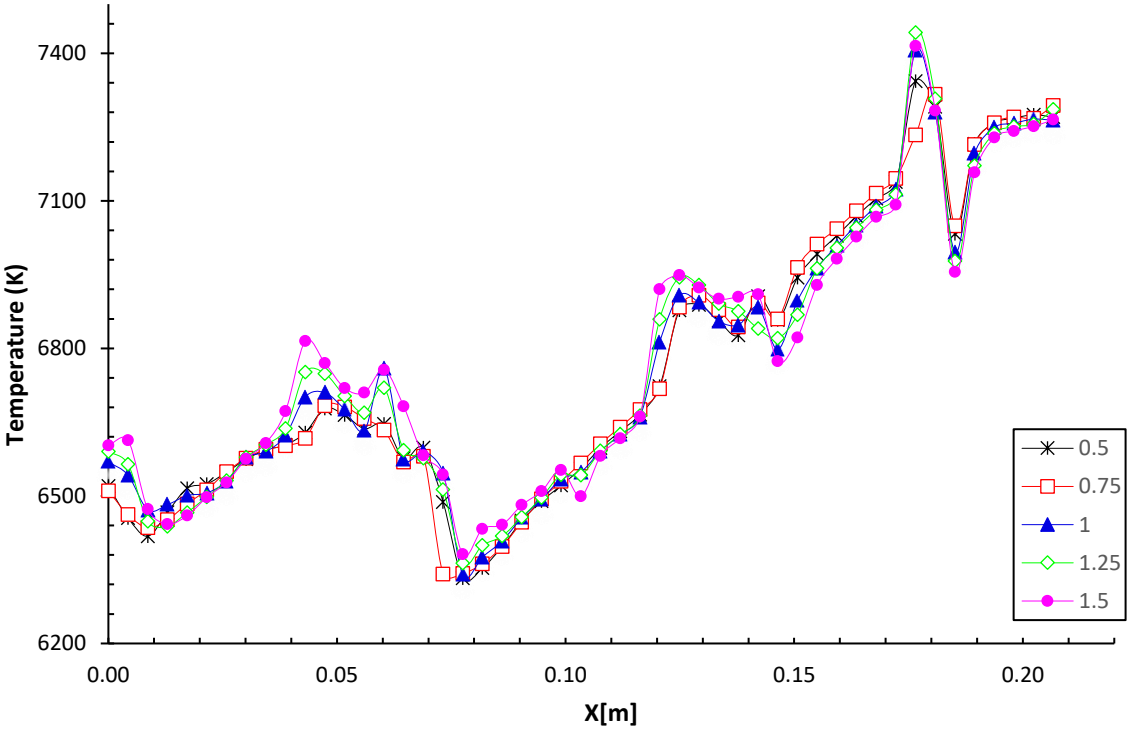

Figure 4.17. Acetylene-Oxygen Temperature Equivalence 1.5 Shockwave at the Exit of Tube

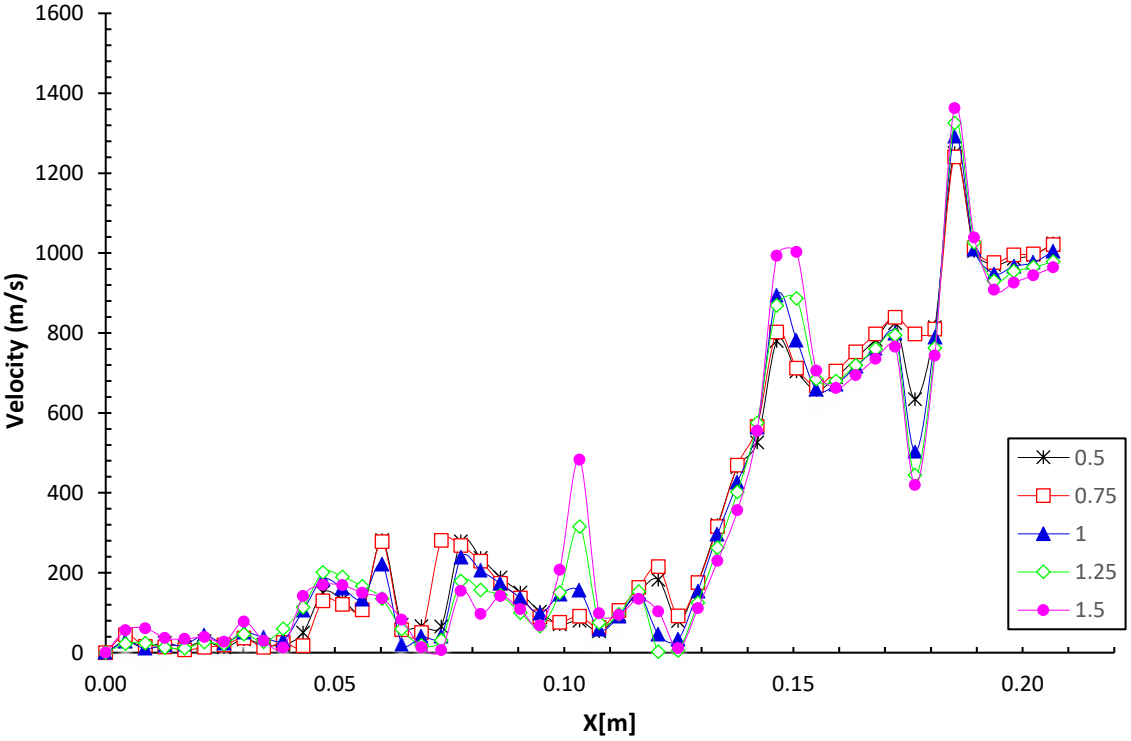

Figure 4.18. Acetylene-Oxygen Velocity Equivalence 1.5 Shockwave at the Exit of Tube

Table 4.2. Acetylene-Equivalence 0.5: Pressure, Temperature, and Velocity Contours Start

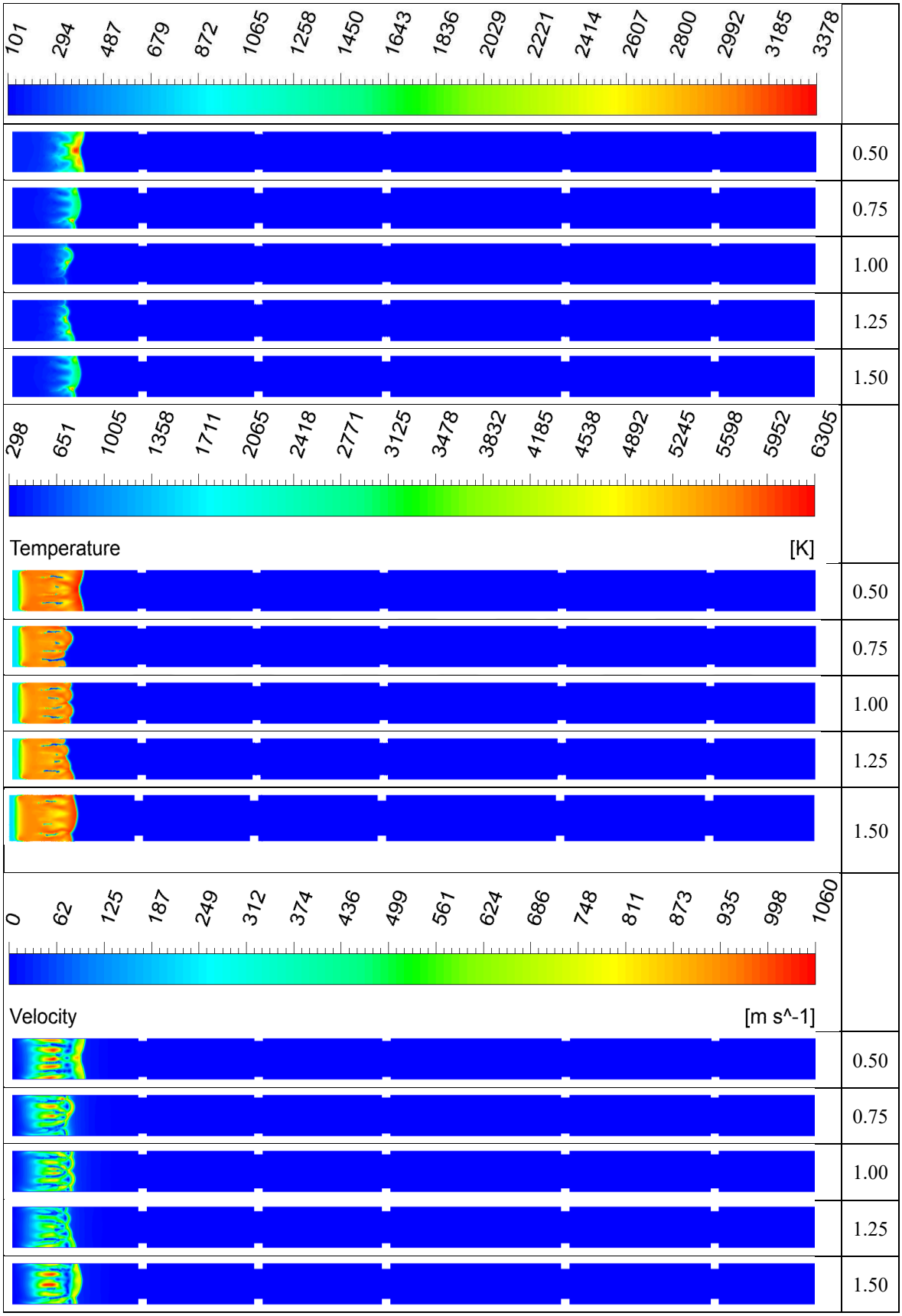

Table 4.3. Acetylene-Equivalence 0.5: Pressure, Temperature, and Velocity Contours Exit

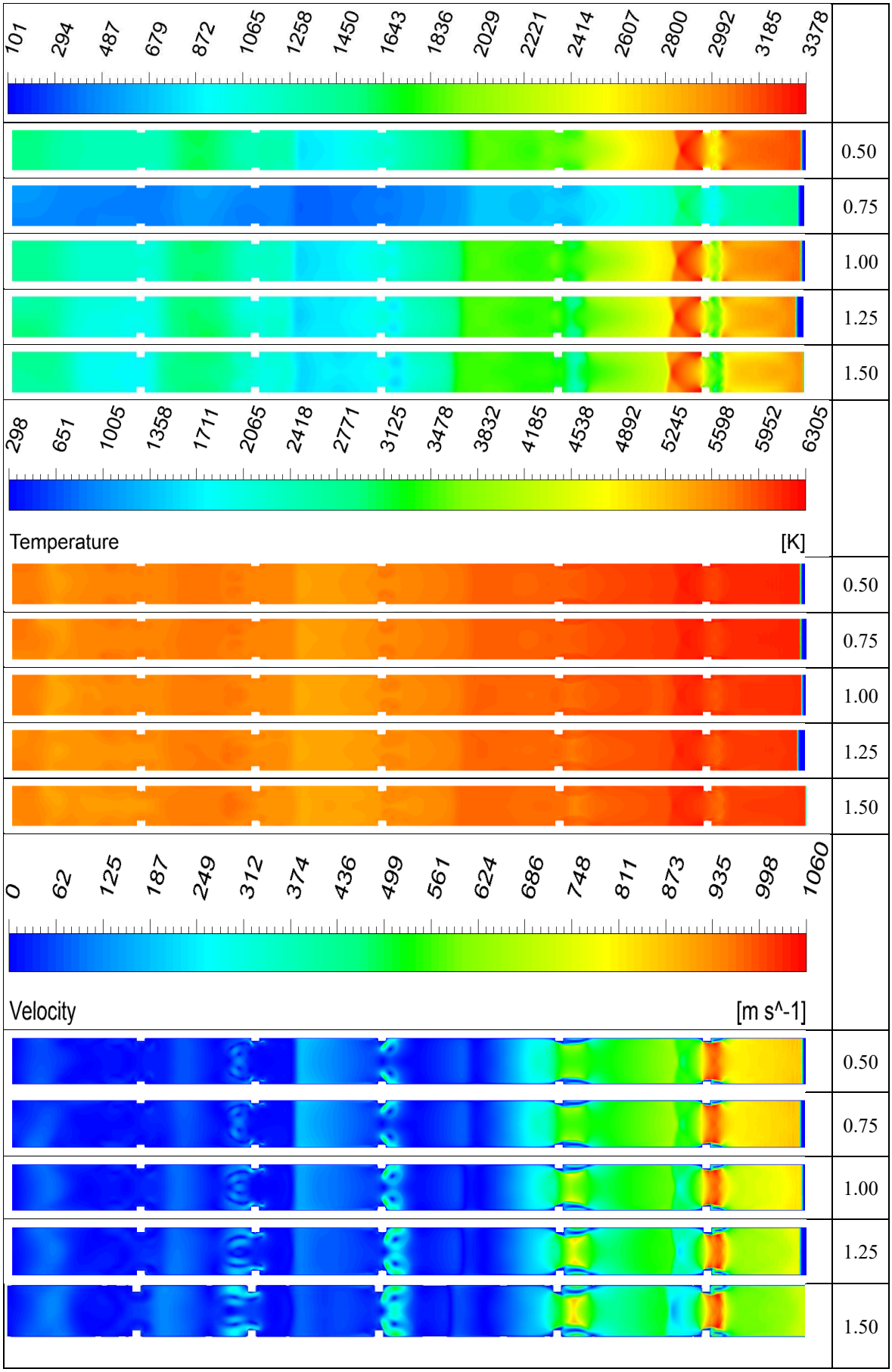

Table 4.4. Acetylene-Equivalence 1: Pressure, Temperature and, Velocity Contours Start

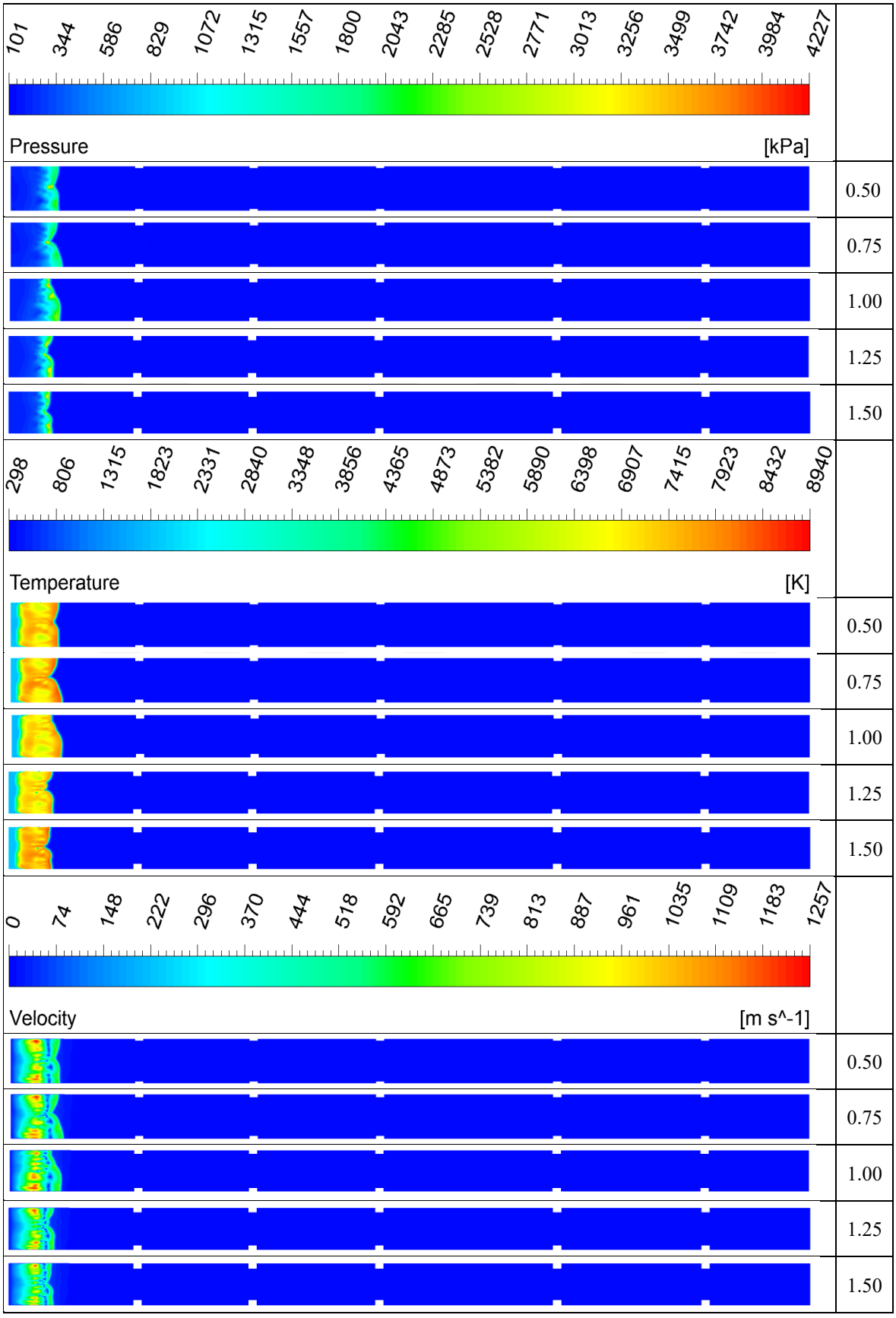

Table 4.5. Acetylene-Equivalence 1: Pressure, Temperature, and Velocity Contours Exit

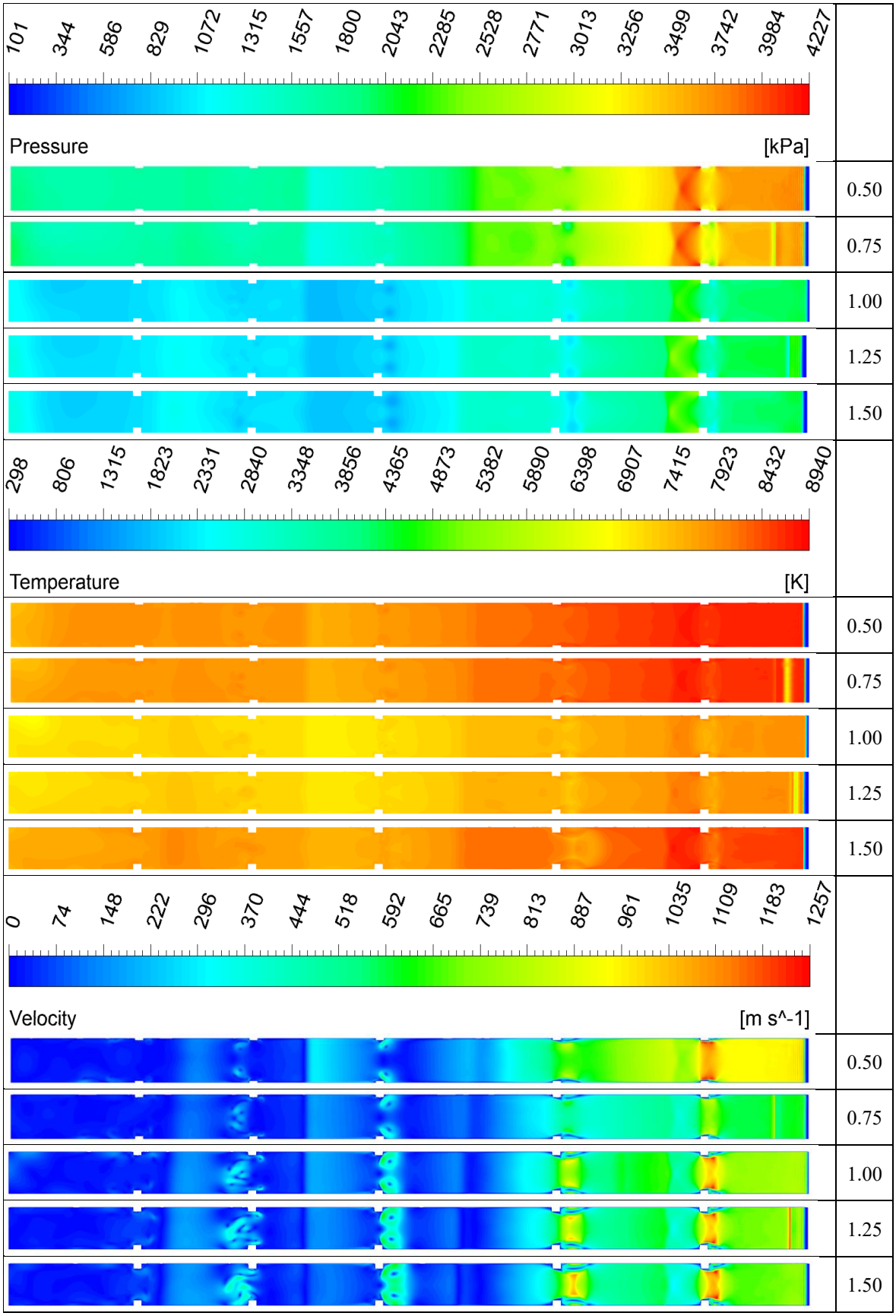

Table 4.6. Acetylene-Equivalence 1.5: Pressure, Temperature and Velocity Contours Start

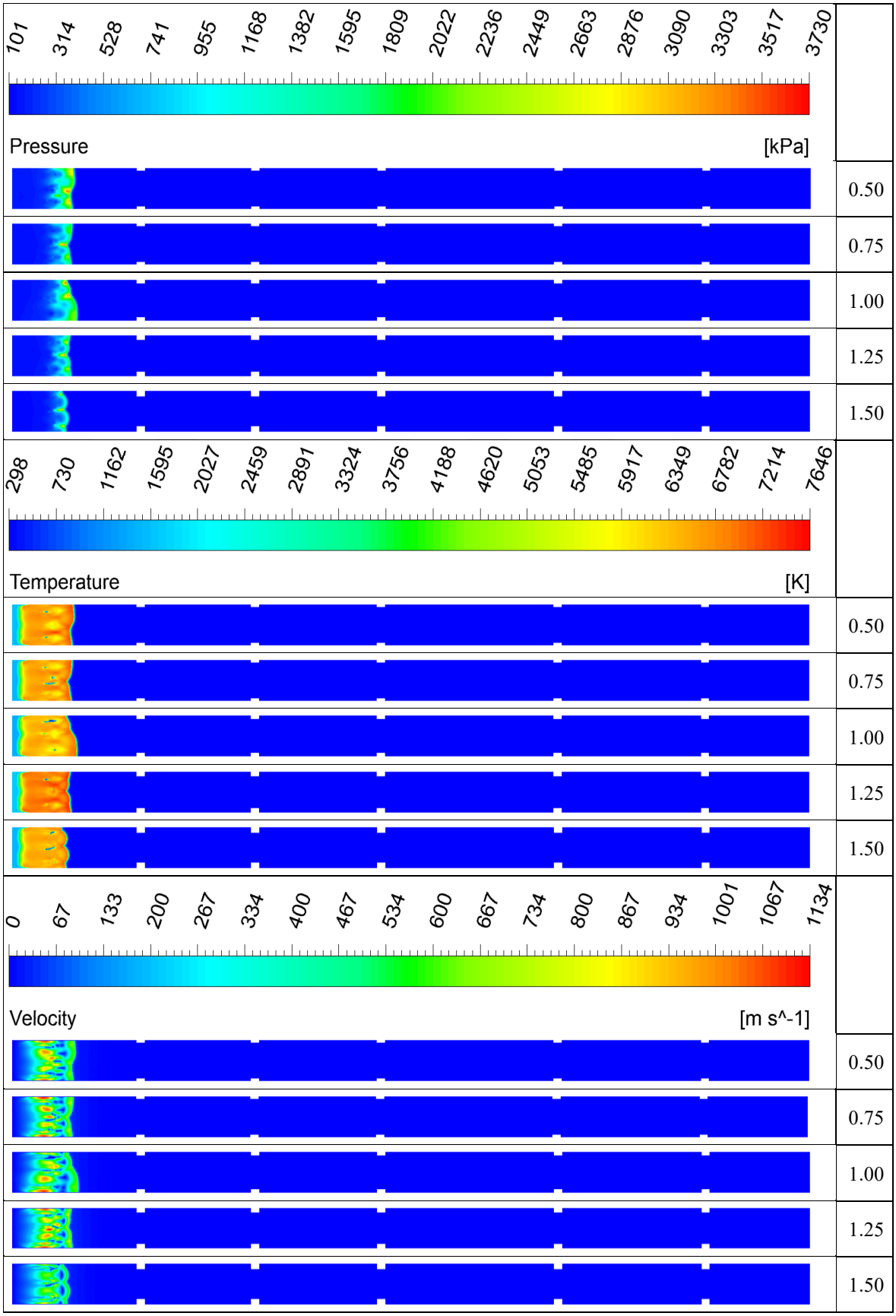

Table 4.7. Acetylene-Equivalence 1.5: Pressure, Temperature, and Velocity Contours Exit

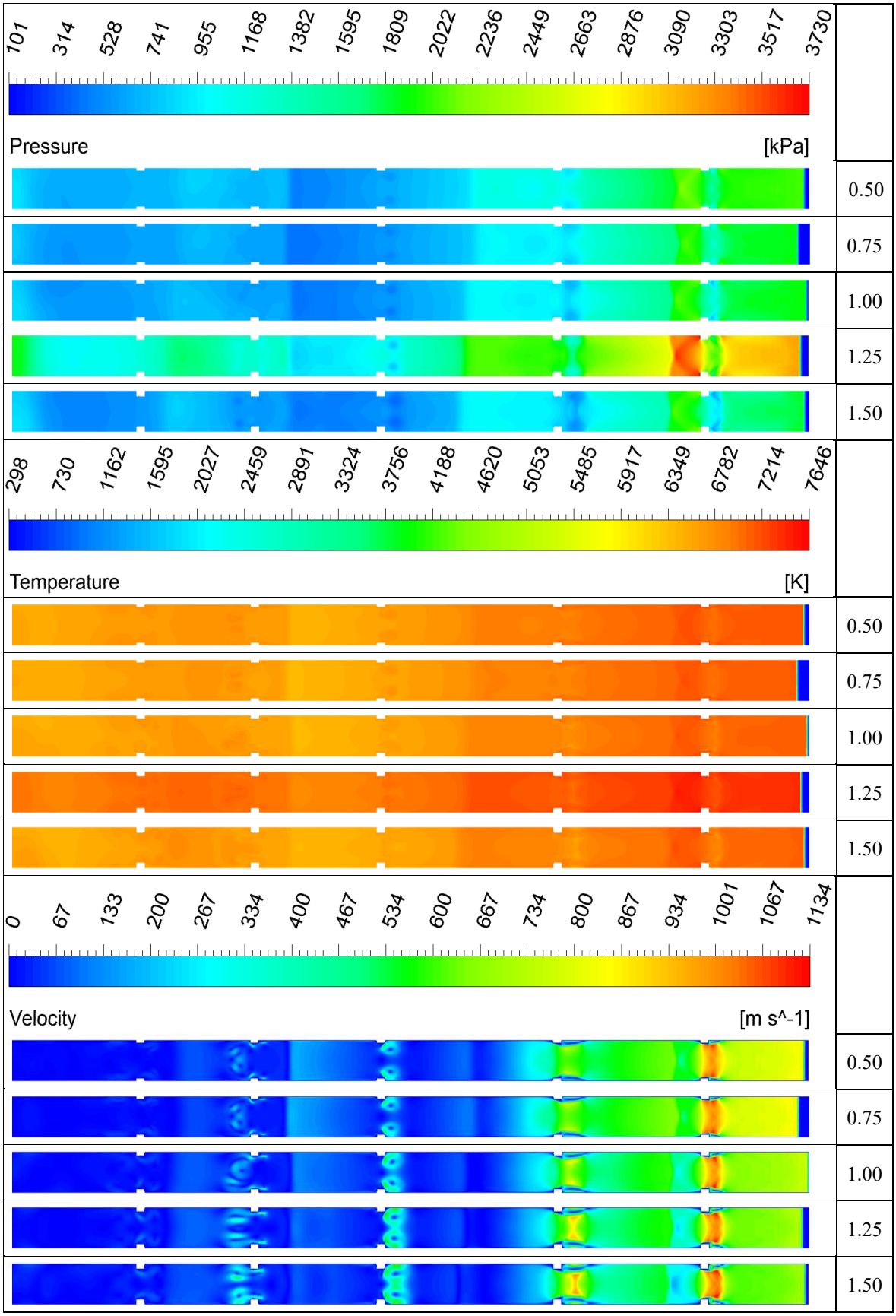

4.2. Ethylene

Upon analyzing the results for Ethylene-Oxygen at an equivalence ratio of 0.5, we observed micro-explosions in all analyses, as illustrated in Figure 4.19. These micro-explosions cause localized spikes in pressure, temperature, and velocity along the tube.

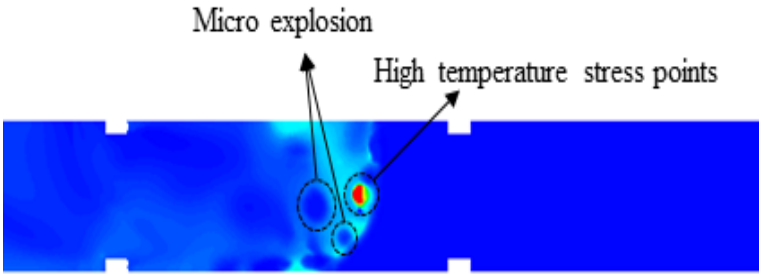

Figure 4.19. Micro Explosion Occurring at Equivalence 0.5

Upon examining the data for equivalence ratios 1 and 1.5, we observed that the shock wave formation times averaged 0.34 and 0.55 milliseconds, respectively. In both cases, the equivalence ratios exit the tube 0.61 milliseconds after the shock wave formation. At an equivalence ratio of 1, we observe a maximum pressure of 4541.13 kPa and a temperature of 7464.19 K at an obstacle height of 0.5 mm. Additionally, the velocity of 1261.08 m/s is recorded at an obstacle height of 1 mm. At an equivalence ratio of 1.5, examinations reveal the following maximum values: pressure at 4069.46 kPa, temperature at 6065.35 K, and velocity at 1233.97 m/s. These peaks occur at obstacle heights of 0.5 mm, 0.75 mm, and 1.5 mm, respectively. It can be observed that the maximum pressure, temperature, and velocity values occur at stoichiometric conditions in Table 4.8. Lower equivalence ratios lead to lower temperatures and pressures. Additionally, changes in obstacle heights do not cause significant differences in pressure, temperature, and velocity values.

It is determined from Table 4.9 that the shock wave occurs at the entrance of the first obstacle, while Table 4.11 shows that the shock wave occurs between the first and second obstacles. The graphs for the equivalence ratios of 1 are presented in Figure 4.20, Figure 4.21, and Figure 4.23, respectively. These figures represent the time elapsed until shock wave formation. The figures 4.24, 4.25, and 4.26 presented illustrate the changes caused by the shock wave as it progresses through the tube towards the exit.

Contours for equivalence ratios 1 and 1.5 are presented in Table 4.9, Table 4.10, Table 4.11, and Table 4.12.

Table 4.8. Pressure, Temperature, and Velocity Values for Ethylene-Oxygen

Geometric Features		Molar Mass		Ethylene [1]		
A	b	$[C_2H_4]$	0.226	P[kPa]	T[K]	V[m/s]
0.5	2.18	$[O_2]$	0.774	4541.13	7464.19	1254.71
0.75	2.18			4536.87	7459.94	1260.88
1	2.18			4526.31	7453.78	1261.08
1.25	2.18			4524.82	7451.26	1260.56
1.5	2.18			4509.22	7451.10	1257.32
Geometric Features		Molar Mass		Ethylene [1.5]		
A	b	$[C_2H_4]$	0.303	P[kPa]	T[K]	V[m/s]
0.5	2.18	$[O_2]$	0.697	4069.46	6059.88	1228.94
0.75	2.18			4064.54	6065.35	1231.10
1	2.18			3615.88	5694.91	1166.52
1.25	2.18			4051.83	6061.64	1231.12
1.5	2.18			4061.32	6059.22	1233.97

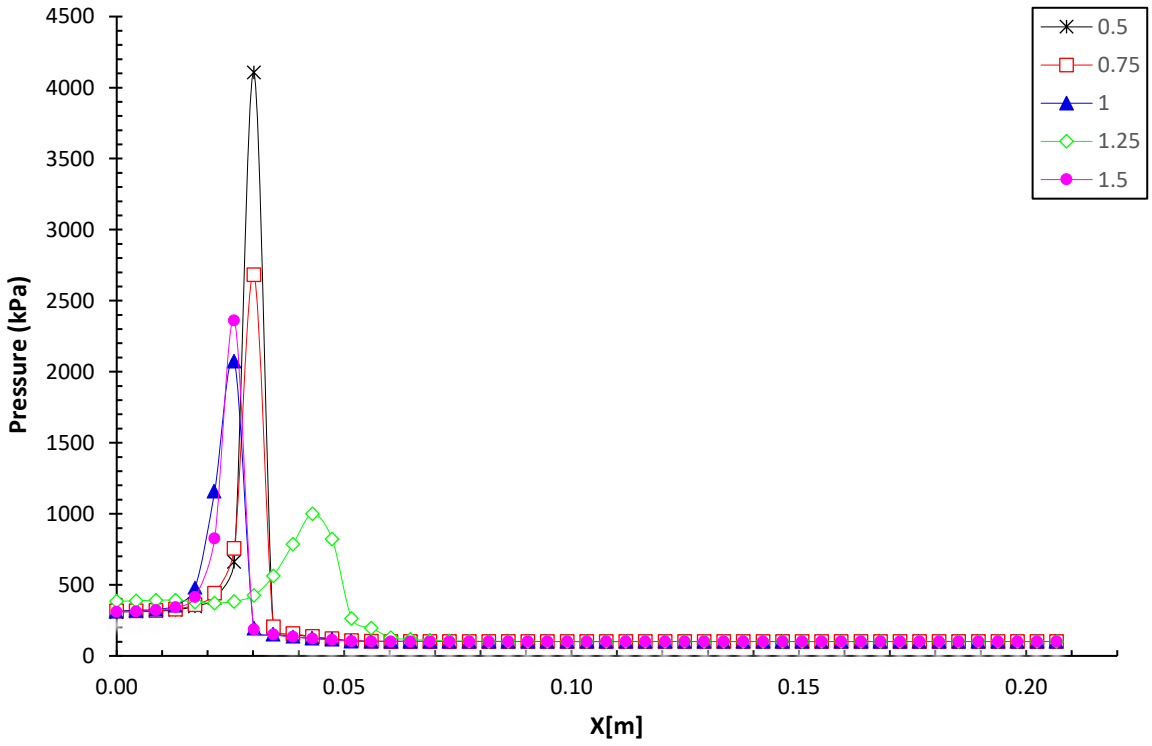

Figure 4.20. Ethylene-Oxygen Pressure Equivalence 1 Shockwave Starting Point

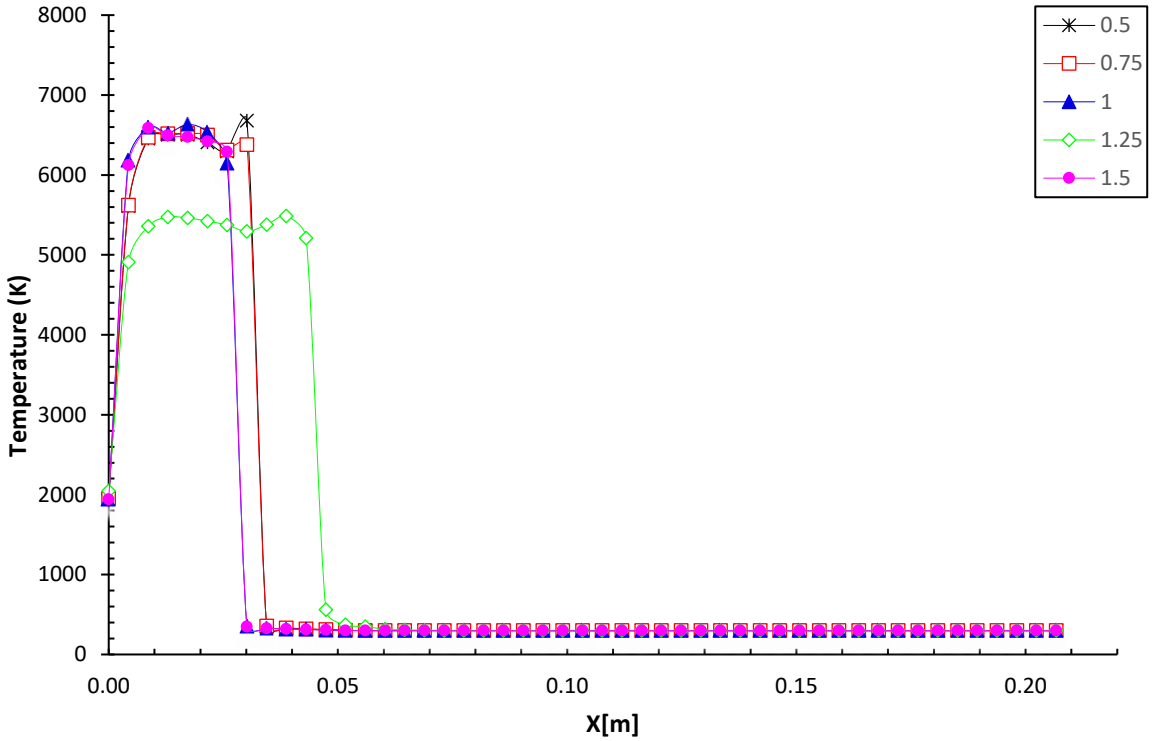

Figure 4.21. Ethylene-Oxygen Temperature Equivalence 1 Shockwave Starting Point

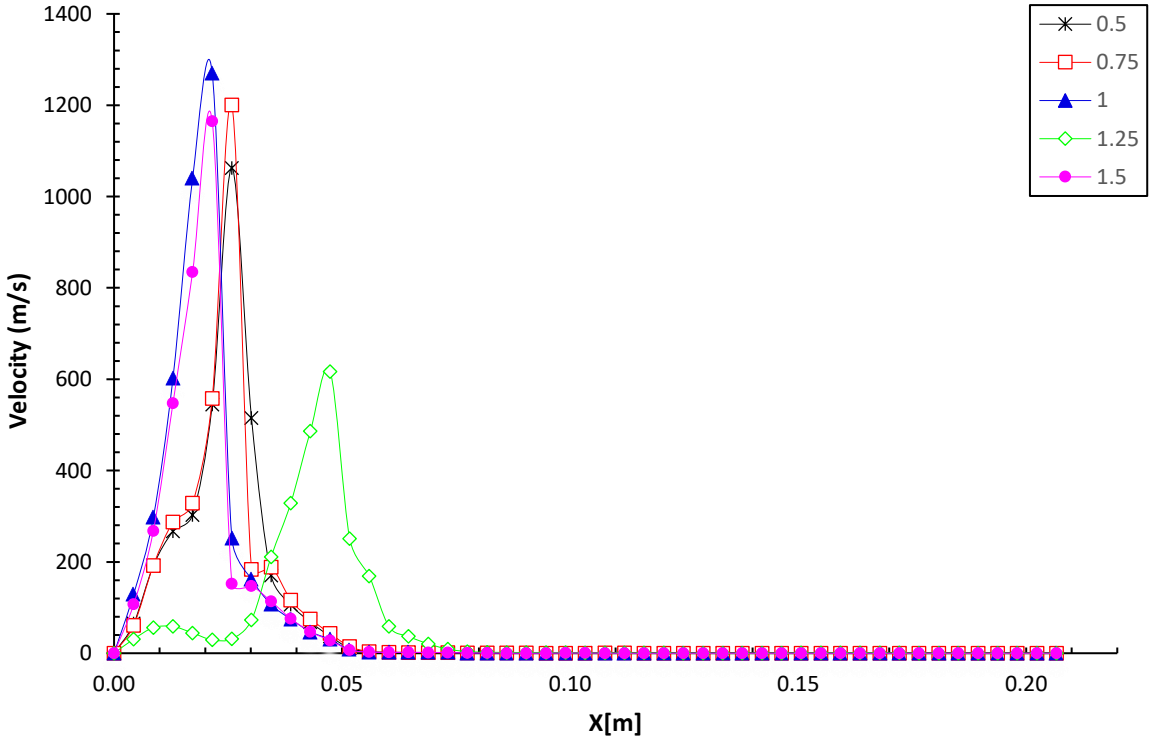

Figure 4.22. Ethylene-Oxygen Velocity Equivalence 1 Shockwave Starting Point

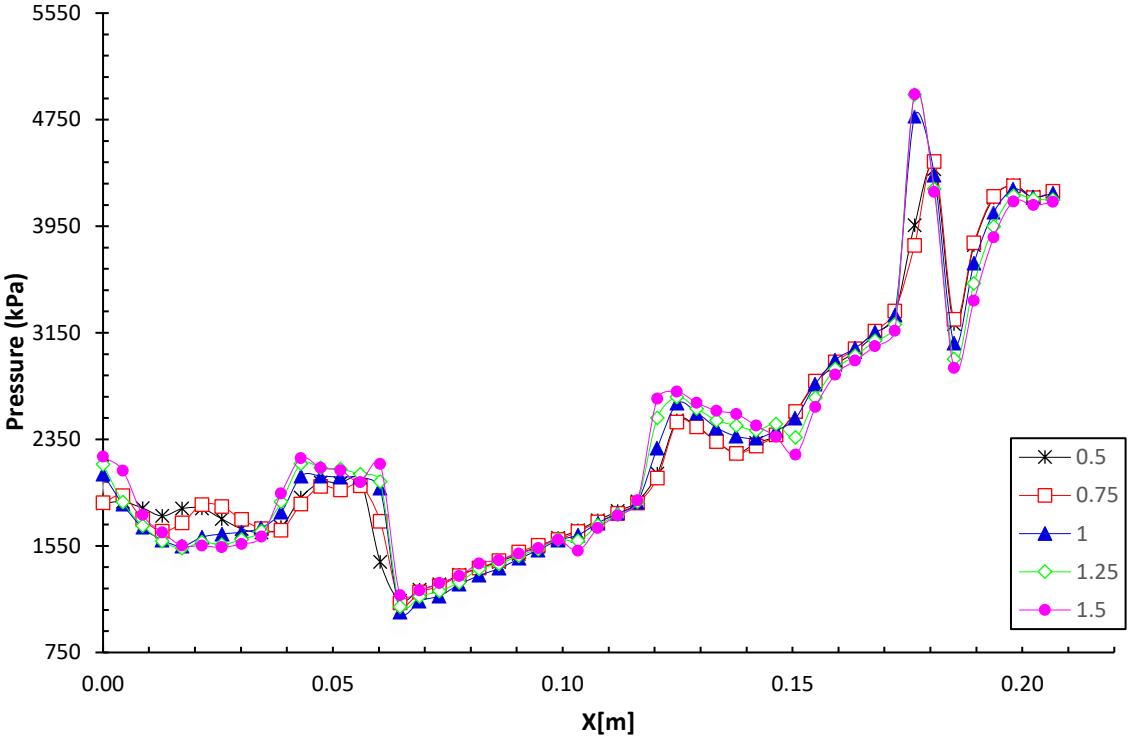

Figure 4.23. Ethylene-Oxygen Pressure Equivalence 1 Shockwave at the Exit of Tube

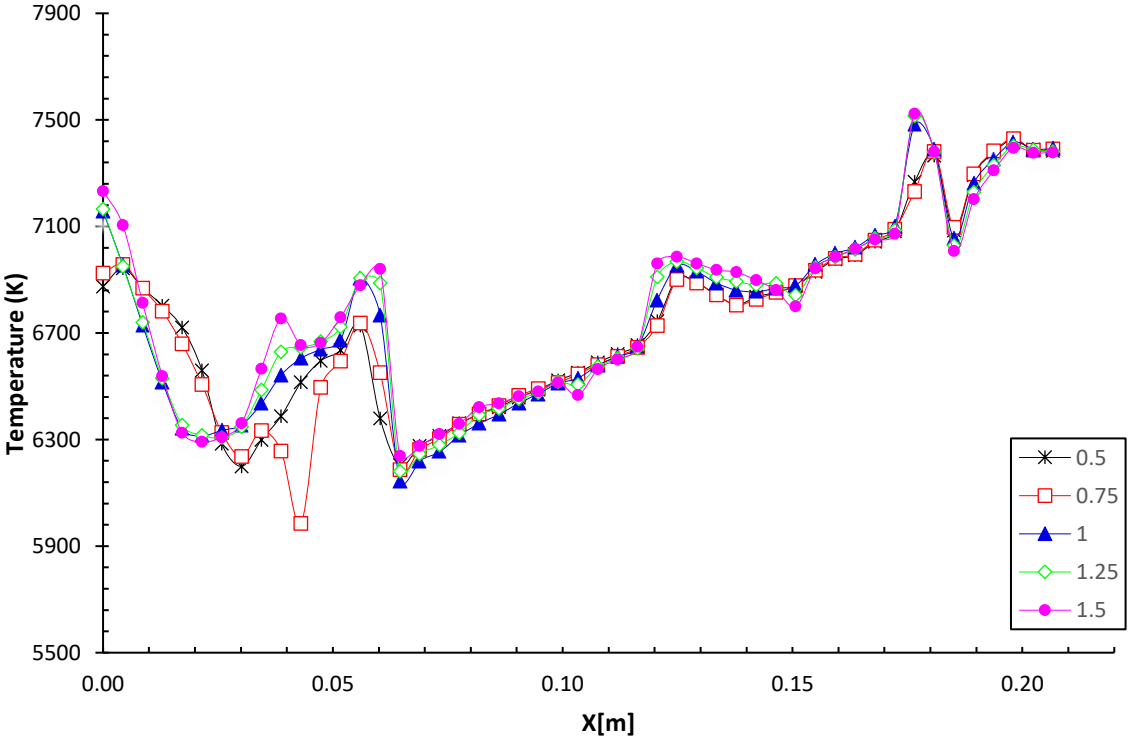

Figure 4.24. Ethylene-Oxygen Temperature Equivalence 1 Shockwave at the Exit of Tube

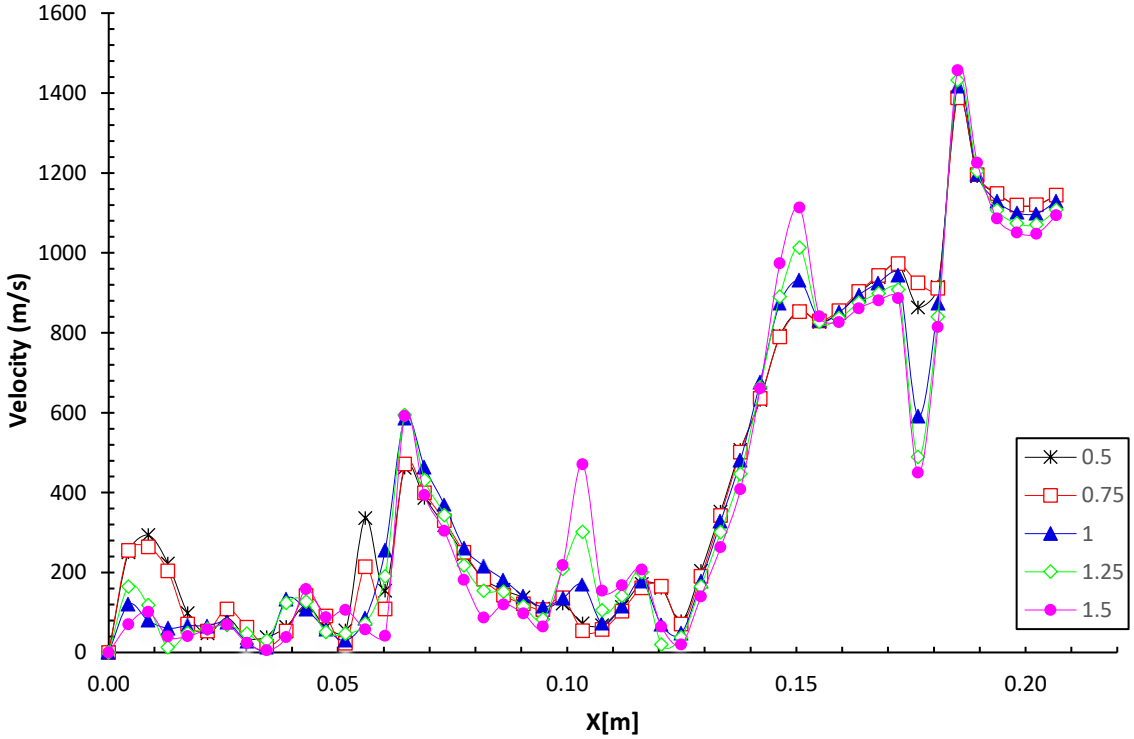

Figure 4.25. Ethylene-Oxygen Velocity Equivalence 1 Shockwave at the Exit of Tube

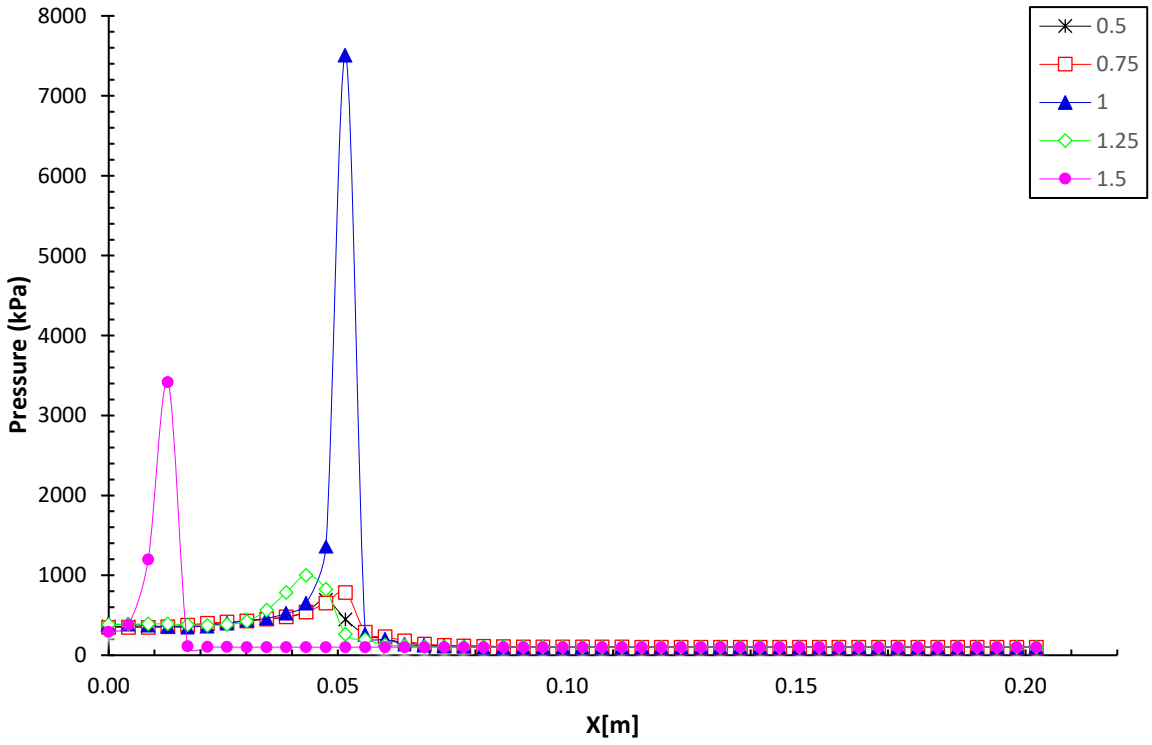

Figure 4.26. Ethylene-Oxygen Pressure Equivalence 1.5 Shockwave Starting Point

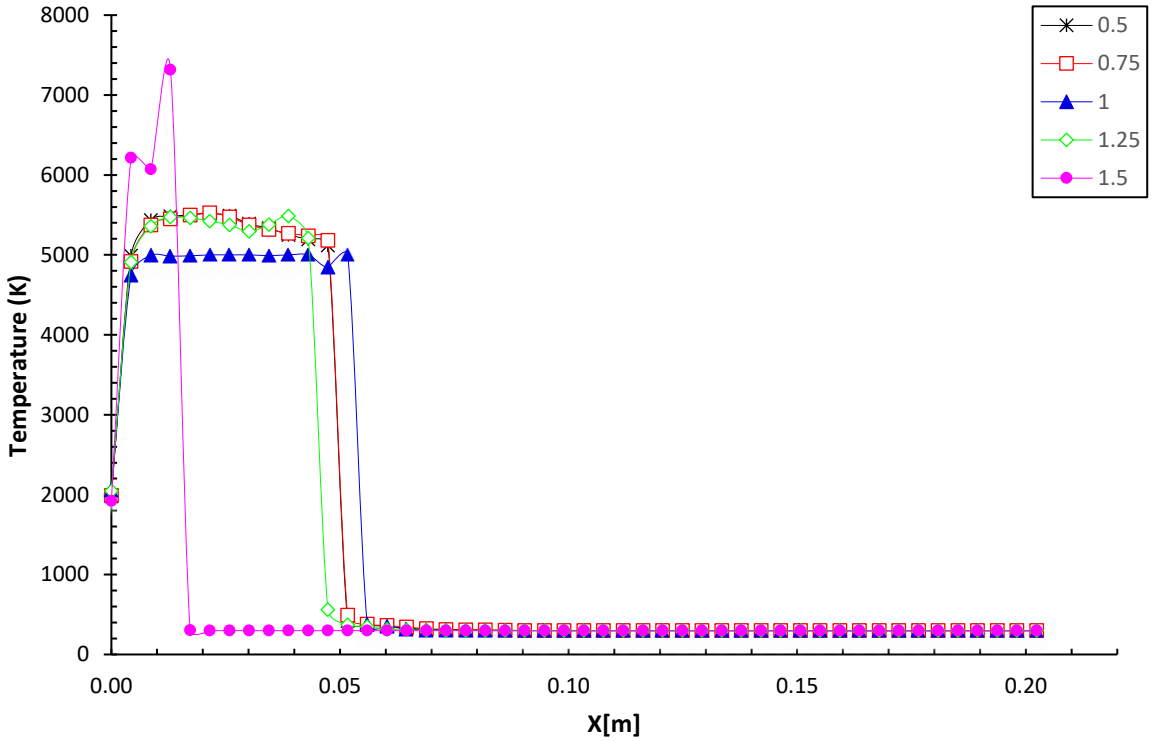

Figure 4.27. Ethylene-Oxygen Temperature Equivalence 1.5 Shockwave Starting Point

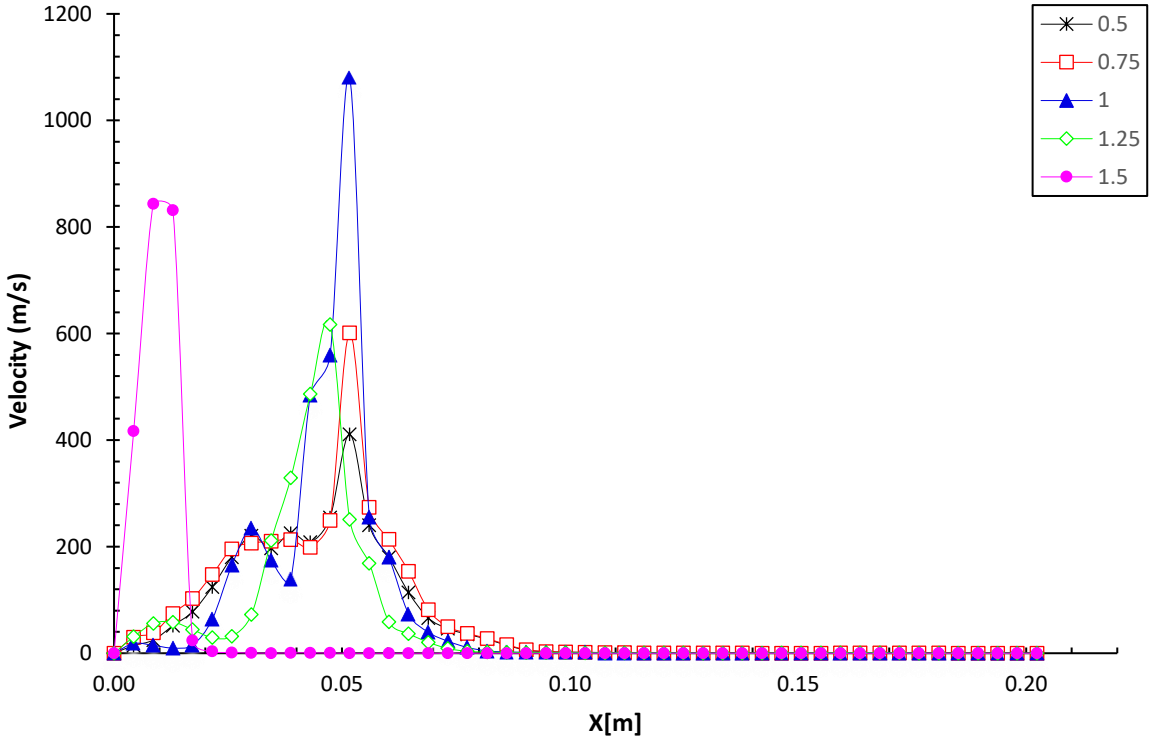

Figure 4.28. Ethylene-Oxygen Velocity Equivalence 1.5 Shockwave Starting Point

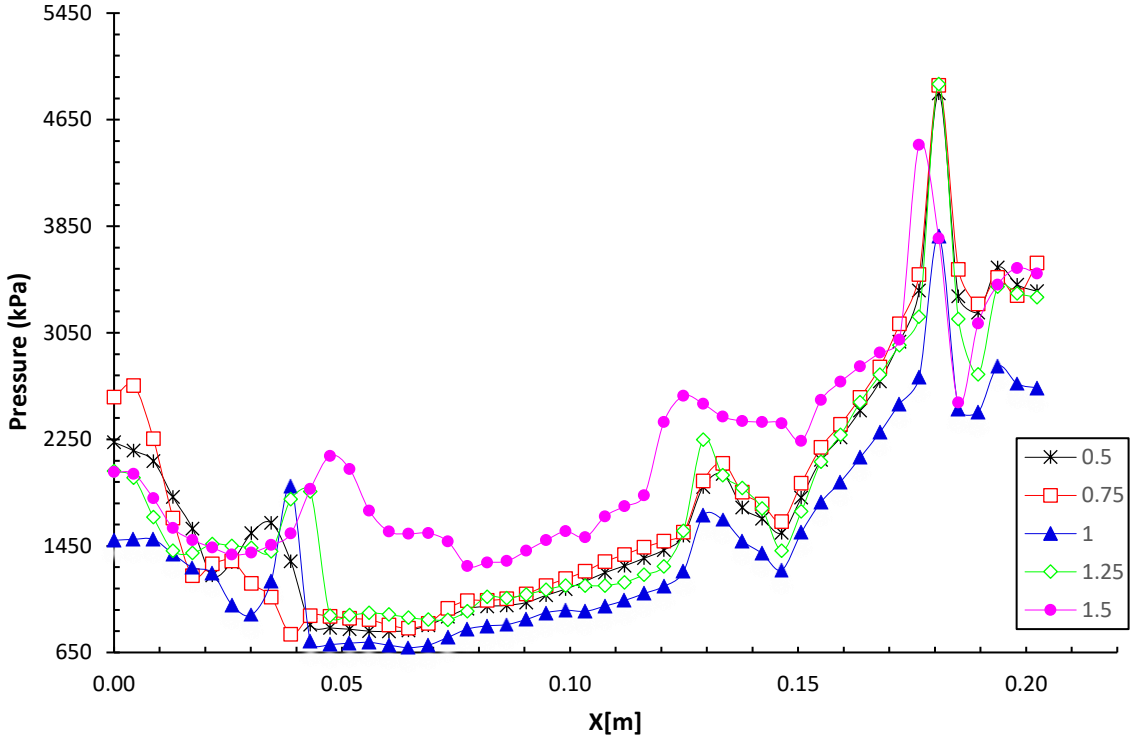

Figure 4.29. Ethylene-Oxygen Pressure Equivalence 1.5 Shockwave at the Exit of Tube

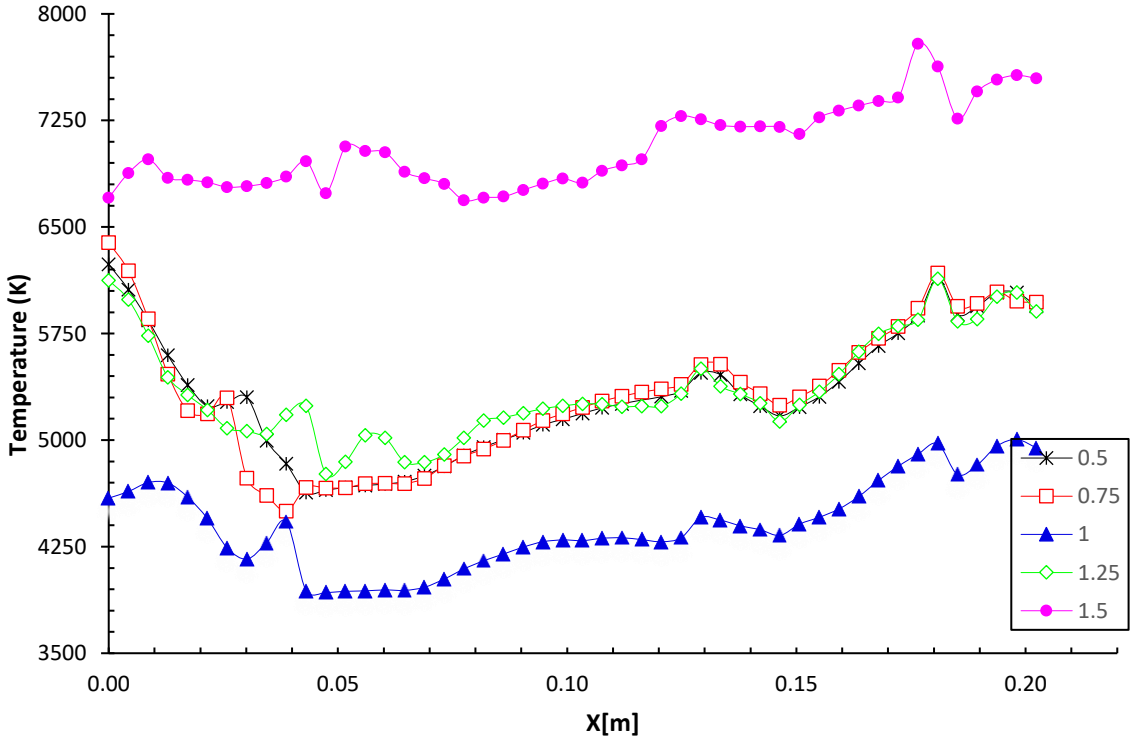

Figure 4.30. Ethylene-Oxygen Temperature Equivalence 1.5 Shockwave at the Exit of Tube

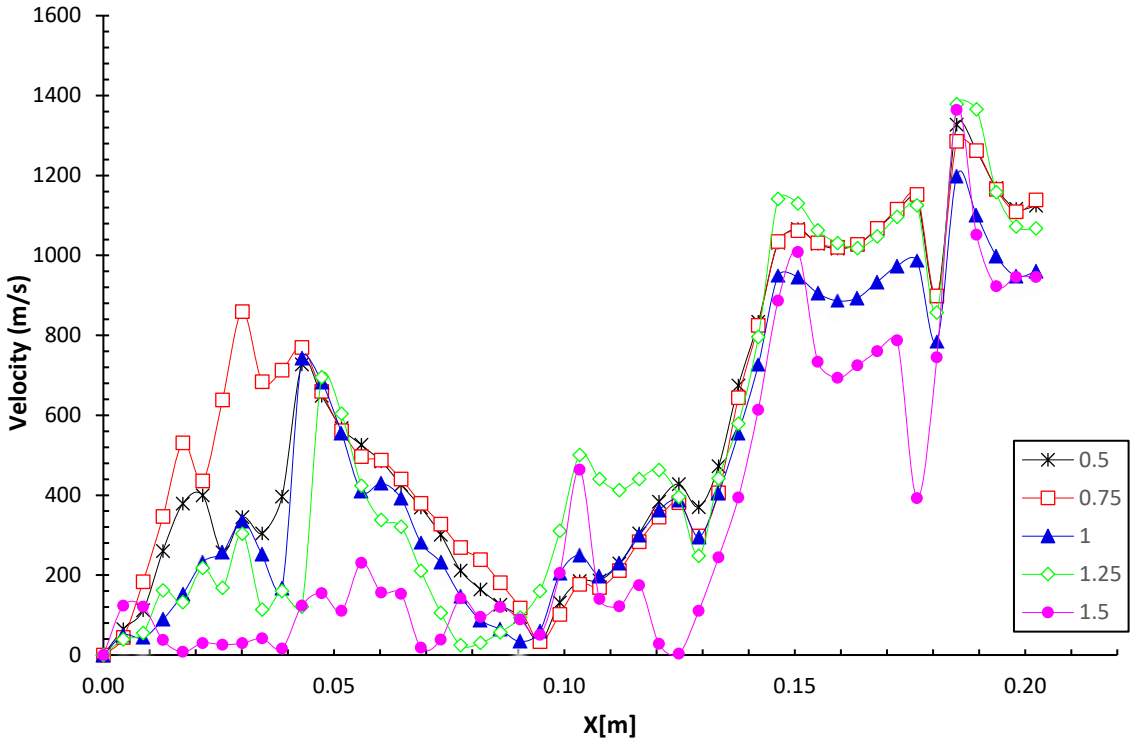

Figure 4.31. Ethylene-Oxygen Velocity Equivalence 1.5 Shockwave at the Exit of Tube

Table 4.9. Ethylene-Equivalence 1: Pressure, Temperature, and Velocity Contours Start

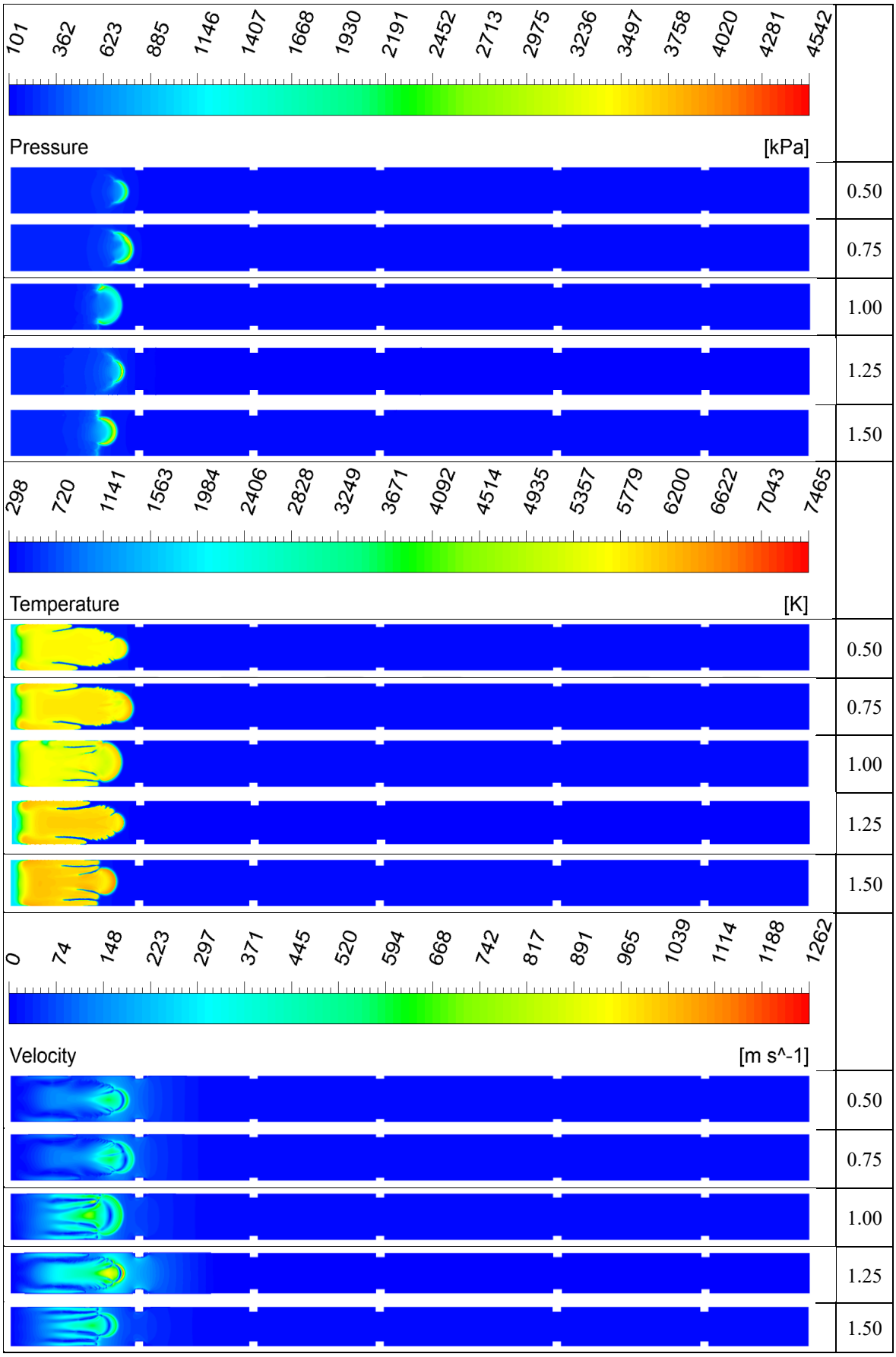

Table 4.10. Ethylene-Equivalence 1: Pressure, Temperature, and Velocity Contours Exit

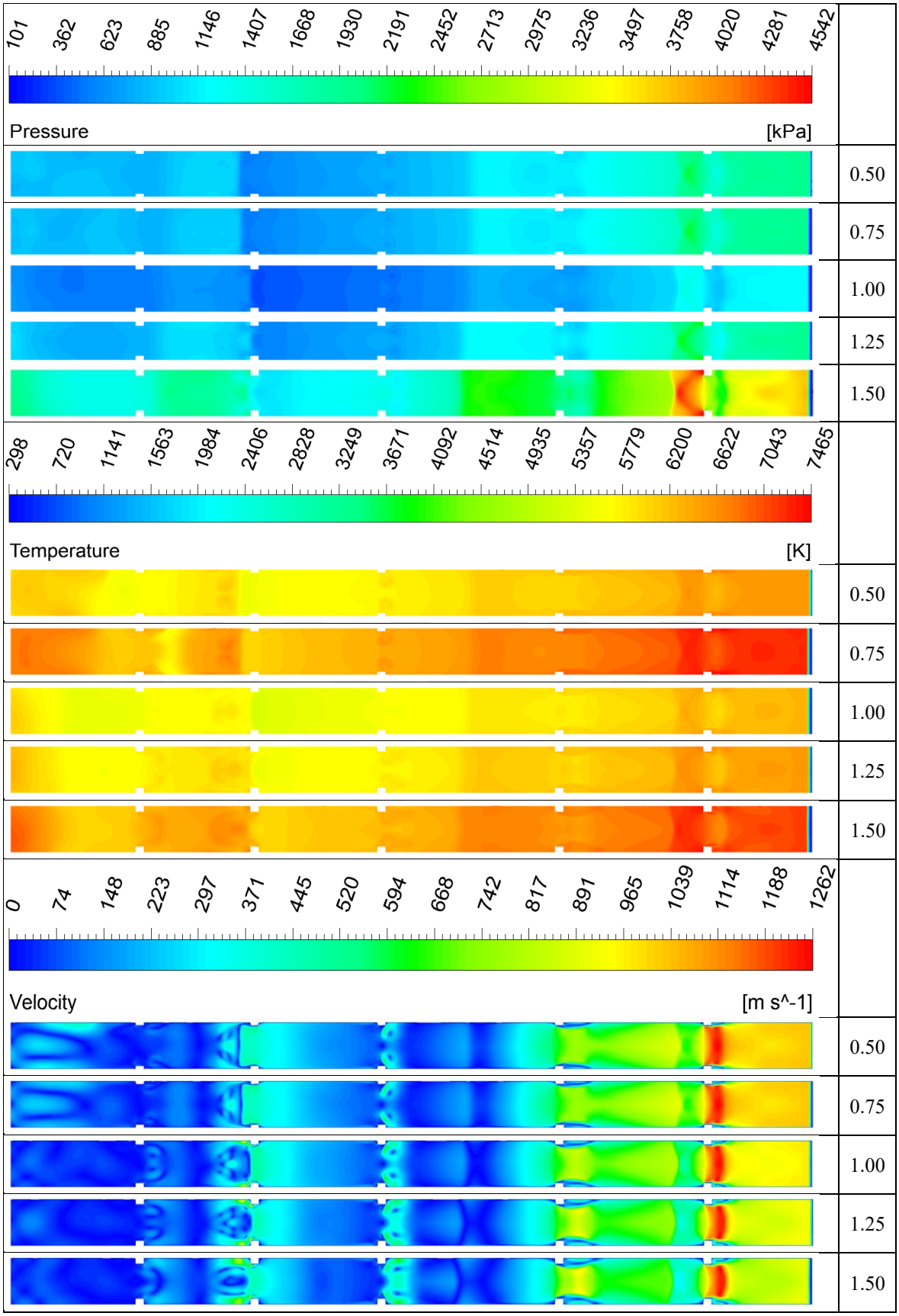

Table 4.11. Ethylene-Equivalence 1.5: Pressure, Temperature, and Velocity Contours Start

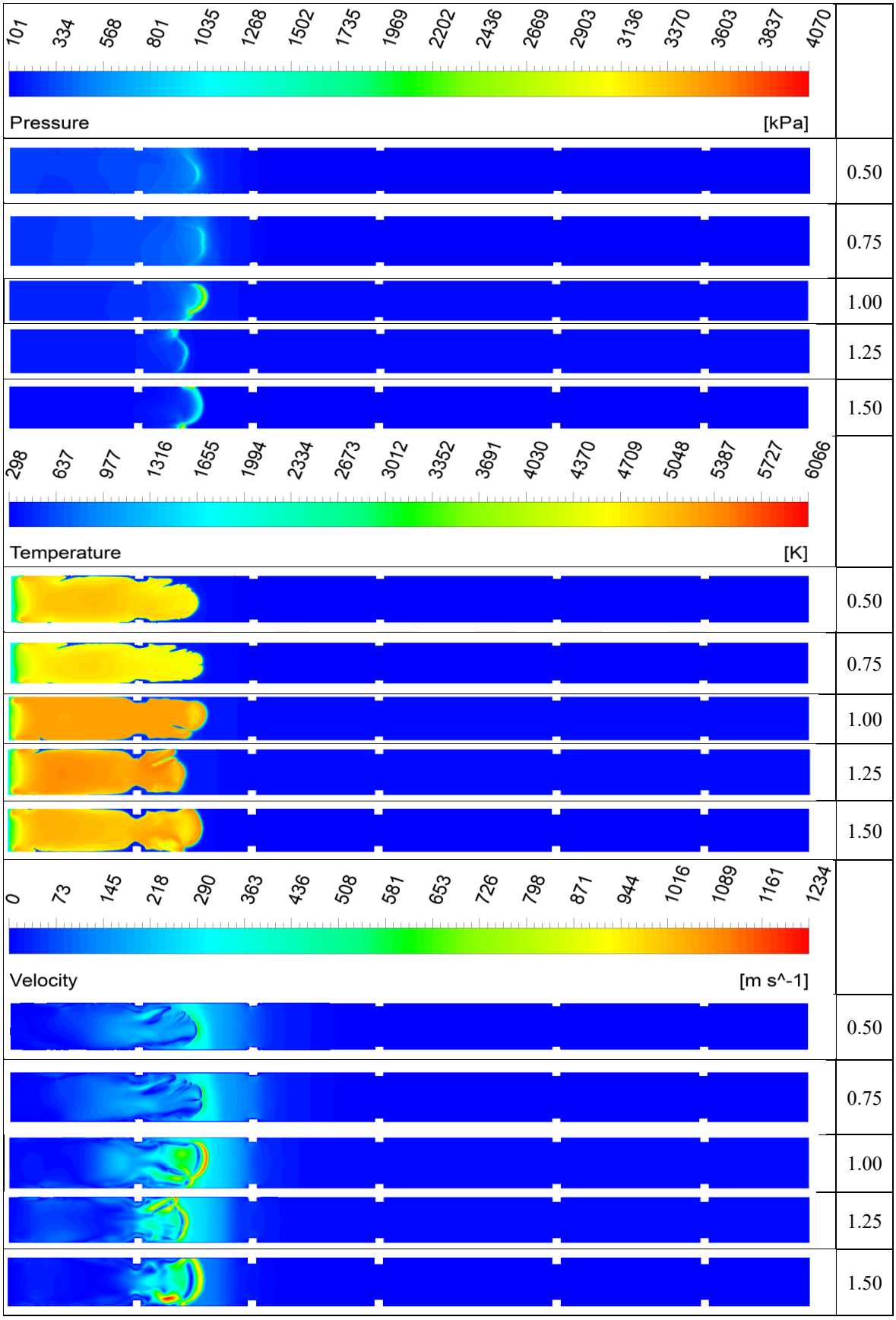

Table 4.12. Ethylene-Equivalence 1.5: Pressure, Temperature, and Velocity Contours Exit

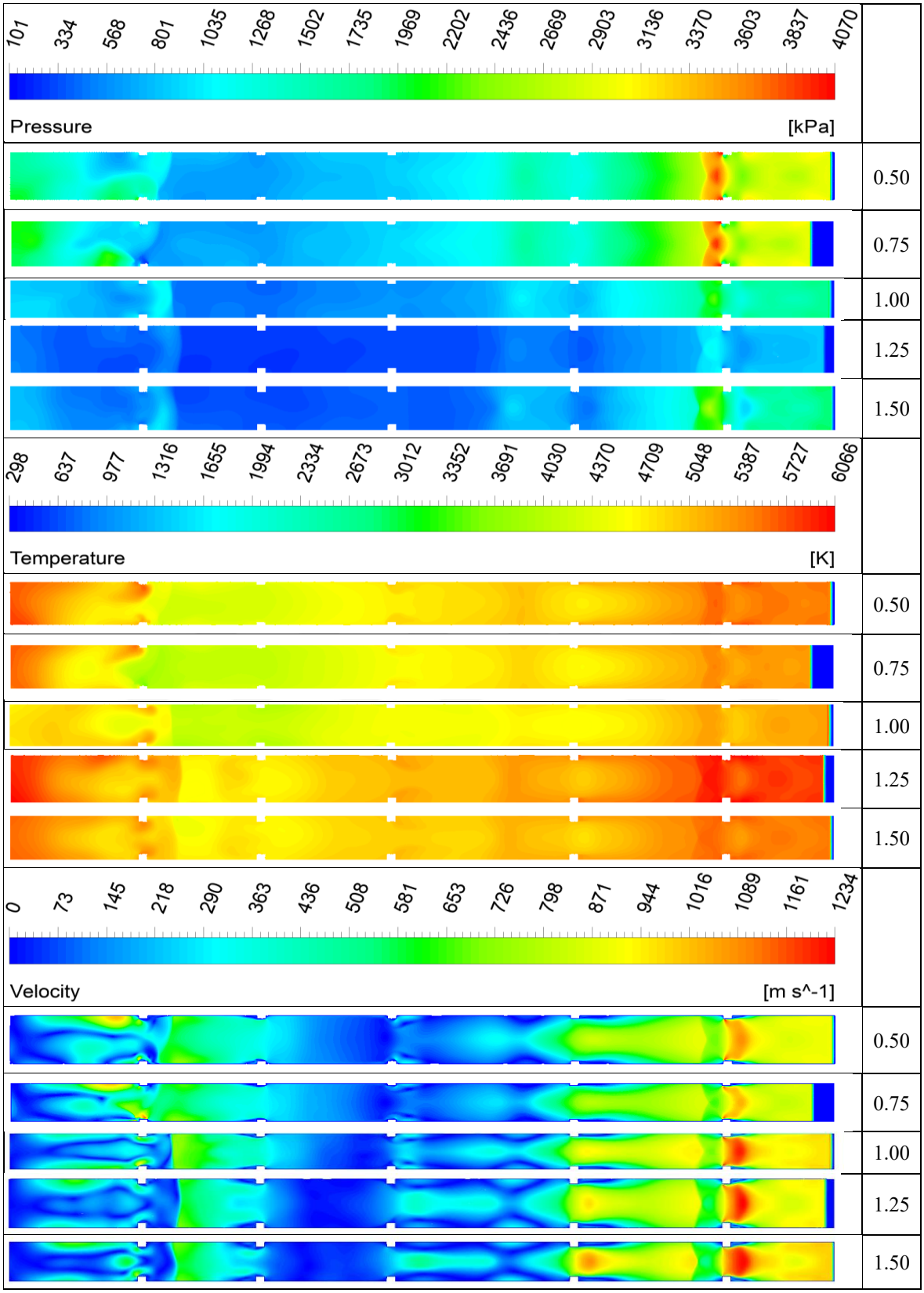

4.3. Ethane

Figure 4.1 illustrates the CFD findings for the ethane-oxygen system at all blockage ratios for the equivalency ratio of 0.5, which exhibit micro-explosions and high-stress areas. These micro-explosions can lead to vibration loads and jeopardize the design, making it undesirable. On the other hand, for the equivalence ratio of 1.5, it was determined that the temperature assigned as the patch gradually decreases over time and reaches ambient conditions, and no shock wave formation occurs. In Ethane fuel, the shock wave is observed to form on average in 0.66 milliseconds, and it completely leaves the PDE in 0.057 milliseconds after the shock wave formation. The maximum pressure value of the shock wave at stoichiometric conditions is 6699.67 kPa, the temperature value is 4934.78 K, and the velocity value is 1344.36 m/s, as seen in Table 4.13. The shock wave reaches these maximum values at an obstacle height of 0.75 mm.

Looking at the contour curves in Table 4.14, it is determined that the shock wave forms immediately after the first obstacle.

Table 4.13. Pressure, Temperature, and Velocity Values for Ethane-Oxygen

Geometric Features		Molar Mass		Ethane [1]		
a	b	$[C_2H_6]$	0.211	P[kPa]	T[K]	V[m/s]
0.5	2.18	$[O_2]$	0.789	4934.15	6699.28	1342.15
0.75	2.18			4934.78	6699.67	1344.36
1	2.18			4929.81	6698.90	1338.07
1.25	2.18			4921.84	6695.88	1341.11
1.5	2.18			4925.19	6695.30	1343.77

The curves for the equivalence ratios of 1 are presented in Figure 4.32, Figure 4.33, and Figure 4.34, respectively. These figures represent the time elapsed until shock wave formed. Figures 4.35, 4.36, and 4.37 illustrate the changes caused by the shock wave as it progresses through the tube towards the exit. Table 4.14 illustrates the shock wave formation process of ethane fuel, while Table 4.15 demonstrates how high-pressure and high-temperature gas behaves throughout the PDE.

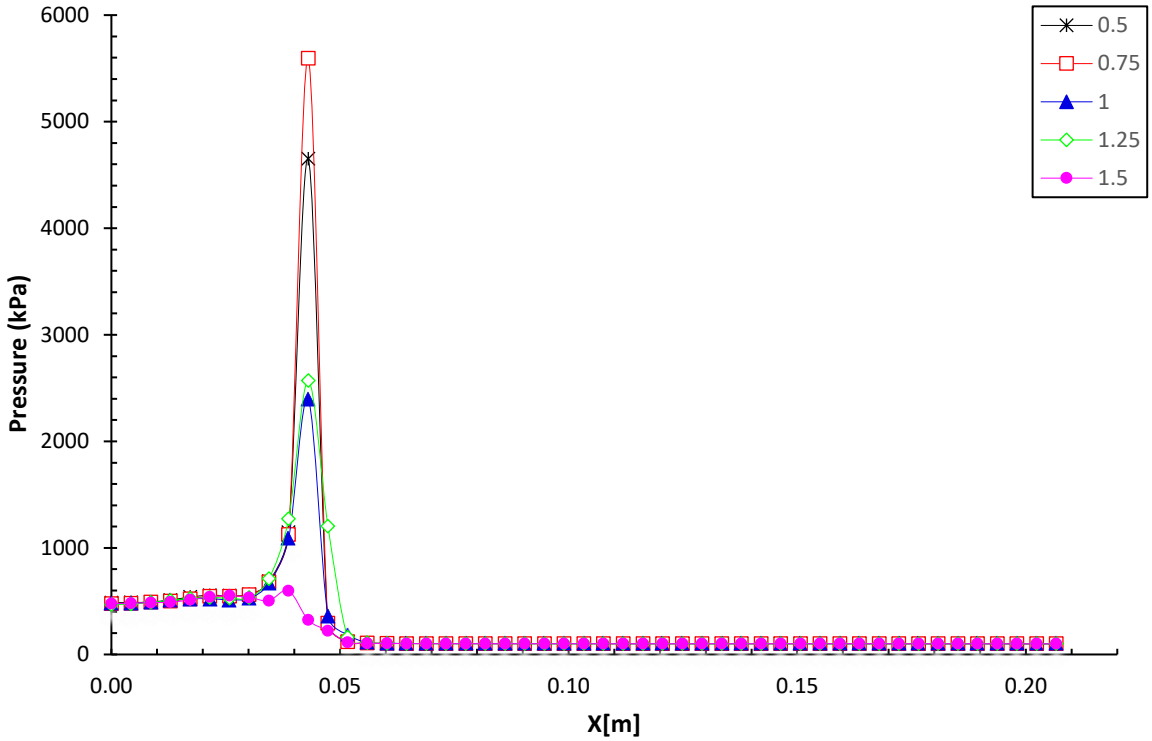

Figure 4.32. Ethane-Oxygen Pressure Equivalence 1 Shockwave Starting Point

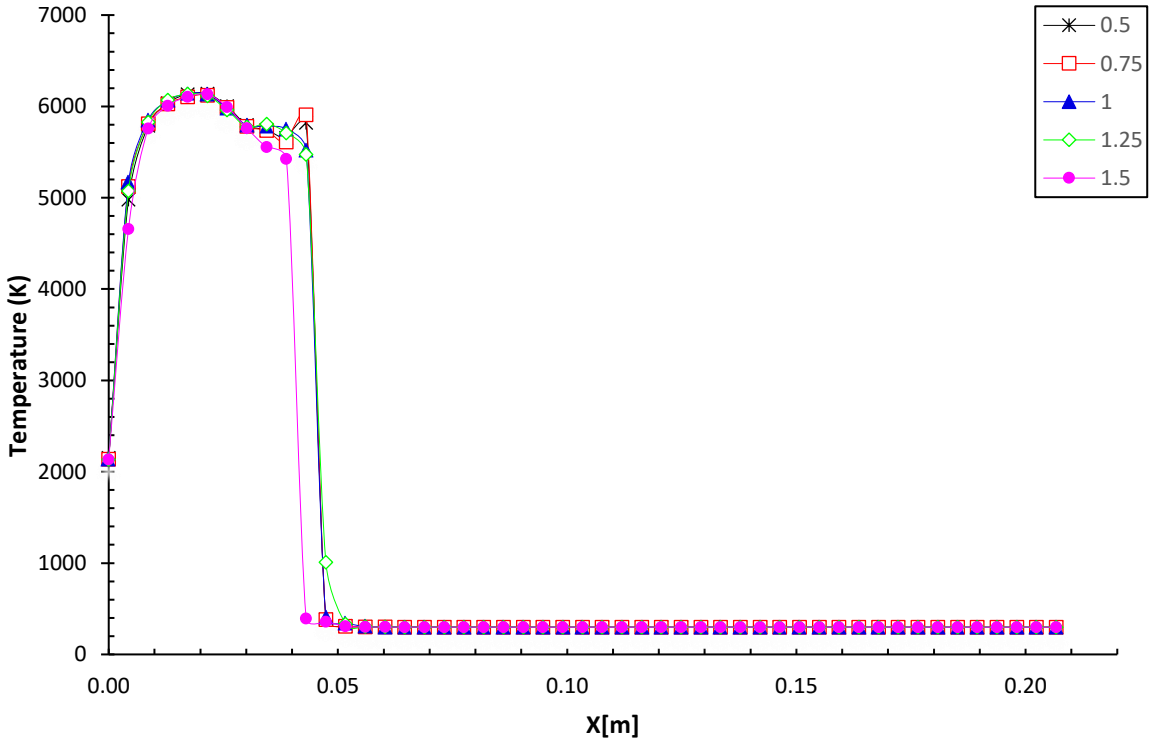

Figure 4.33. Ethane-Oxygen Temperature Equivalence 1 Shockwave Starting Point

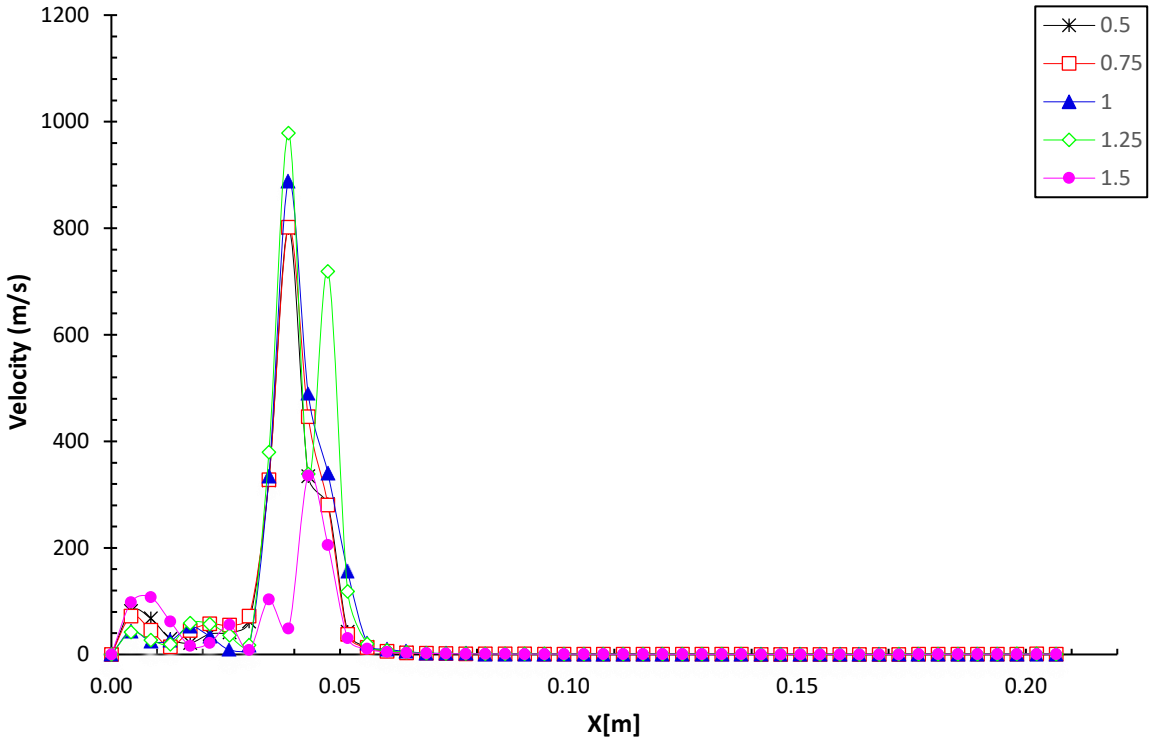

Figure 4.34. Ethane-Oxygen Velocity Equivalence 1 Shockwave Starting Point

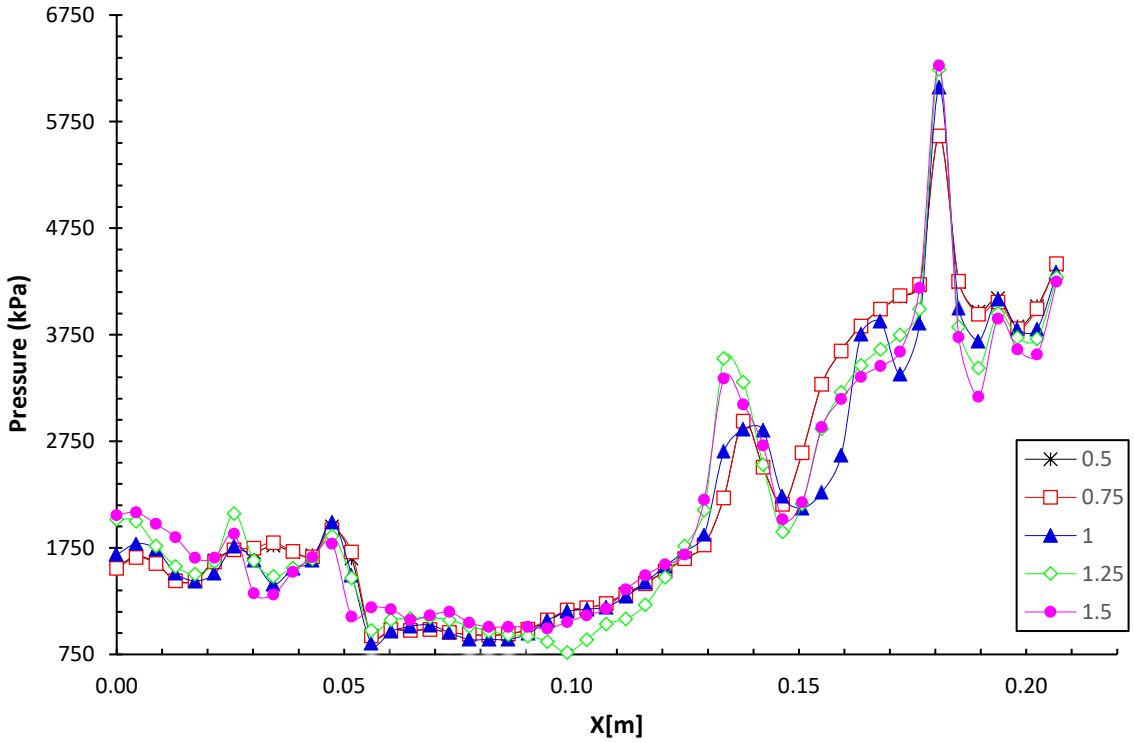

Figure 4.35. Ethane-Oxygen Pressure Equivalence 1 Shockwave at the Exit of Tube

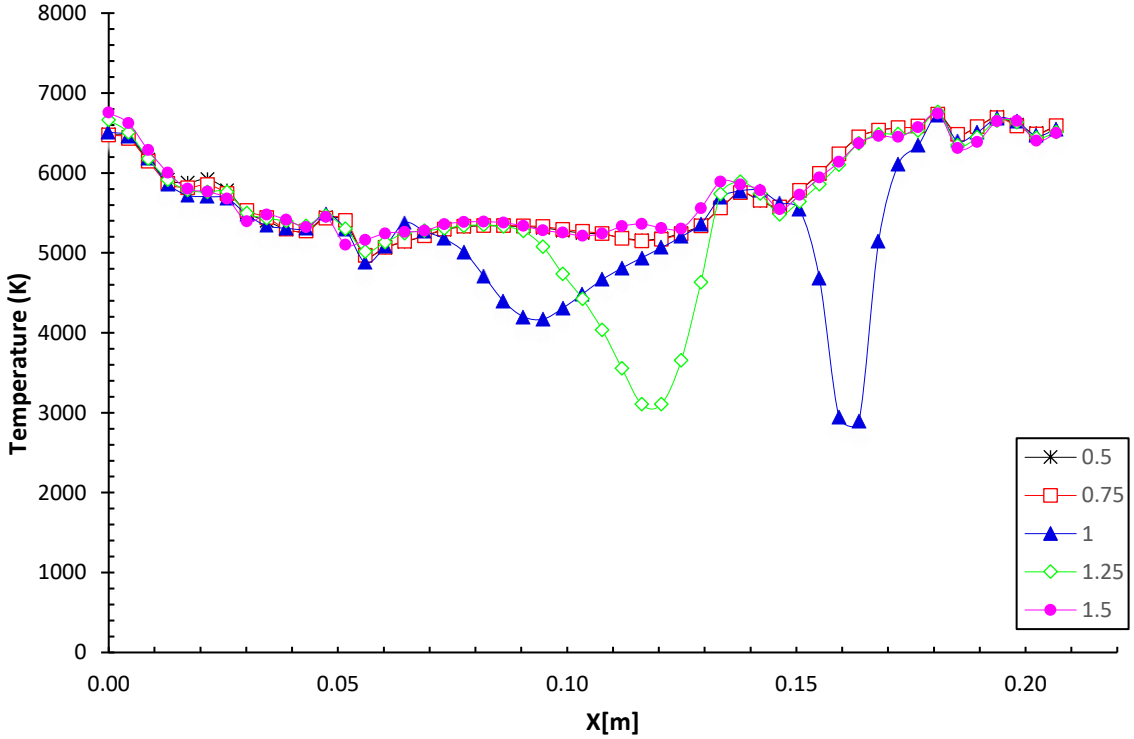

Figure 4.36. Ethane-Oxygen Temperature Equivalence 1 Shockwave at the Exit of Tube

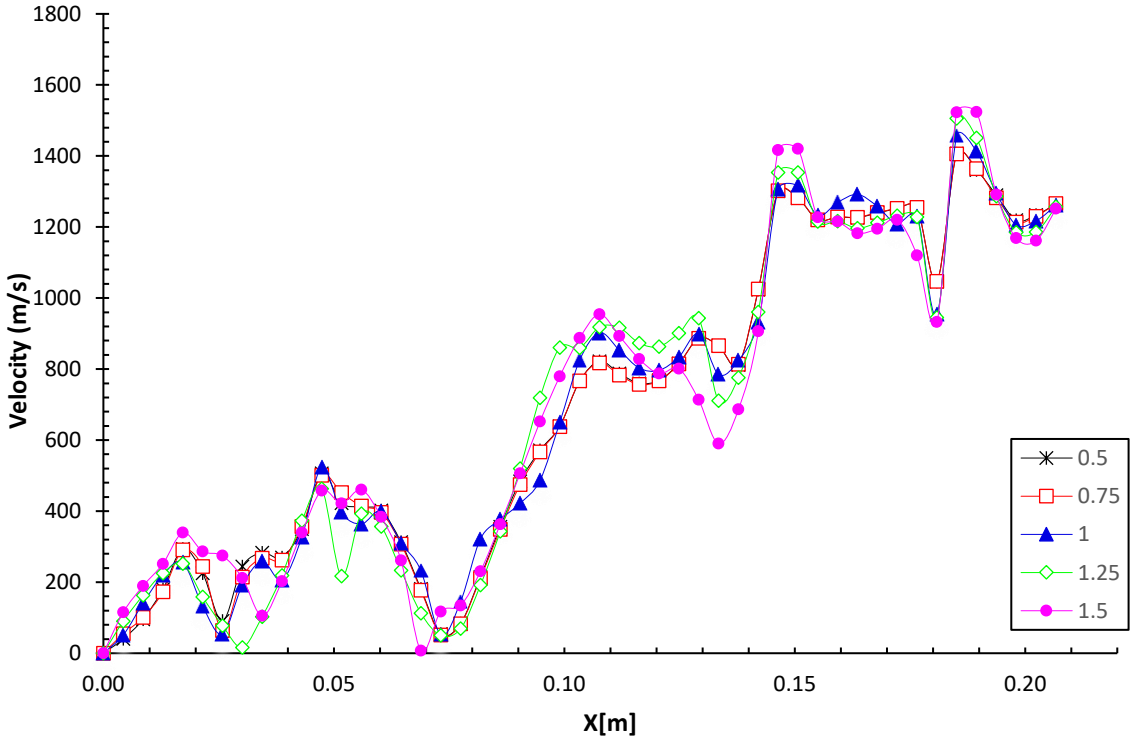

Figure 4.37. Ethane-Oxygen Velocity Equivalence 1 Shockwave at the Exit of Tube

Table 4.14. Ethane-Equivalence 1: Pressure, Temperature, and Velocity Contours Start

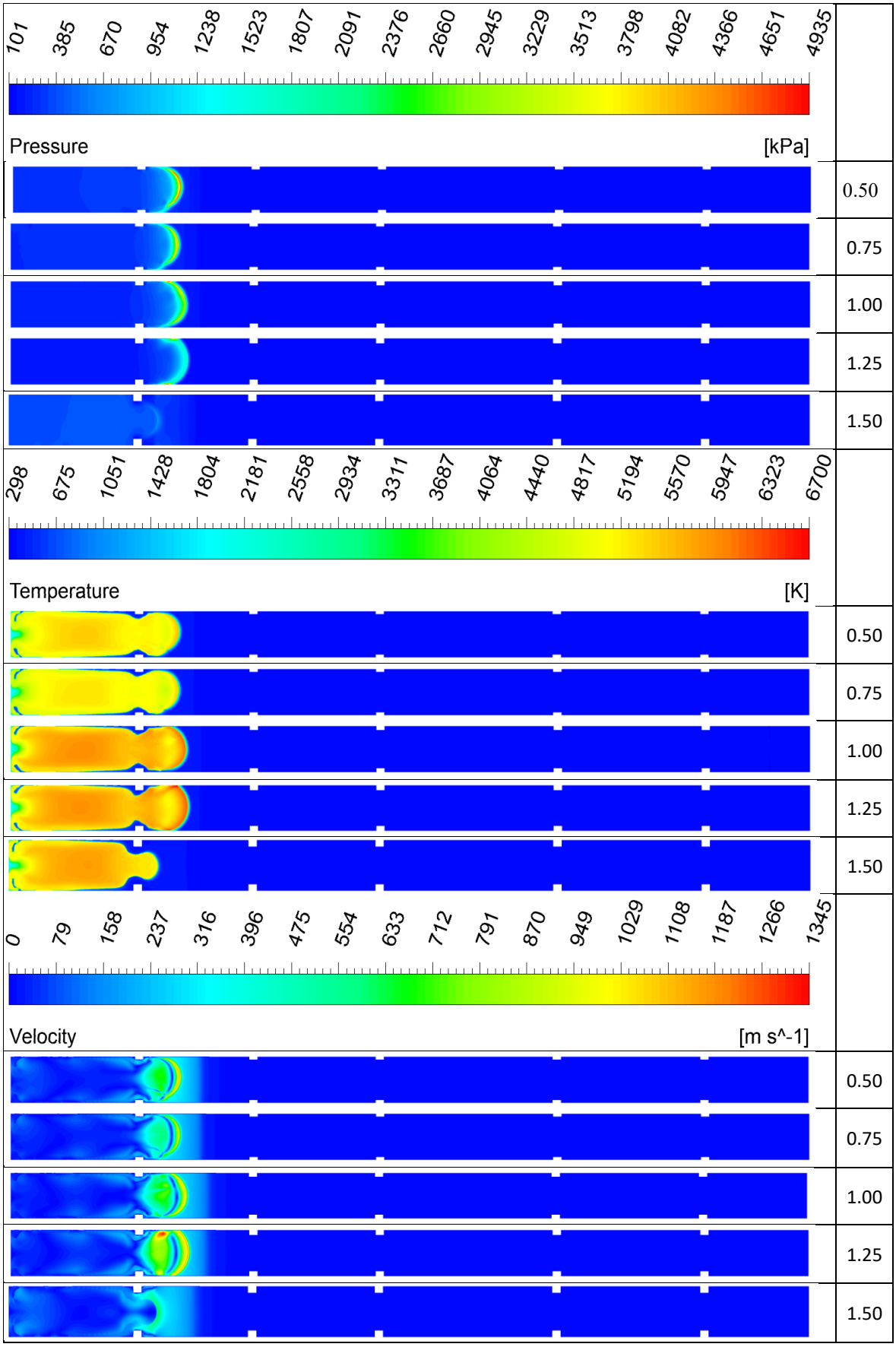

Table 4.15. Ethane-Equivalence 1: Pressure, Temperature, and Velocity Contours Exit

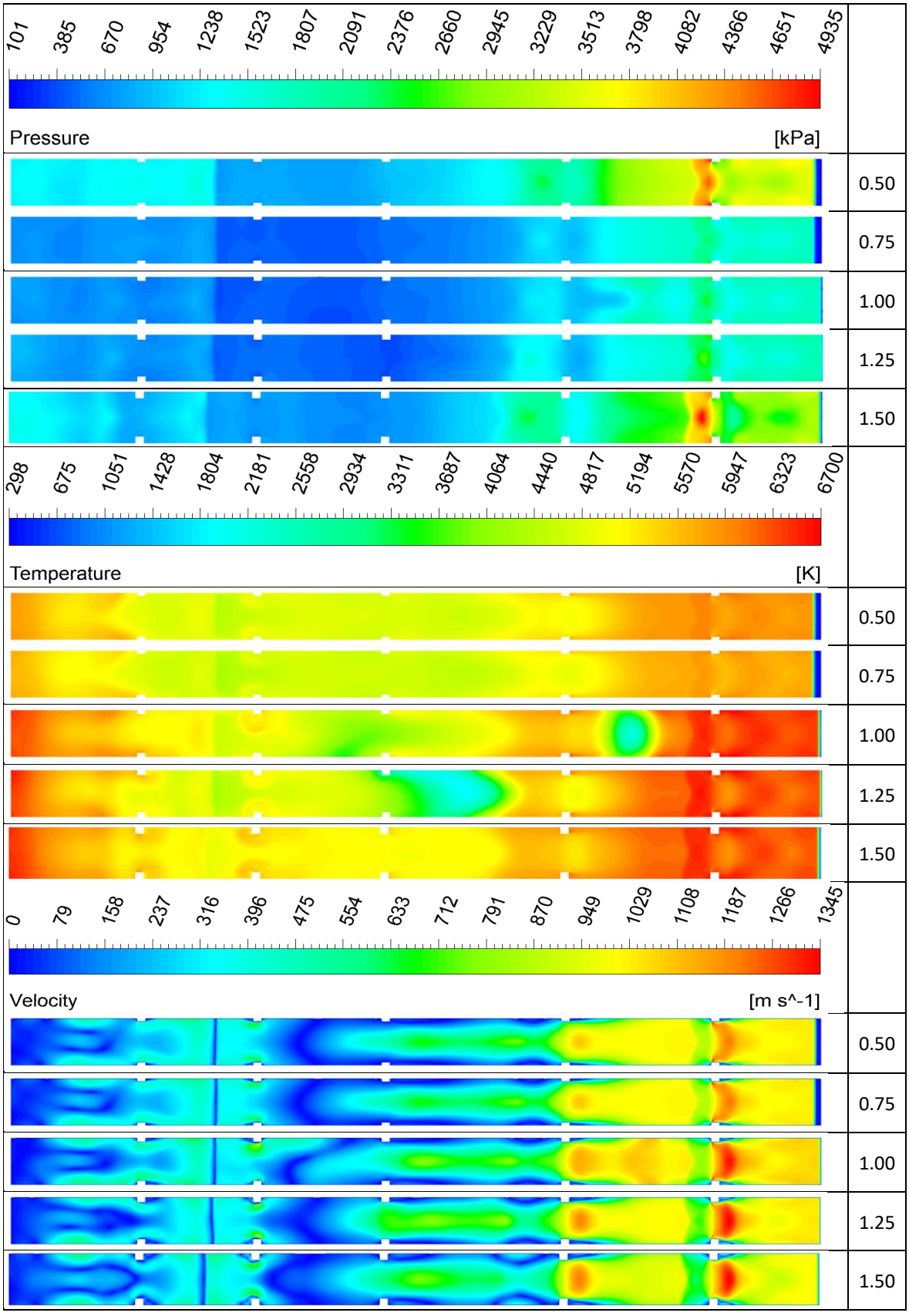

4.4. Methane

Methane fuel is highly stable. Methane fuel has a low risk of explosion and produces energy stably during the combustion process. Analysis of methane fuel revealed that shock waves failed to develop at any of the three possible equivalency ratios in our geometry. Micro-explosions, however, were caused when a certain amount of oxygen was added to the driving portion. It should be noted that these micro-explosions can lead to vibration loads that may jeopardize the design.

4.5. Kerosene

In the analysis of kerosene fuel, it was observed that shock waves did not form at an equivalence ratio of 1.5. On the other hand, at an equivalence ratio of 0.5, the shock wave formed in 0.468 milliseconds and exited the PDE in 0.066 milliseconds after formation. At an equivalence ratio of 1, the shock wave formed in 0.594 milliseconds and exited the PDE in 0.062 milliseconds after formation. Although the shock wave formed earlier at an equivalence ratio of 0.5, it did not exit the tube as quickly as it did under stoichiometric conditions. By examining Table 4.16, it was determined that the maximum pressure, temperature, and velocity values were achieved under stoichiometric conditions. For an equivalence ratio of 0.5, the maximum pressure, temperature, and velocity values were found to be 4230.66 kPa at a blockage height of 0.5 mm, 5420.07 K at 1 mm blockage height, and 1200.22 m/s at 1 mm blockage height, respectively. For an equivalence ratio of 1, the maximum pressure, temperature, and velocity values were found to be 5884.21 kPa at 1 mm blockage height, 7108.93 K at 1.25 mm blockage height, and 1325.18 m/s at 0.5 mm blockage height, respectively.

Table 4.16. Pressure, Temperature, and Velocity Values for Kerosene-Oxygen

Geometric Features		Molar Mass		Kerosene [0.5]		
a	b	$[C_{12}H_{23}]$	0.128	P[kPa]	T[K]	V[m/s]
0.5	2.18	$[O_2]$	0.872	4230.66	5264.76	1194.05
0.75	2.18			4057.98	5227.15	1147.74
1	2.18			4144.82	5420.07	1200.22
1.25	2.18			4047.28	5201.82	1153.55
1.5	2.18			4055.36	5201.02	1152.61
Geometric Features		Molar Mass		Kerosene [1]		
a	b	$[C_{12}H_{23}]$	0.227	P[kPa]	T[K]	V[m/s]
0.5	2.18	$[O_2]$	0.773	5881.48	7082.56	1325.18
0.75	2.18			5862.51	7092.29	1314.33
1	2.18			5884.21	7103.16	1324.46
1.25	2.18			5879.13	7108.93	1322.91
1.5	2.18			5865.93	7085.25	1312.84

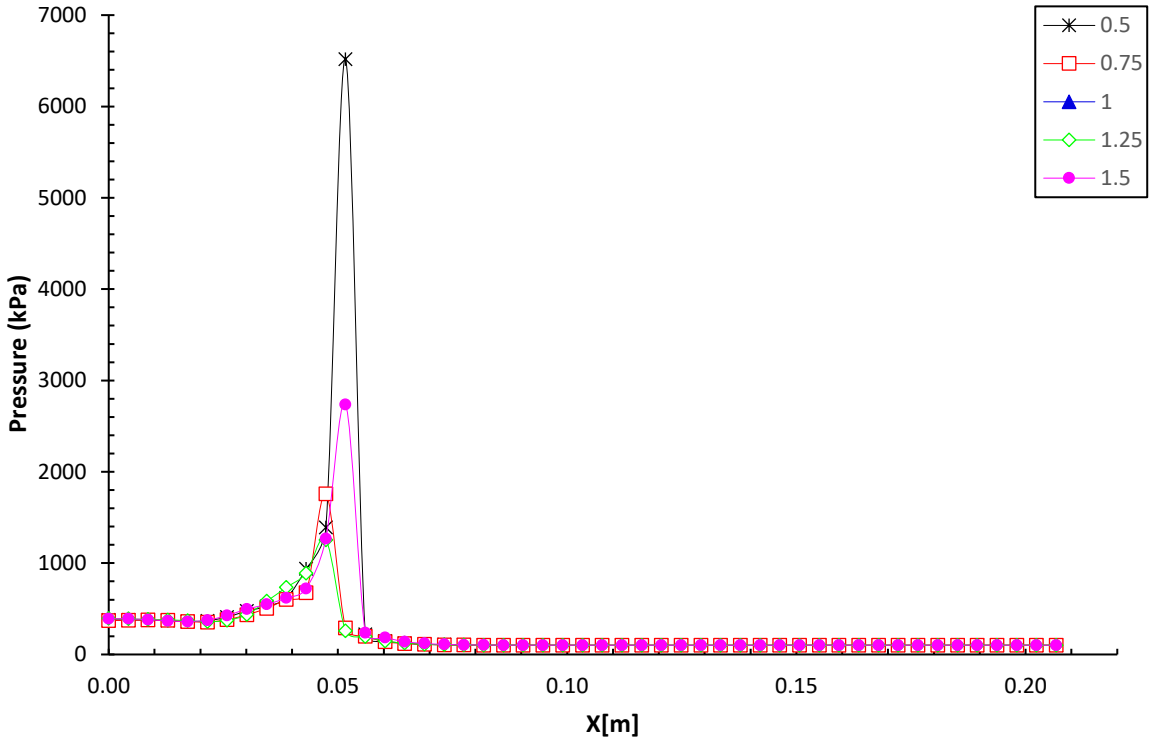

Figure 4.38. Kerosene-Oxygen Pressure Equivalence 0.5 Shockwave Starting Point

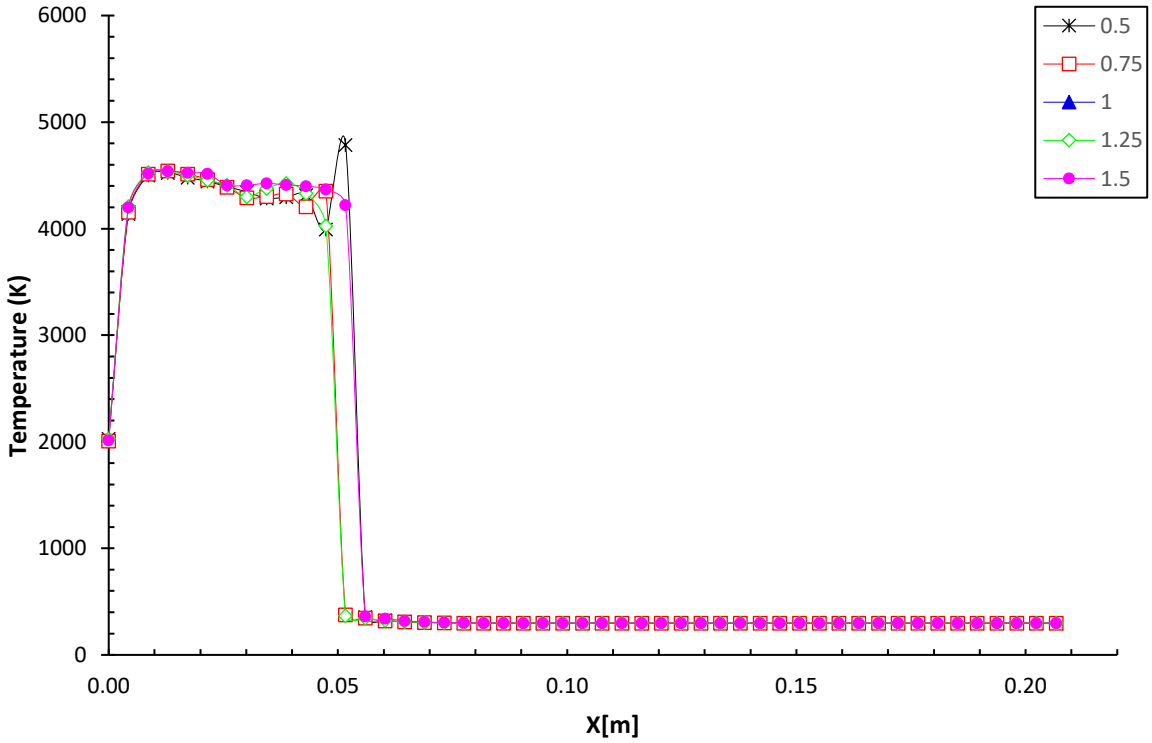

Figure 4.39. Kerosene-Oxygen Temperature Equivalence 0.5 Shockwave Starting Point

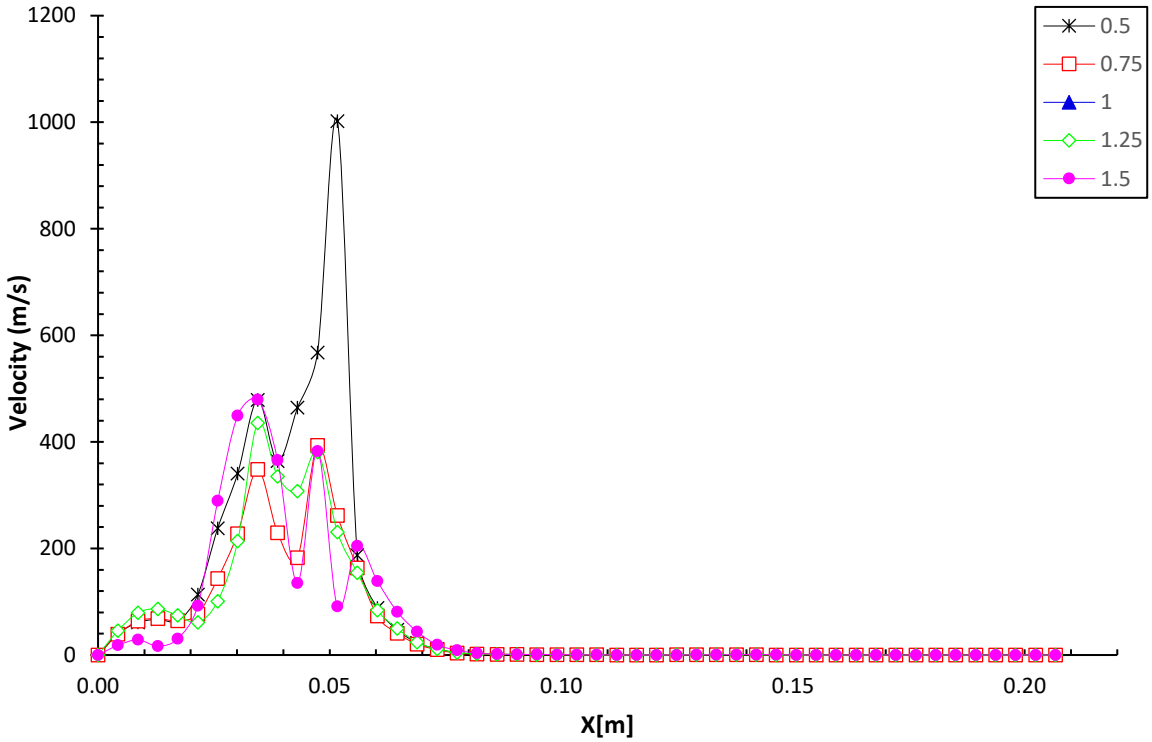

Figure 4.40. Kerosene-Oxygen Velocity Equivalence 0.5 Shockwave Starting Point

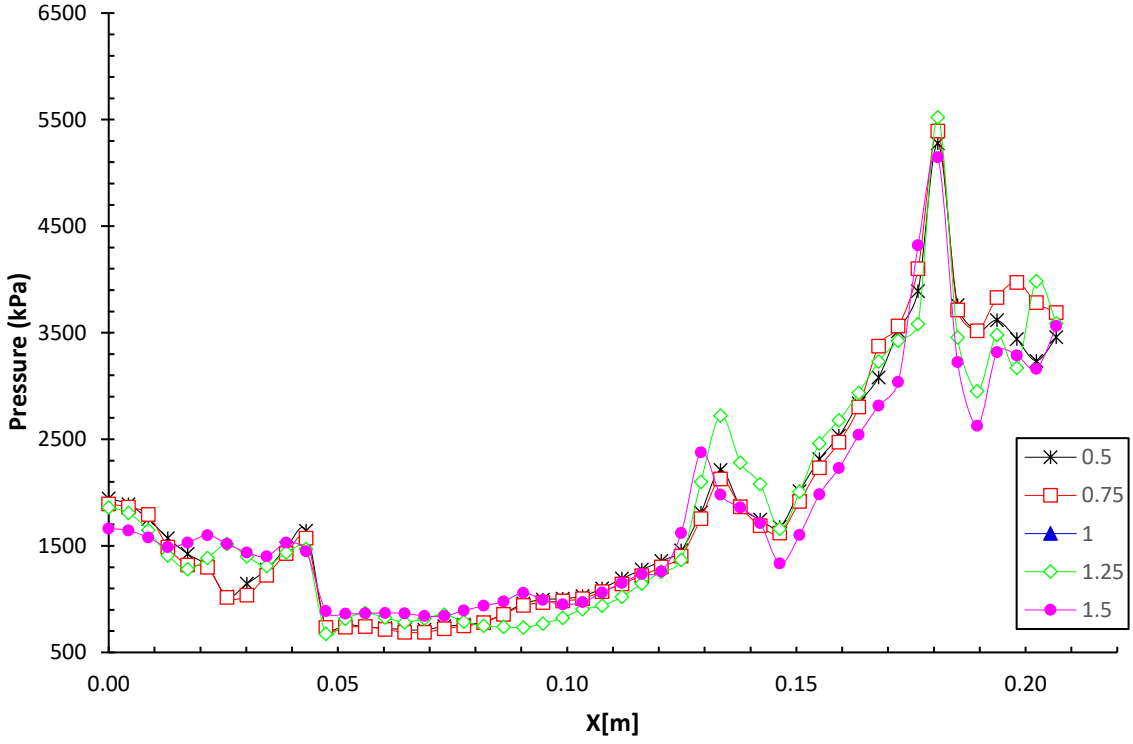

Figure 4.41. Kerosene-Oxygen Pressure Equivalence 0.5 Shockwave at the Exit of Tube

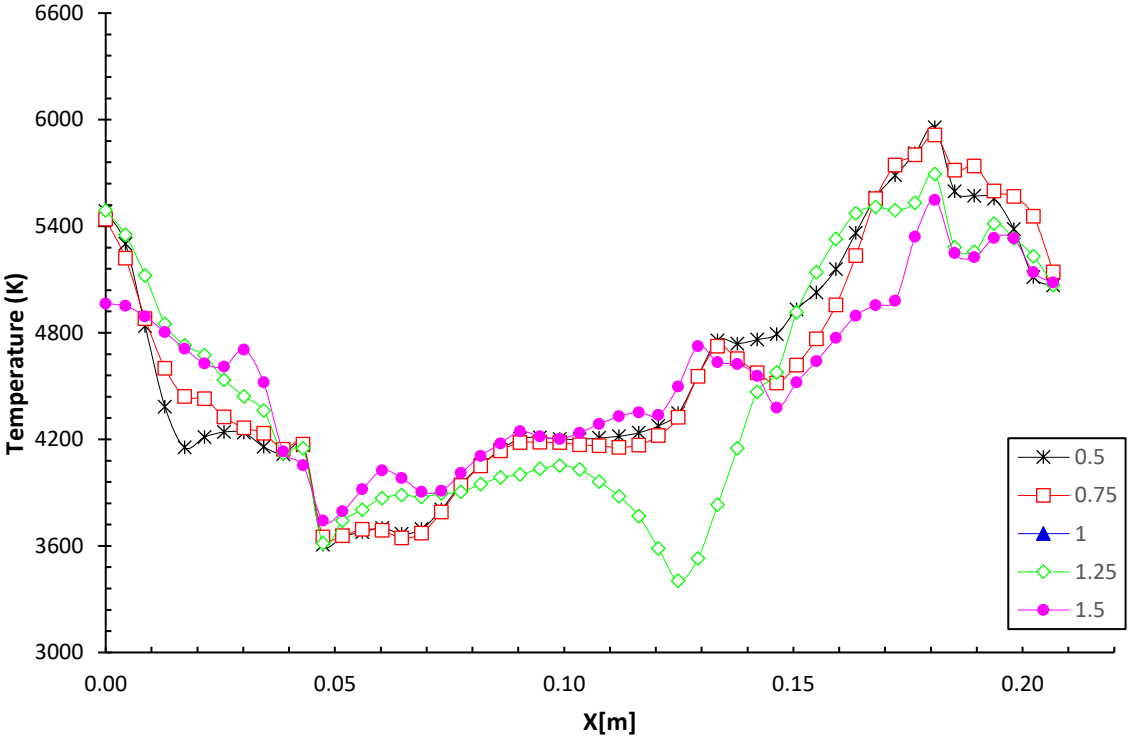

Figure 4.42. Kerosene-Oxygen Temperature Equivalence 0.5 Shockwave at the Exit of Tube

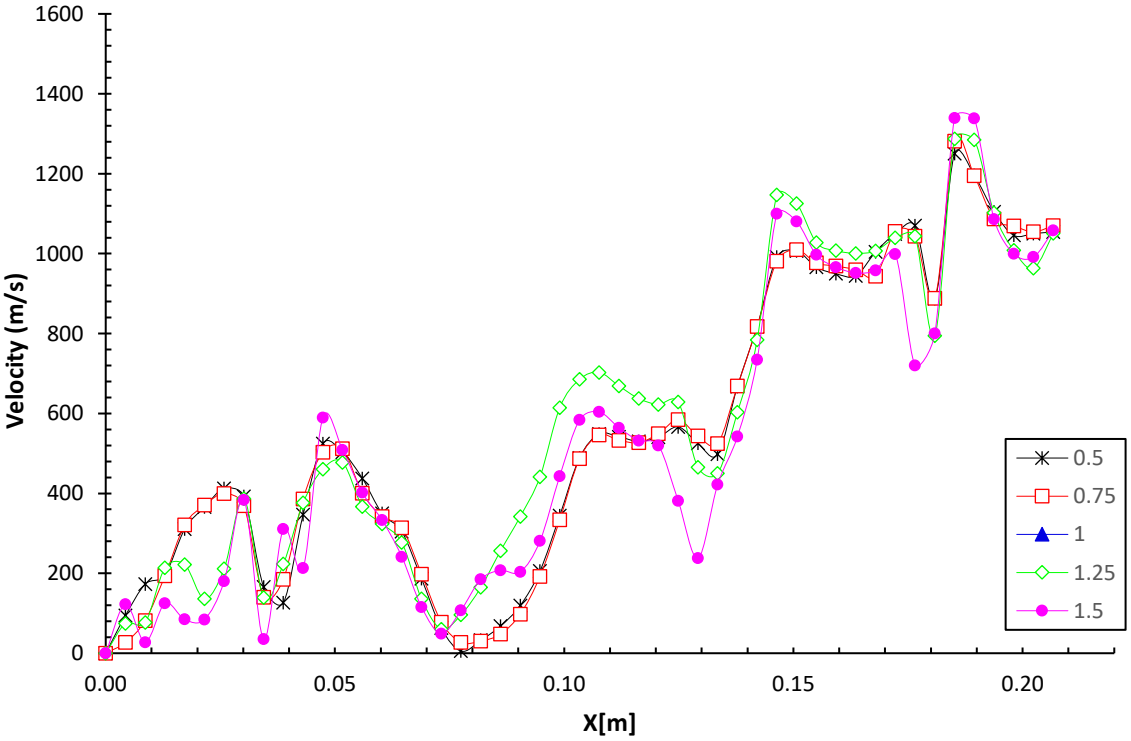

Figure 4.43. Kerosene-Oxygen Velocity Equivalence 0.5 Shockwave at the Exit of Tube

Upon examining Table 4.17, it was observed that at an equivalence ratio of 0.5, the shock wave formed in the middle between the first and second obstacles.

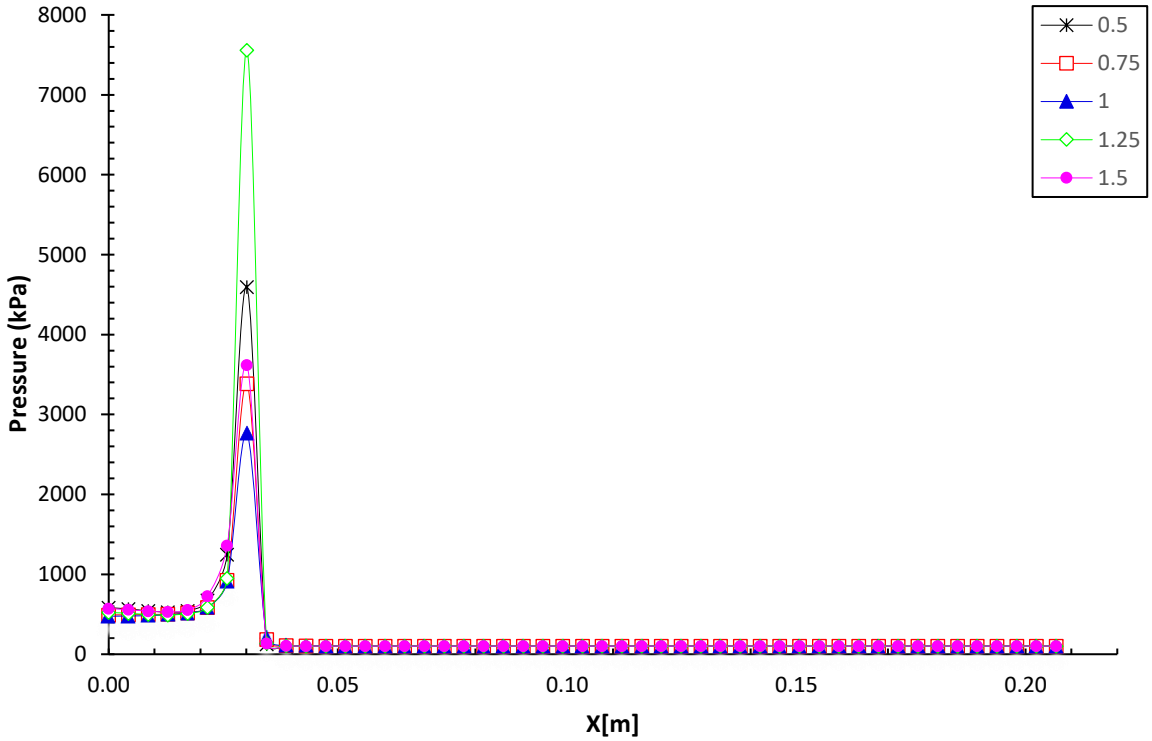

Figure 4.44. Kerosene-Oxygen Pressure Equivalence 1 Shockwave Starting Point

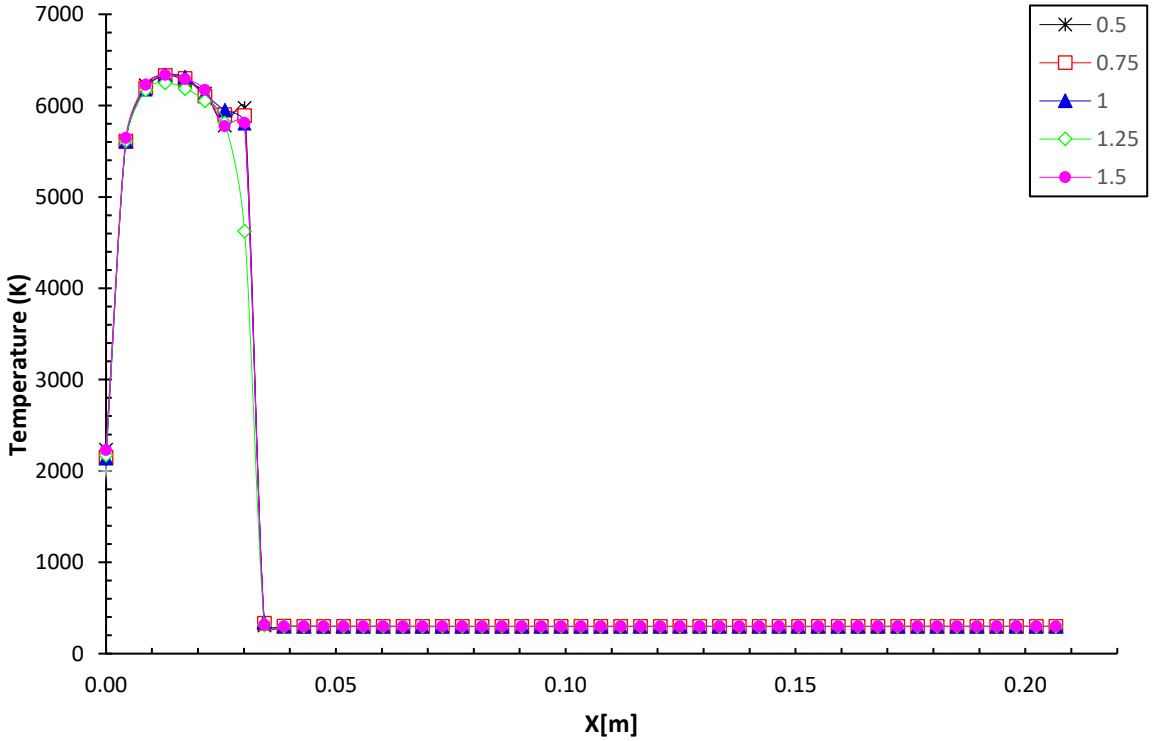

Figure 4.45. Kerosene-Oxygen Temperature Equivalence 1 Shockwave Starting Point

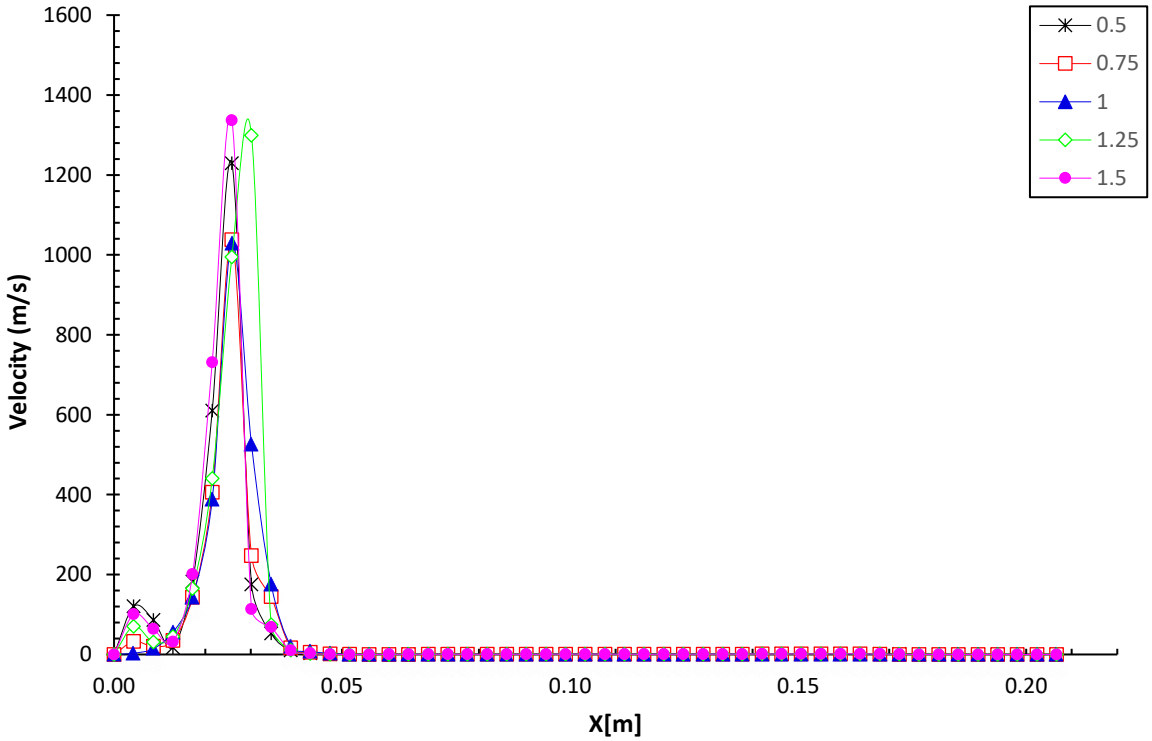

Figure 4.46. Kerosene-Oxygen Velocity Equivalence 1 Shockwave Starting Point

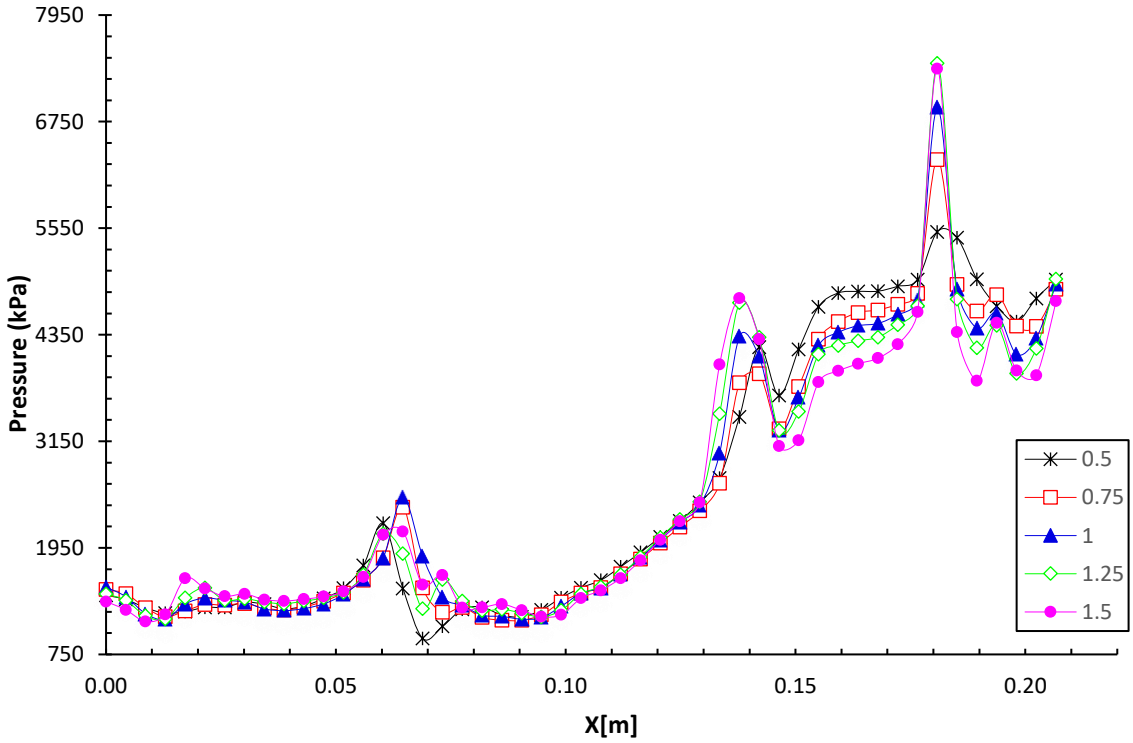

Figure 4.47. Kerosene-Oxygen Pressure Equivalence 1 Shockwave at the Exit of Tube

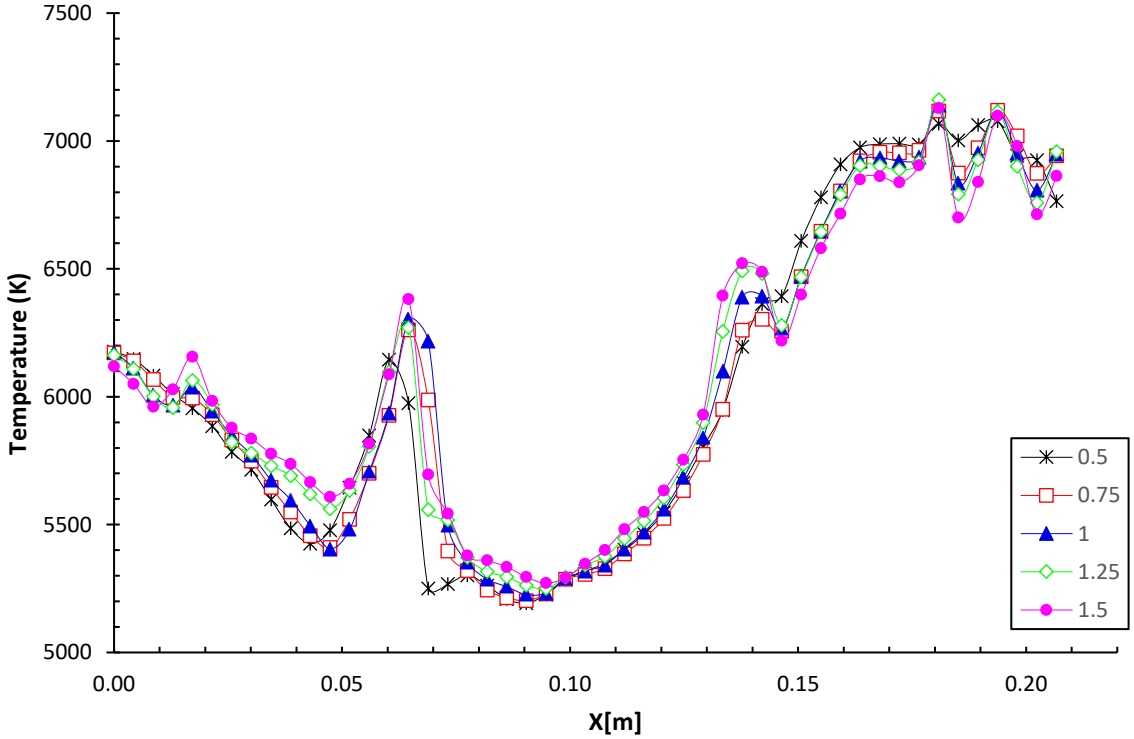

Figure 4.48. Kerosene-Oxygen Temperature Equivalence 1 Shockwave at the Exit of Tube

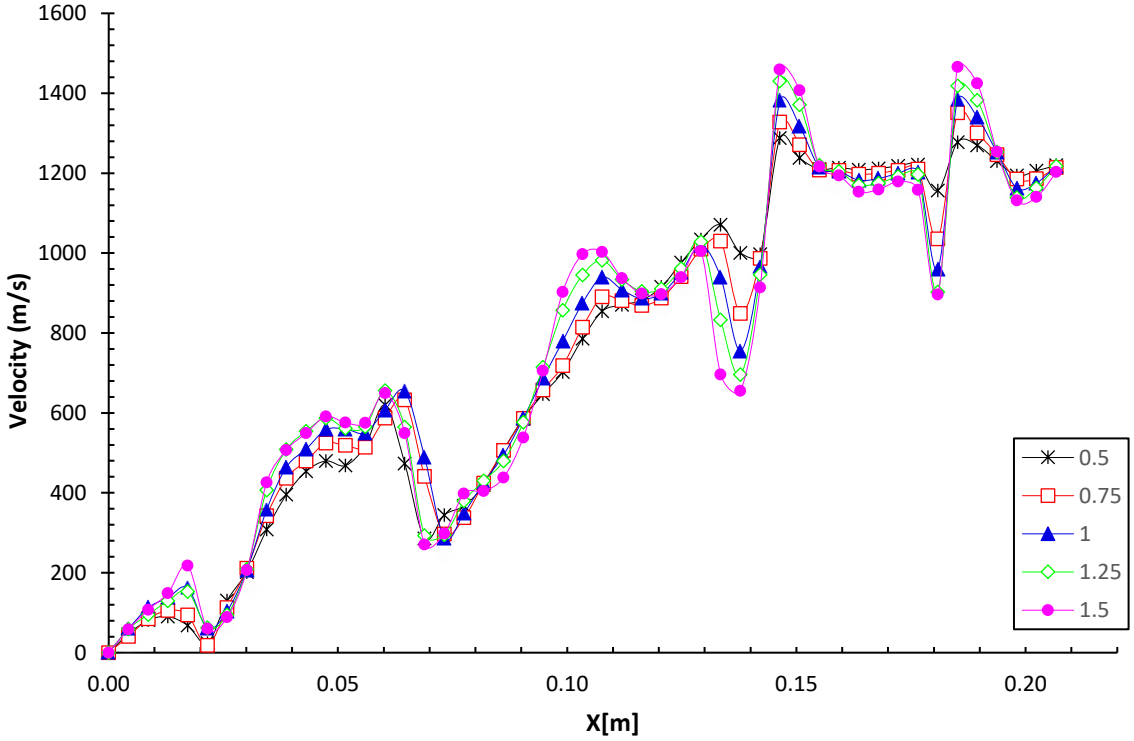

Figure 4.49. Kerosene-Oxygen Velocity Equivalence 1 Shockwave at the Exit of Tube

Table 4.19, it was found that the shock wave formed right at the entrance of the first obstacle.

Table 4.17. Kerosene-Equivalence 0.5: Pressure, Temperature, and Velocity Contours Start

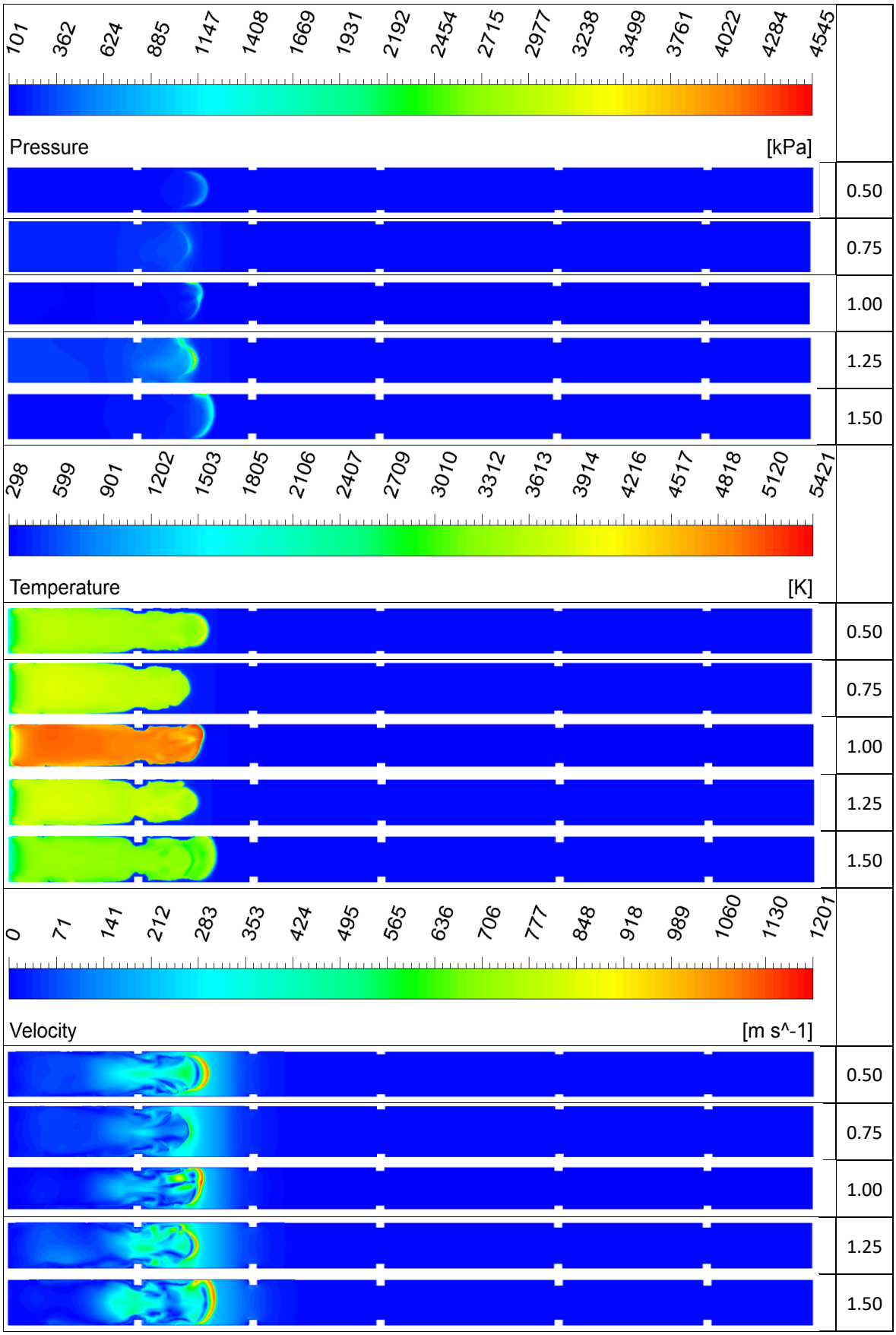

Table 4.18. Kerosene-Equivalence 0.5: Pressure, Temperature, and Velocity Contours Exit

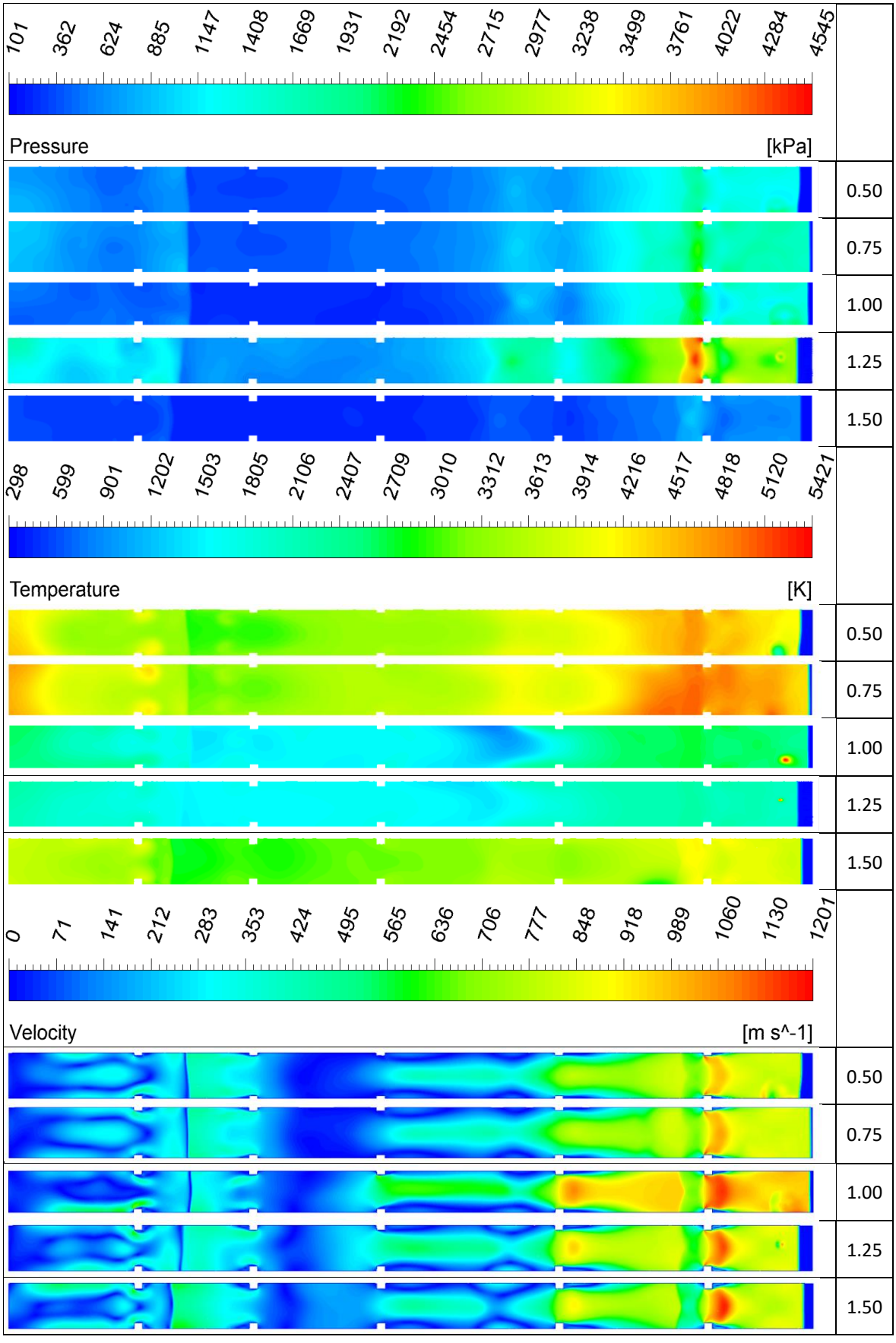

Table 4.19. Kerosene-Equivalence 1: Pressure, Temperature, and Velocity Contours Start

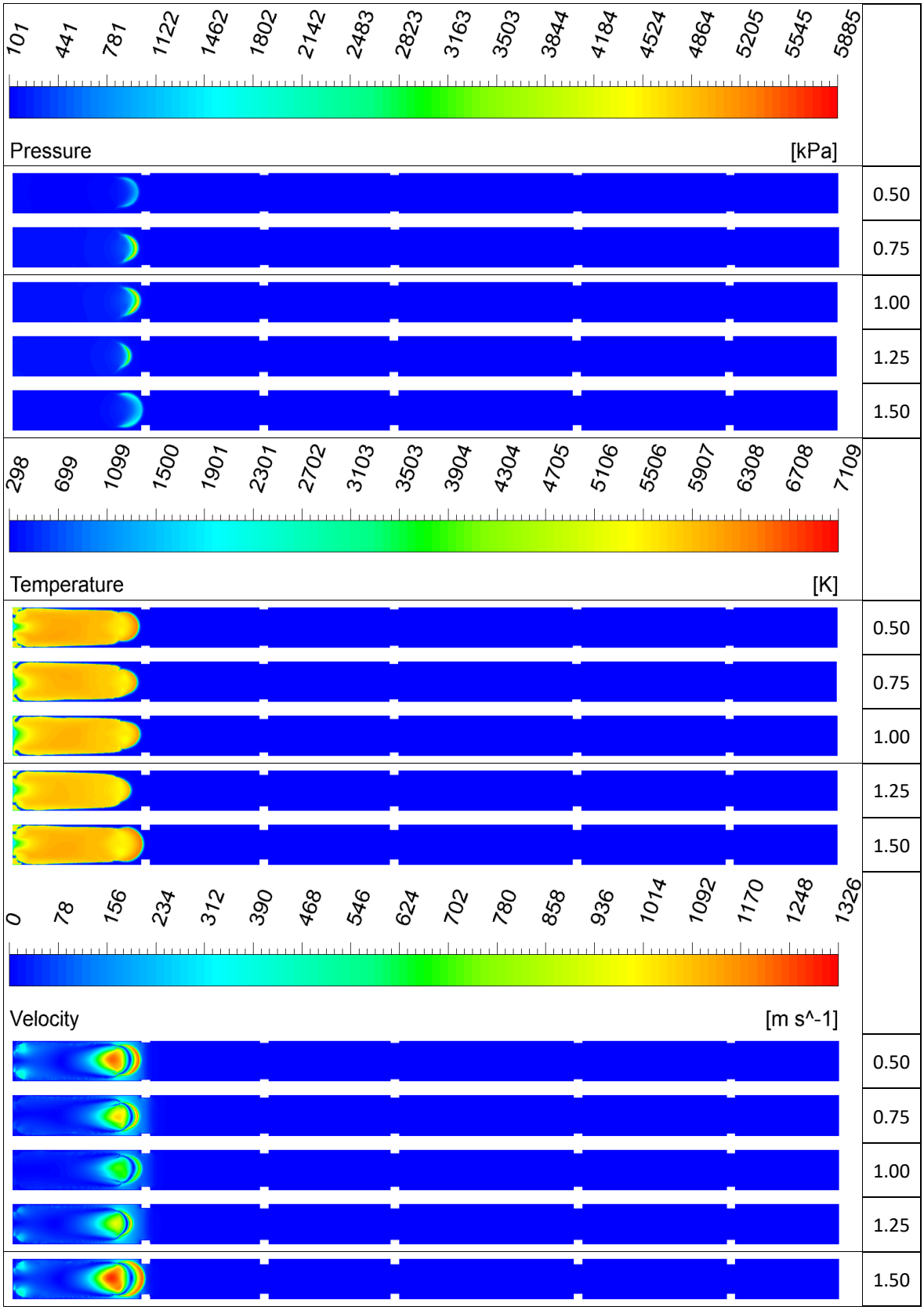

Table 4.20. Kerosene-Equivalence 1: Pressure, Temperature, and Velocity Contours Exit

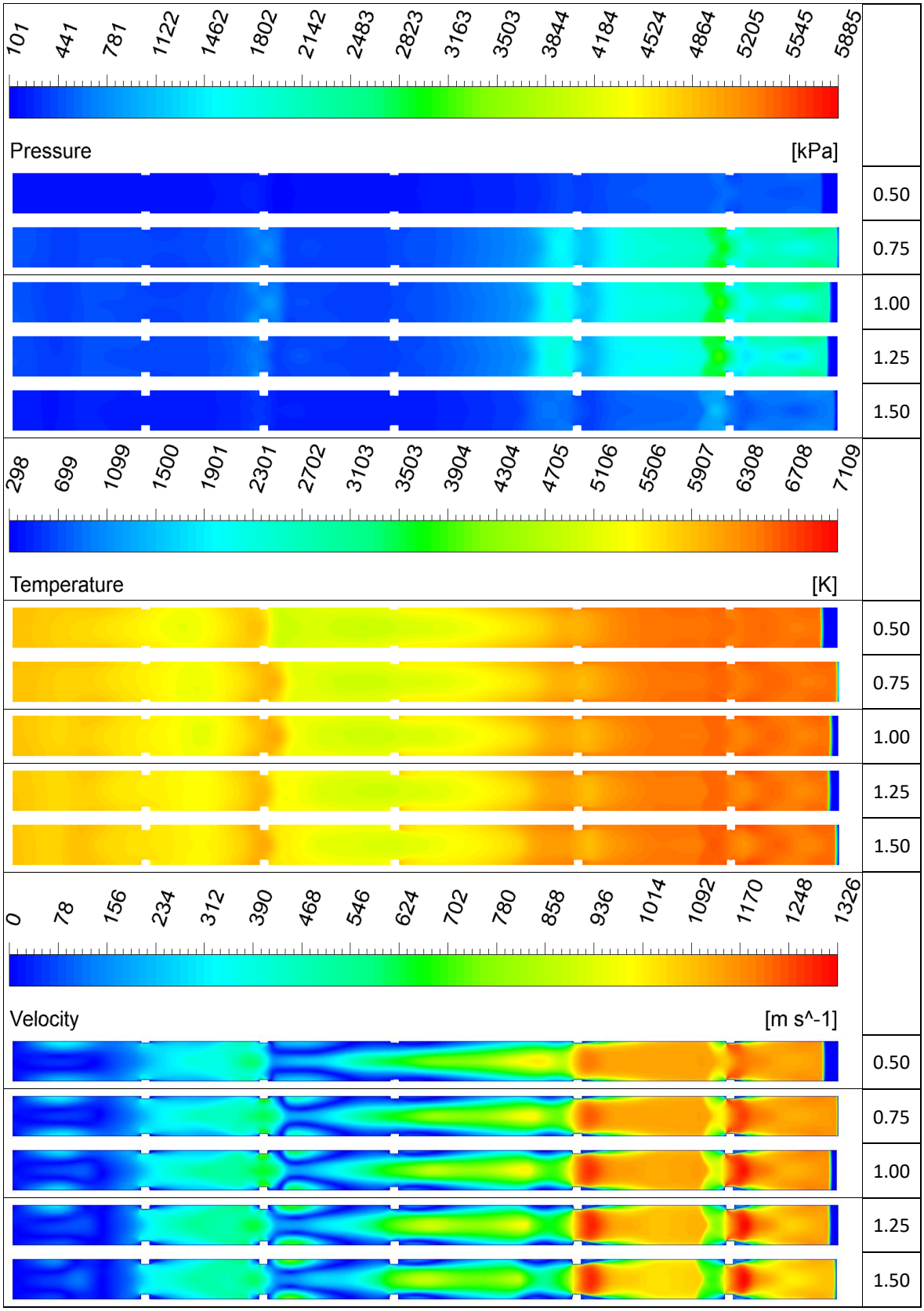

4.6. Hydrogen

The shock wave formed in 0.084 milliseconds and left the PDE in 0.051 milliseconds after generation when hydrogen fuel was evaluated. Upon examining Table 4.21, it was found that for an equivalence ratio of 0.5 and hydrogen fuel, the maximum pressure and velocity values were 2103.47 kPa and 1672.64 m/s, respectively, and these values were achieved at a blockage height of 0.5 mm. The maximum temperature, on the other hand, was observed to be 4322.37 K at a blockage height of 0.75 mm.

Table 4.21. Pressure, Temperature, and Velocity for Hydrogen-Oxygen

Geometric Features		Molar Mass		Hydrogen [0.5]		
a	b	$[H_2]$	0.2	P[kPa]	T[K]	V[m/s]
0.5	2.18	$[O_2]$	0.8	2103.47	4287.39	1672.64
0.75	2.18			2088.00	4322.37	1579.44
1	2.18			2064.78	4274.37	1593.11

Upon examining Table 4.22(a), it was observed that at an equivalence ratio of 0.5 and a blockage height of 1.25 mm, a shock wave forms from the right side of the tube. Similarly, in Table 4.22(b) for an equivalence ratio of 1, and Table 4.22(c) for a blockage height of 1.5 mm, another shock wave is observed to form from the right side of the tube. As the equivalence ratio increases, it is observed that the shock formed on the right side moves towards the left.

The curves for the equivalence ratios of 0.5 are presented in Figure 4.50, Figure 4.51, and Figure 4.52, respectively. These figures represent the time elapsed until shock wave formed. The figures 4.53, 4.54, and Figure 4.55 illustrate the changes caused by the shock wave as it progresses through the tube towards the exit. These graphs show how pressure, temperature, and velocity change along the PDE. Contours for equivalence ratios 0.5 are presented in Table 4.23 and Table 4.24.

.

Table 4.22. Hydrogen-Oxygen Multiple Shock State in PDE

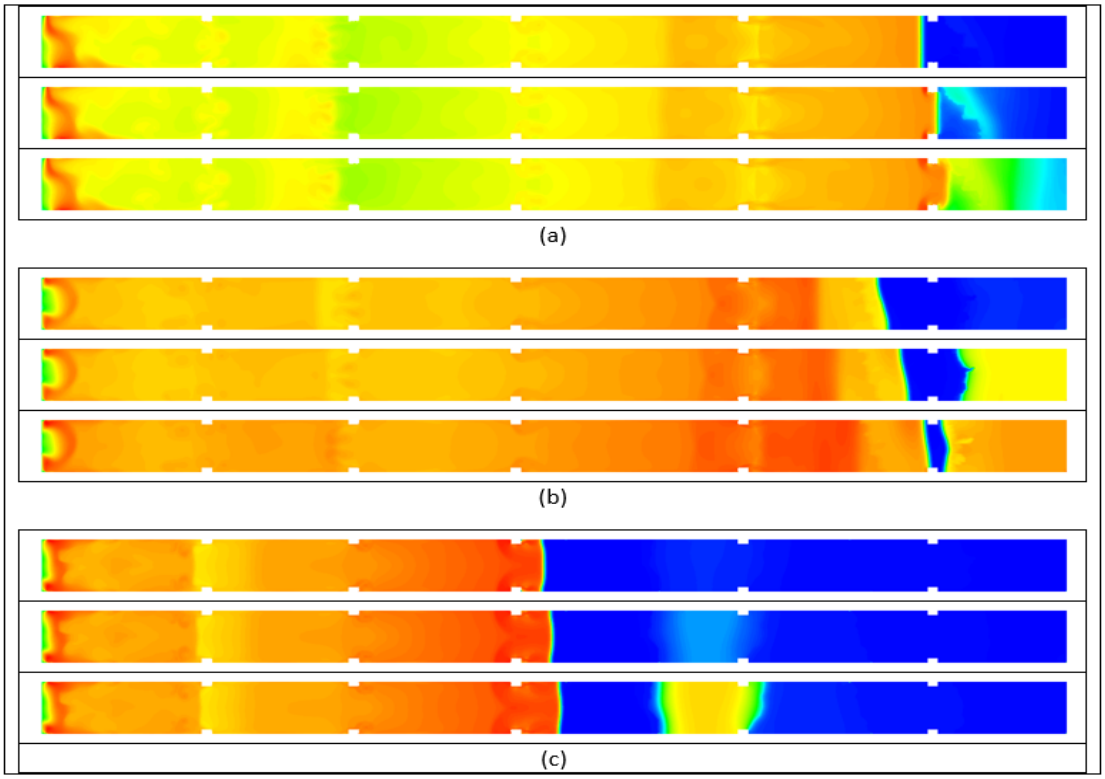

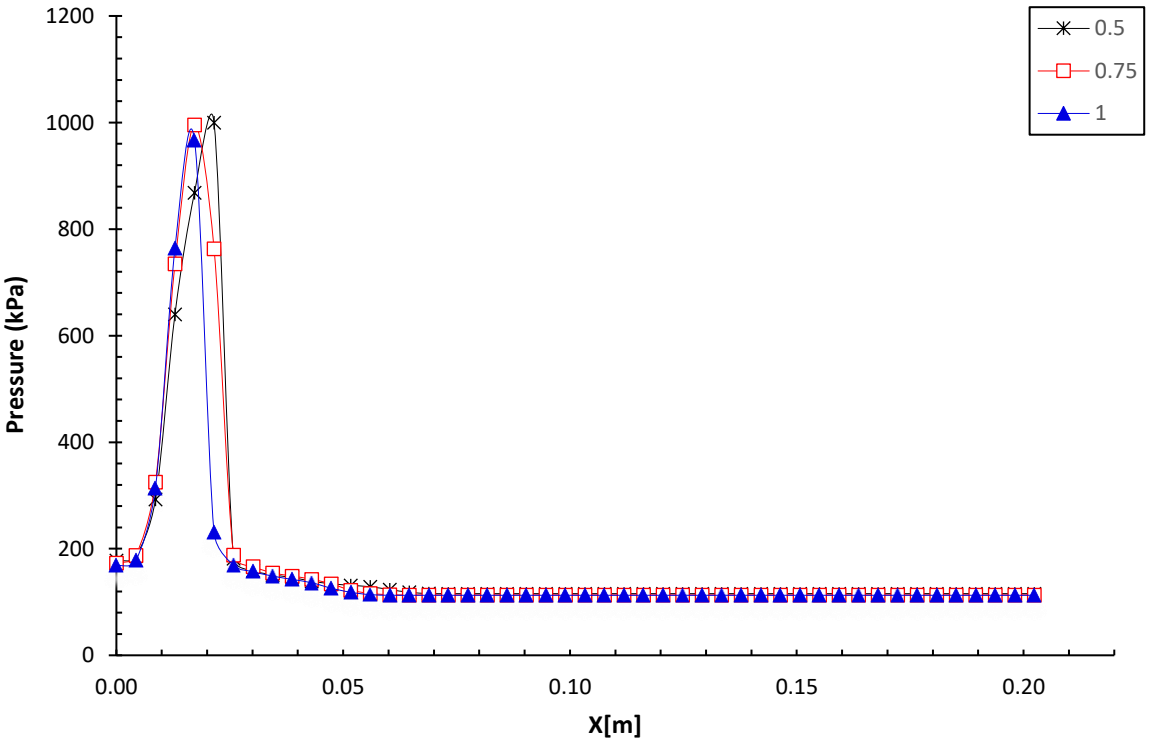

Figure 4.50. Hydrogen-Oxygen Pressure Equivalence 0.5 Shockwave Starting Point

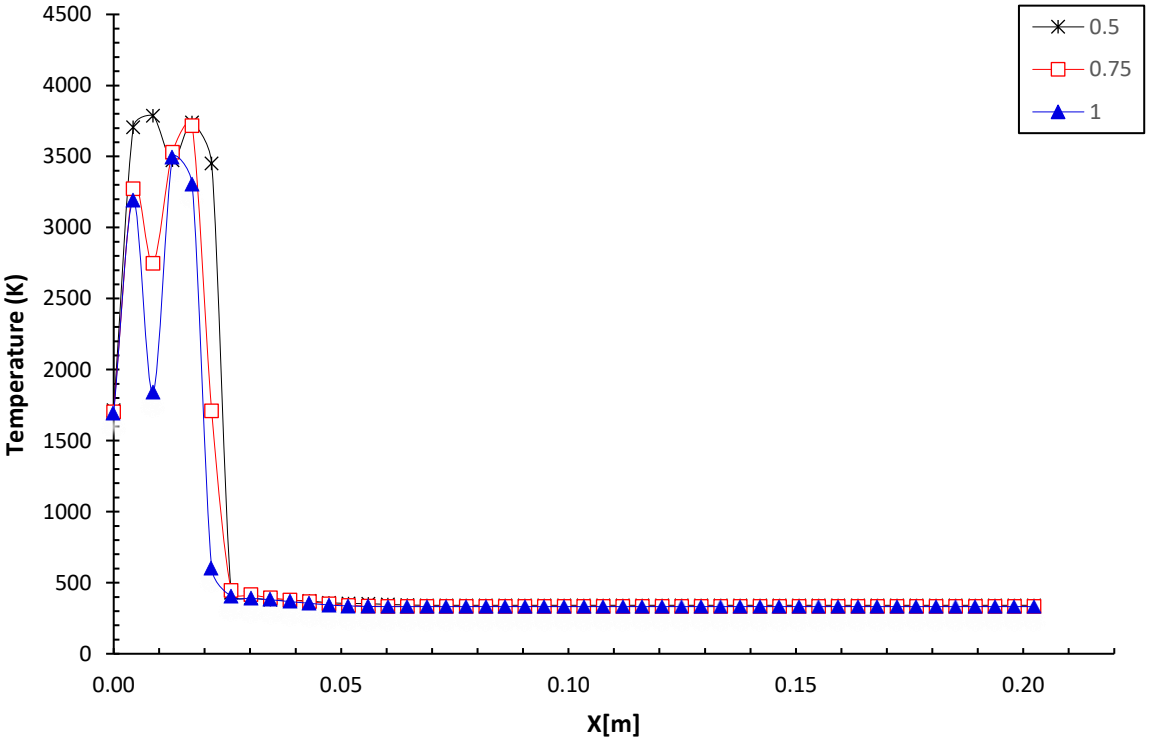

Figure 4.51. Hydrogen-Oxygen Temperature Equivalence 0.5 Shockwave Starting Point

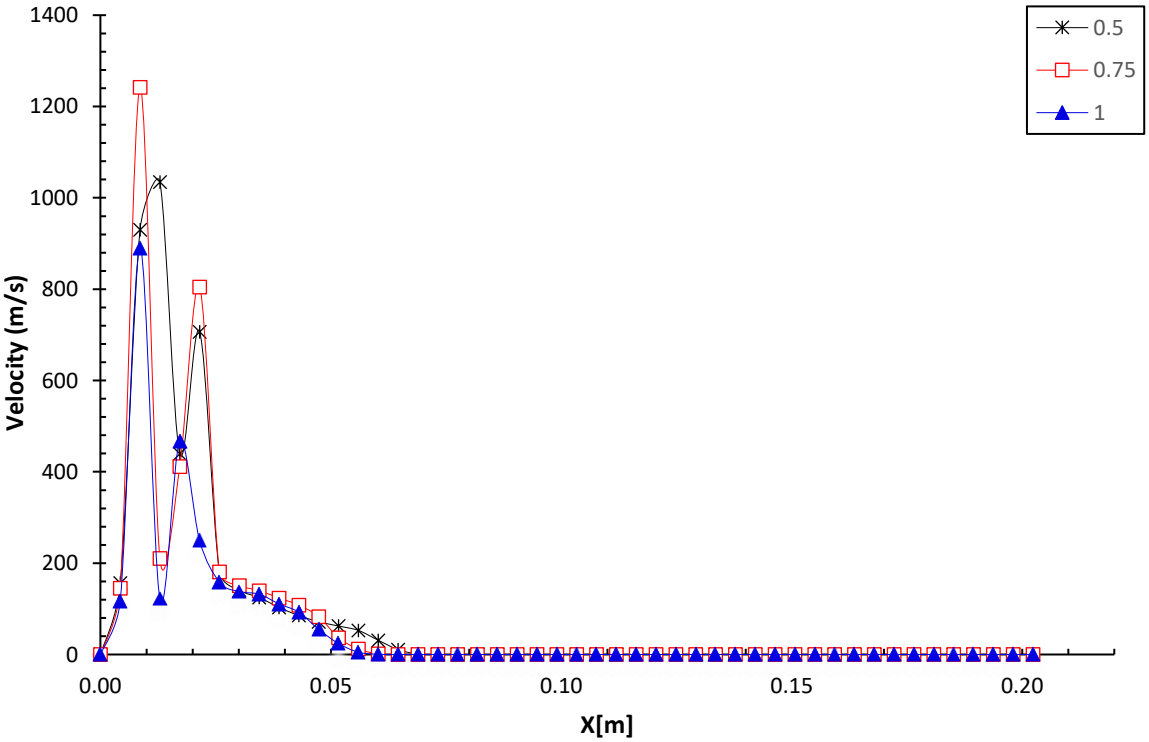

Figure 4.52. Hydrogen-Oxygen Velocity Equivalence 0.5 Shockwave Starting Point

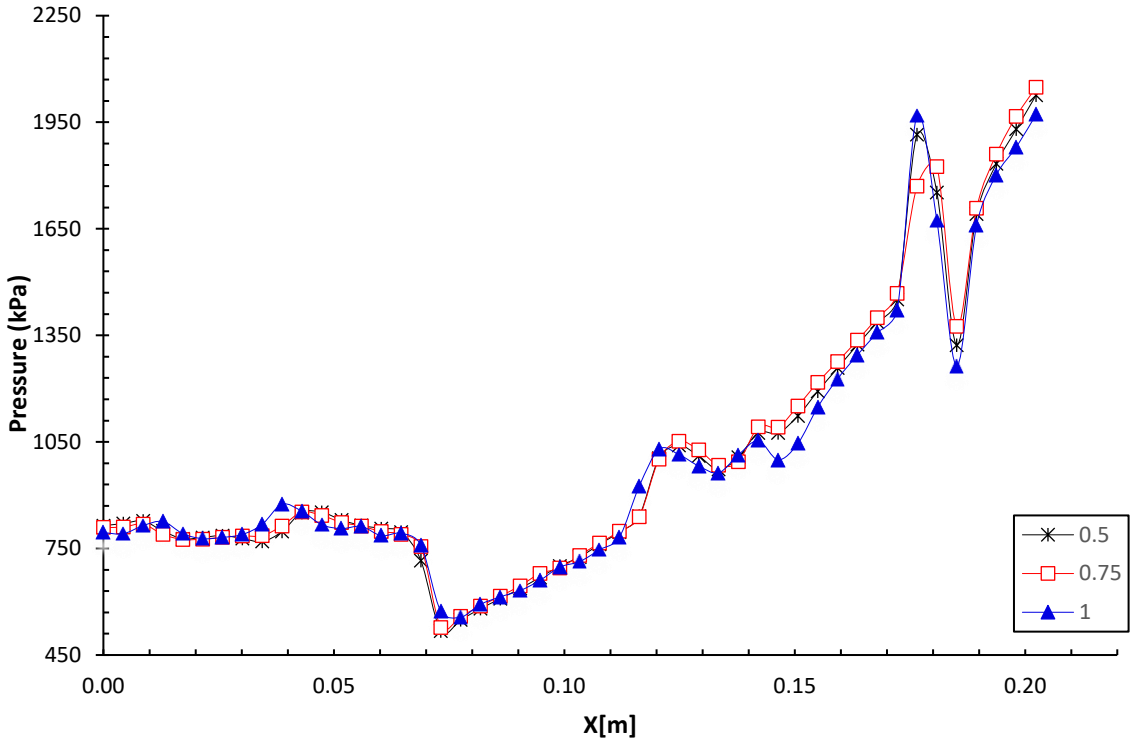

Figure 4.53. Hydrogen-Oxygen Pressure Equivalence 0.5 Shockwave at the Exit of Tube

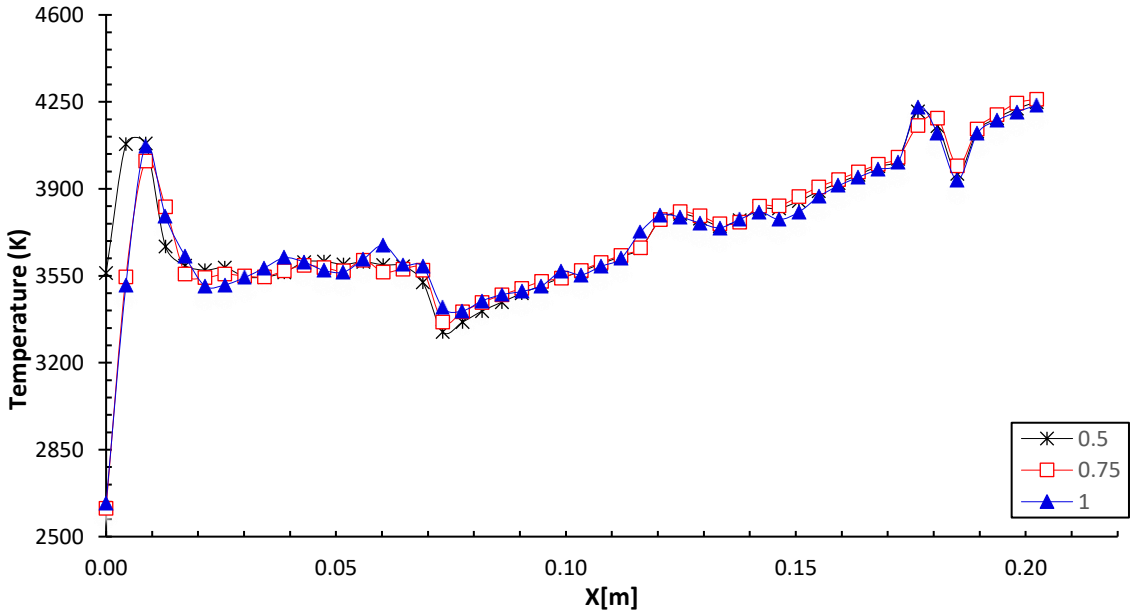

Figure 4.54. Hydrogen-Oxygen Temperature Equivalence 0.5 Shockwave at the Exit of Tube

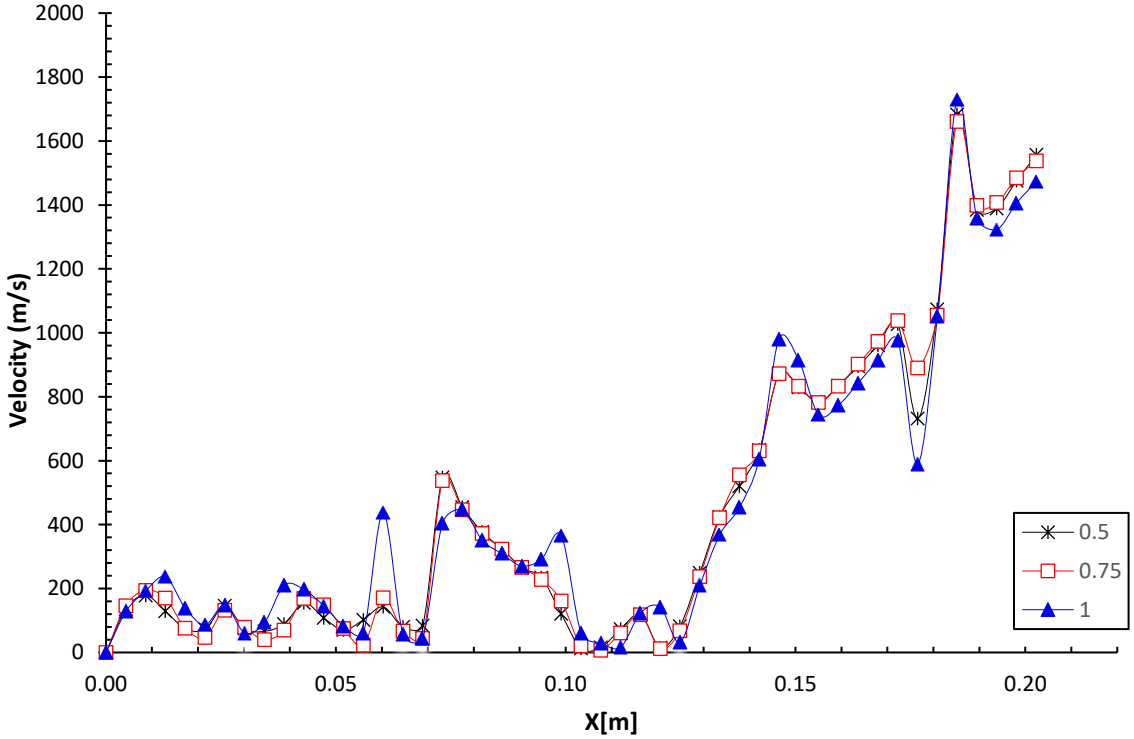

Figure 4.55. Hydrogen-Oxygen Velocity Equivalence 0.5 Shockwave at the Exit of Tube

Table 4.23. Hydrogen-Equivalence 0.5: Pressure, Temperature, andVelocity Contours Start

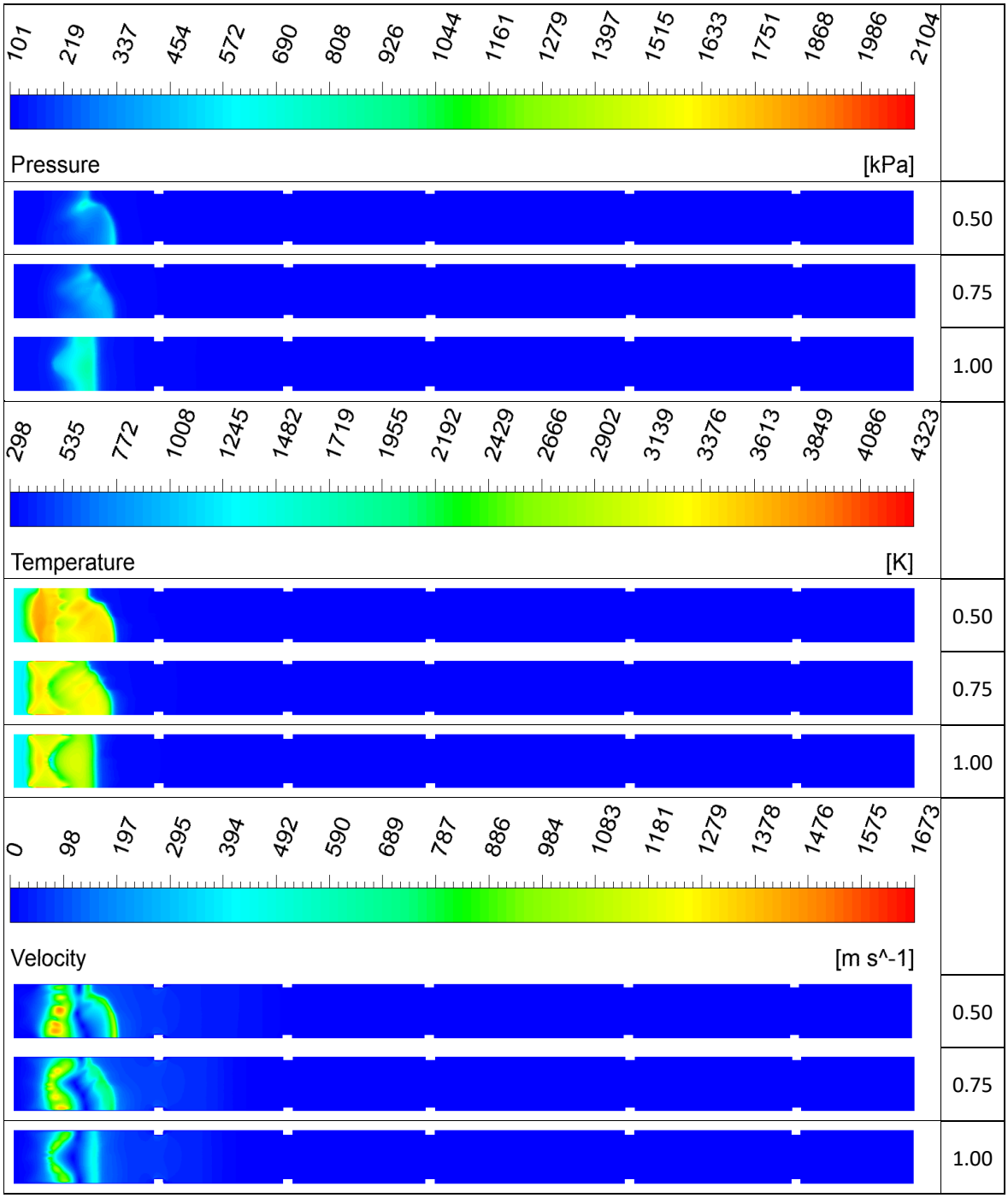

Table 4.24. Hydrogen-Equivalence 0.5: Pressure, Temperature, and Velocity Contours Exit

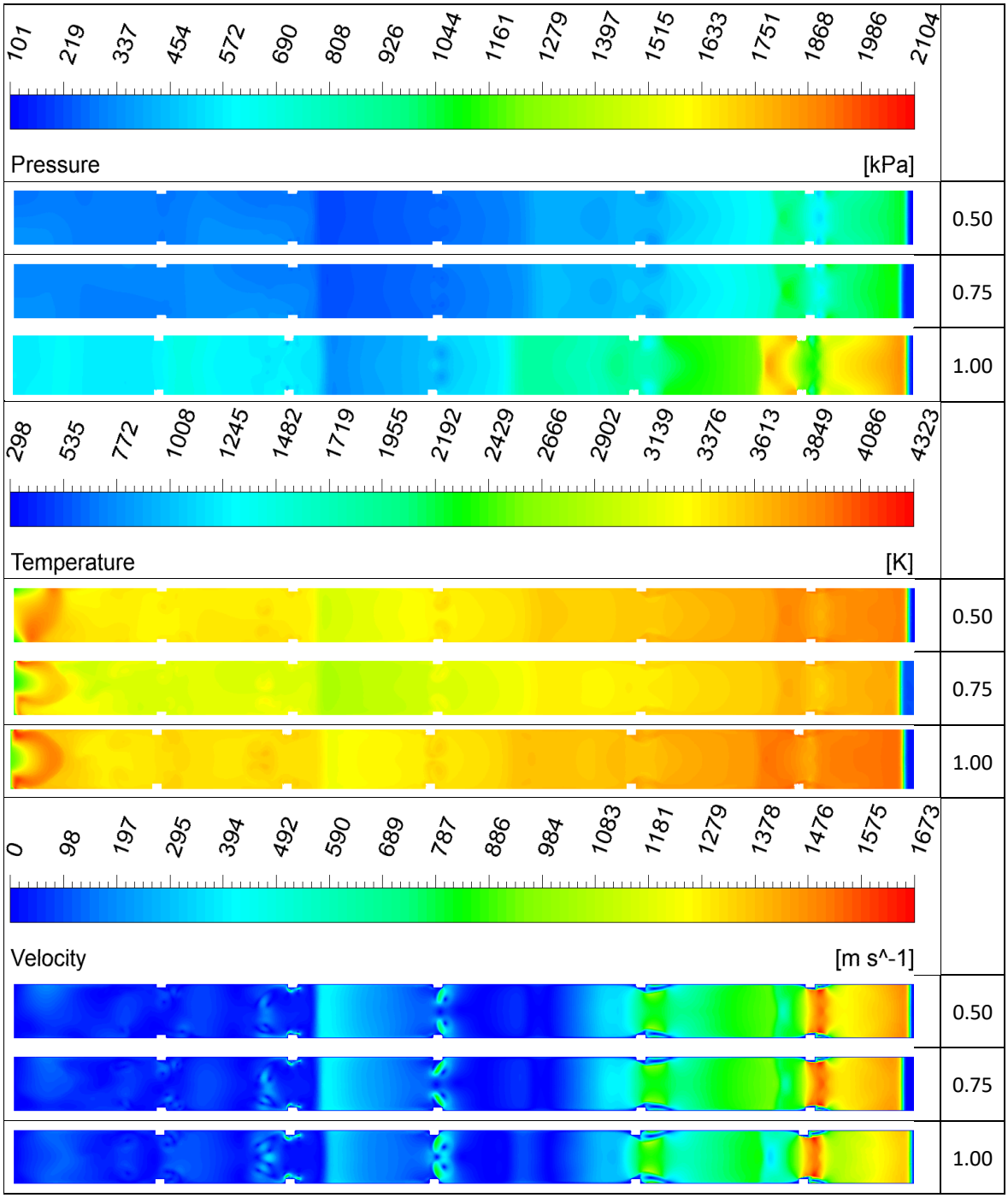

4.7. General Conclusions 1

The variations in maximum pressure values of the fuels used in the thesis study concerning equivalence ratios are shown in Figure 4.56. At an equivalence ratio of 0.5, it can be observed that only kerosene and hydrogen do not result in the formation of a shock wave. The maximum pressure value at an equivalence ratio of 0.5 is determined to be 4544.82 kPa for kerosene, and the minimum pressure value is 2103.47 kPa for hydrogen fuel. At an equivalence ratio of 1, the maximum pressure value is found to be 5884.21 kPa for kerosene, and the minimum pressure value is 4227.71 kPa for acetylene fuel. For an equivalence ratio of 1.5, the maximum pressure occurs at 4069.46 kPa for ethylene fuel, and the minimum pressure is 3729.03 kPa for acetylene fuel. Analyzing the pressure values among the fuels, it is determined that kerosene fuel reaches the highest maximum pressure value, which is 5884.21 kPa.

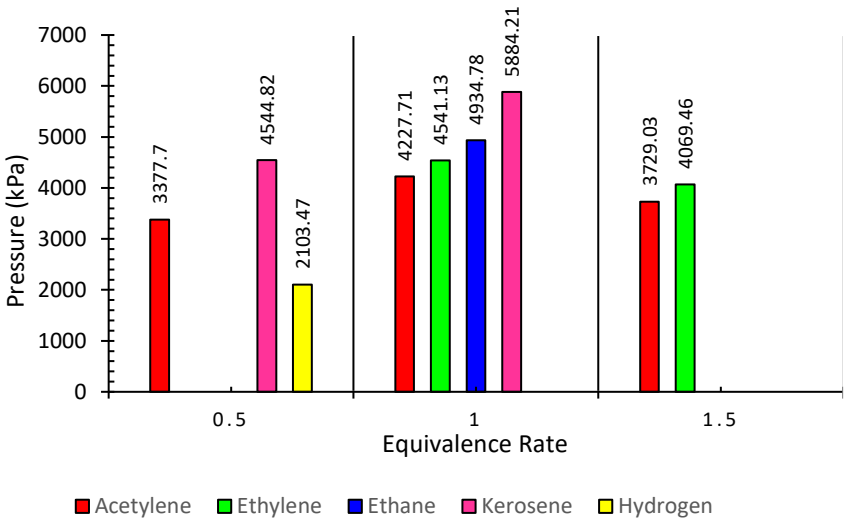

Figure 4.56. Pressure Equivalence

The maximum temperature for acetylene fuel is found at 6304.78 K when examining Figure 4.57 with an equivalency ratio of 0.5. Similarly, at an equivalence ratio of 0.5, the minimum temperature is determined to be 4322.37 K for hydrogen fuel.

At an equivalence ratio of 1, the maximum temperature is found to be 8940 K for acetylene, and the minimum temperature is 6699.19 K for ethylene fuel. For an equivalence

ratio of 1.5, the maximum temperature occurs at 7645.52 K for acetylene, and the minimum temperature is 6065.35 K for ethylene fuel. When all equivalence ratios are examined, it is determined that the maximum temperature belongs to acetylene fuel and the minimum temperature belongs to hydrogen fuel.

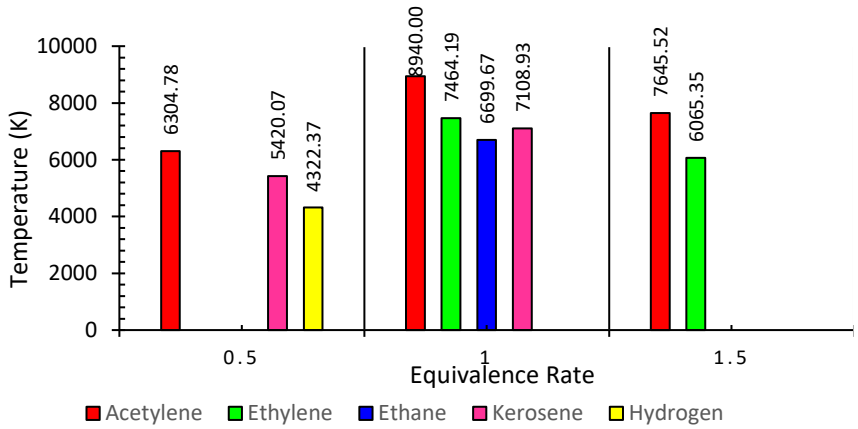

Figure 4.57. Temperature Equivalence

At an equivalence ratio of 0.5, Figure 4.58 depicts the maximum velocity for hydrogen as 1672.64 m/s, while the minimum velocity for acetylene fuel is 1059.45 m/s. At an equivalence ratio of 1, the maximum velocity is found to be 1344.36 m/s for ethane, and the minimum velocity is 1256.09 m/s for acetylene fuel. Eşdeğerlik oranı 1,5 olduğunda, etilen 1233,97 m/s'de maksimum hızı gösterirken, asetilen yakıtı 1133,51 m/s'de minimum hızı göstermektedir. Upon examination of all equivalence ratios, it is evident that acetylene fuel exhibits the lowest velocity, while hydrogen attains the highest velocity. It is observed that ethane fuel only occurs at an equivalence ratio of 1 and achieves the highest velocity among the fuels at this ratio.

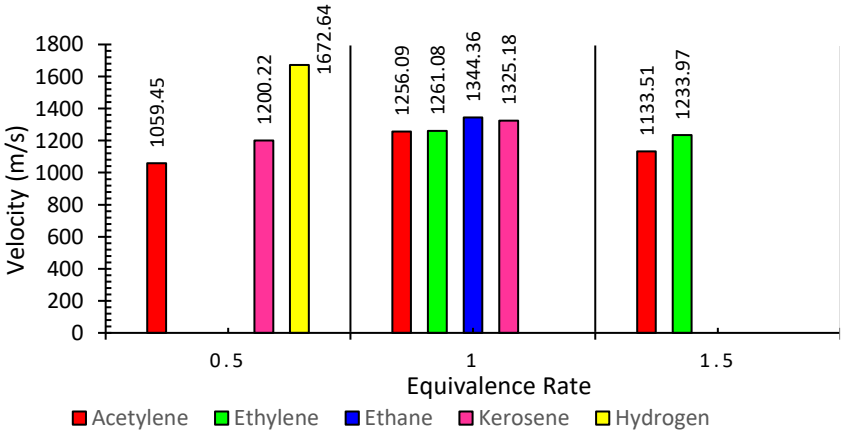

Figure 4.58. Velocity Equivalence

4.8. General Conclusions 2

The maximum pressure, temperature, and velocity values obtained at an equivalence ratio of 1. The pressure increases in a consistent manner for all obstacle heights, as can be observed in Figure 4.59. The maximum pressure occurs in kerosene fuel, while the minimum pressure is observed in acetylene fuel. The maximum pressure value for kerosene fuel is found to be 5884.21 kPa at an obstacle height of 1 mm. On the other hand, the minimum pressure value for acetylene fuel is determined to be 4180.62 kPa at an obstacle height of 1.5 mm.

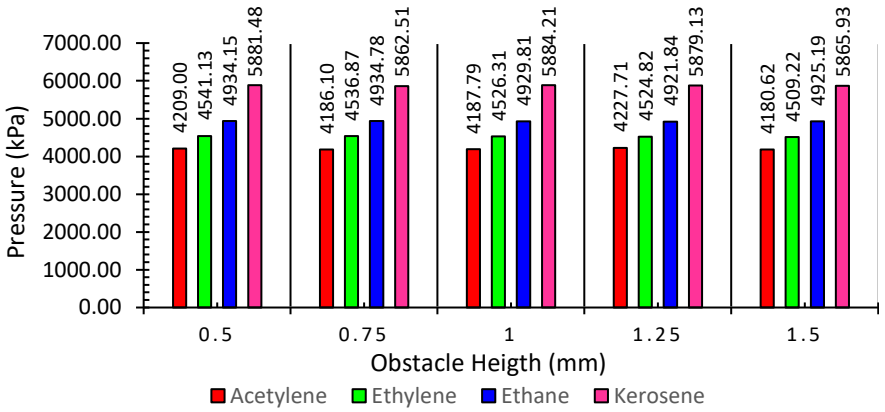

Figure 4.59. Pressure-Obstacle Height

The maximum temperature occurs in Acetylene fuel, while the minimum temperature is observed in ethane fuel. The maximum temperature value for acetylene fuel is found to be 8940 K at an obstacle height of 1.5 mm. On the other hand, the minimum temperature value for ethane fuel is determined to be 6695.30 K at an obstacle height of 1.5 mm.

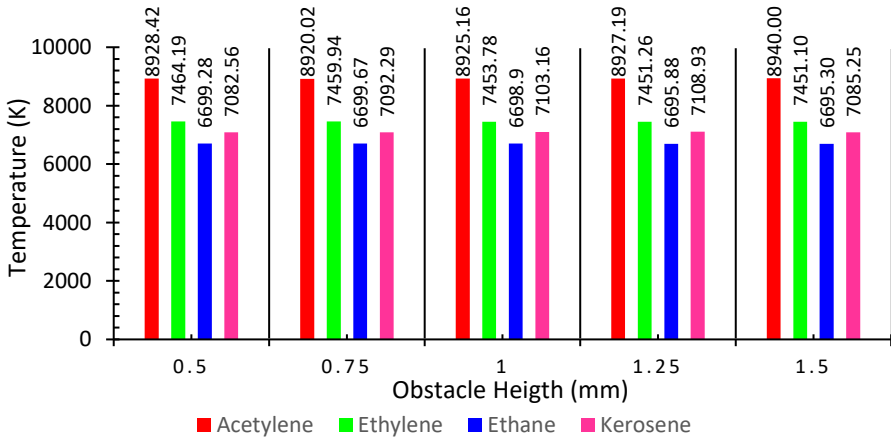

Figure 4.60. Temperature-Obstacle Height

The velocity changes for all obstacle heights follow the same pattern, as shown in Figure 4.61. The maximum velocity occurs in ethane fuel, while the minimum velocity is observed in acetylene fuel. The maximum velocity value for ethane fuel is found to be 1344.36 m/s, and the minimum velocity value for acetylene fuel is determined to be 1234.63 m/s, both at an obstacle height of 0.75 mm.

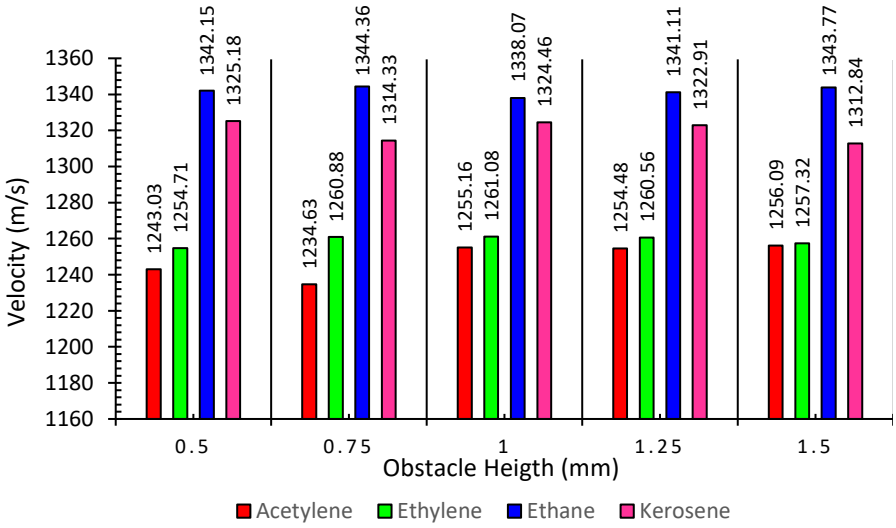

Figure 4.61. Velocity-Obstacle Height

In hydrogen fuel, a shock wave did not form at equivalence ratio 1, but at equivalence ratio 0.5, the shock wave's velocity reached a maximum of 1672.64 m/s, making it the highest velocity among all fuels. Hydrogen also reached a maximum pressure of 2103.47 kPa at an obstacle height of 0.5 mm, and its maximum temperature of 4322.37 K was observed at an obstacle height of 0.75 mm.

4.9. Main-Detonator

In this thesis, some analyses related to the main detonator have been conducted, but comprehensive studies have been deferred to the doctoral thesis. For illustrative purposes, some data related to the main detonator analyses have been shared within the scope of this thesis. In Figures 4.62 and 4.63, Kerosene-Oxygen fuel was analyzed in 2D and 3D under stoichiometric conditions. In Figure 4.64, Kerosene-Oxygen fuel was injected into the main detonator using User Defined Functions (UDF).

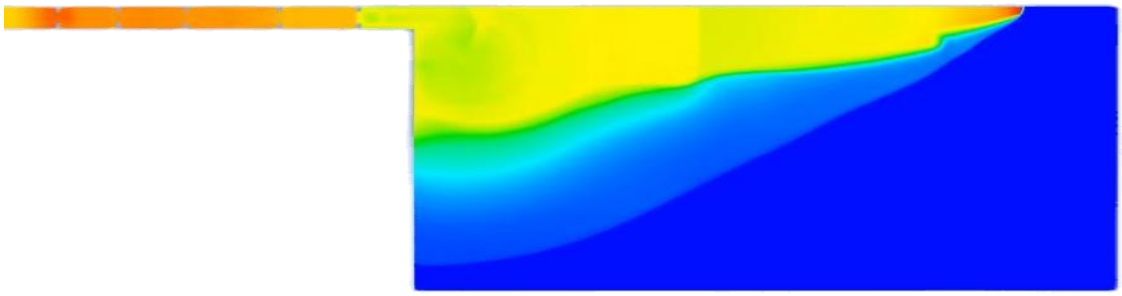

Figure 4.62. Kerosene-Oxygen Fuel Behavior in the Main-Detonator in 2D Analysis

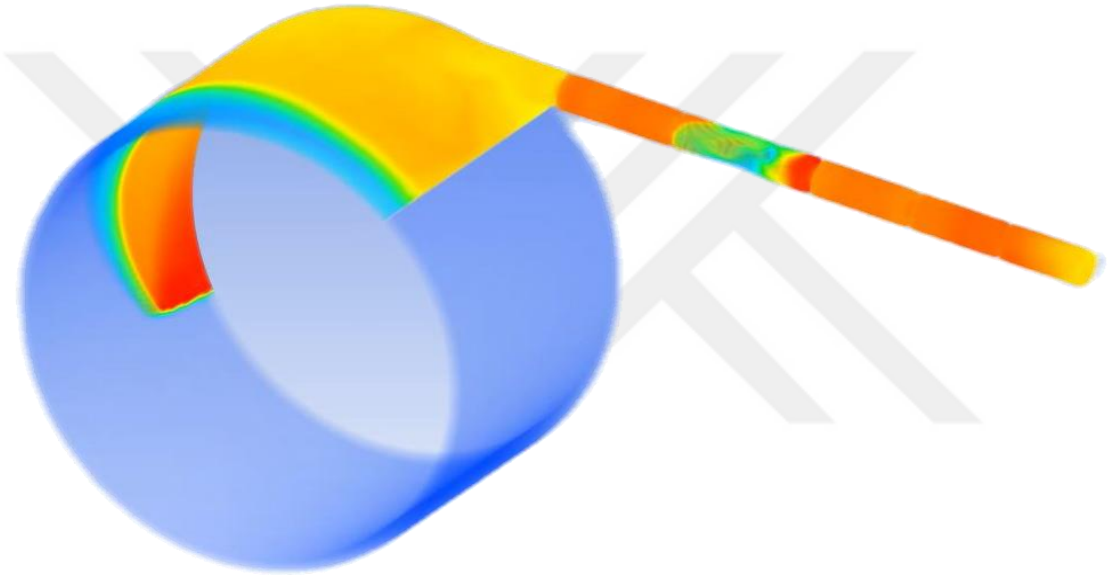

Figure 4.63. Kerosene-Oxygen Fuel Behavior in the Main-Detonator in 3D Analysis

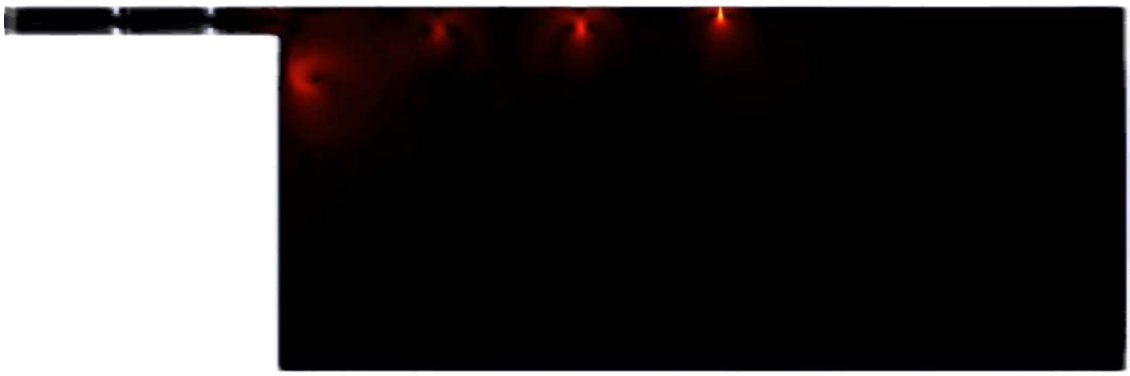

Figure 4.64. Spraying of Kerosene-Oxygen Fuel into 2D Main-Detonator with UDF

Tablo 4.25 shows the feeding of the shock wave in the 2D Main Detonator using Kerosene-Oxygen fuel with the implementation of User Defined Functions (UDF). It is essential to remember that for the continuity of the shock wave, a detailed study of the injector positions, injection rates, and opening/closing times is required. These parameters play a crucial role in the behavior of the shock wave and need to be carefully analyzed to ensure the accuracy and reliability of the results.

Table 4.25. Feeding Shock Wave in a 2D Main-Detonator with Kerosene-Oxygen Using UDF

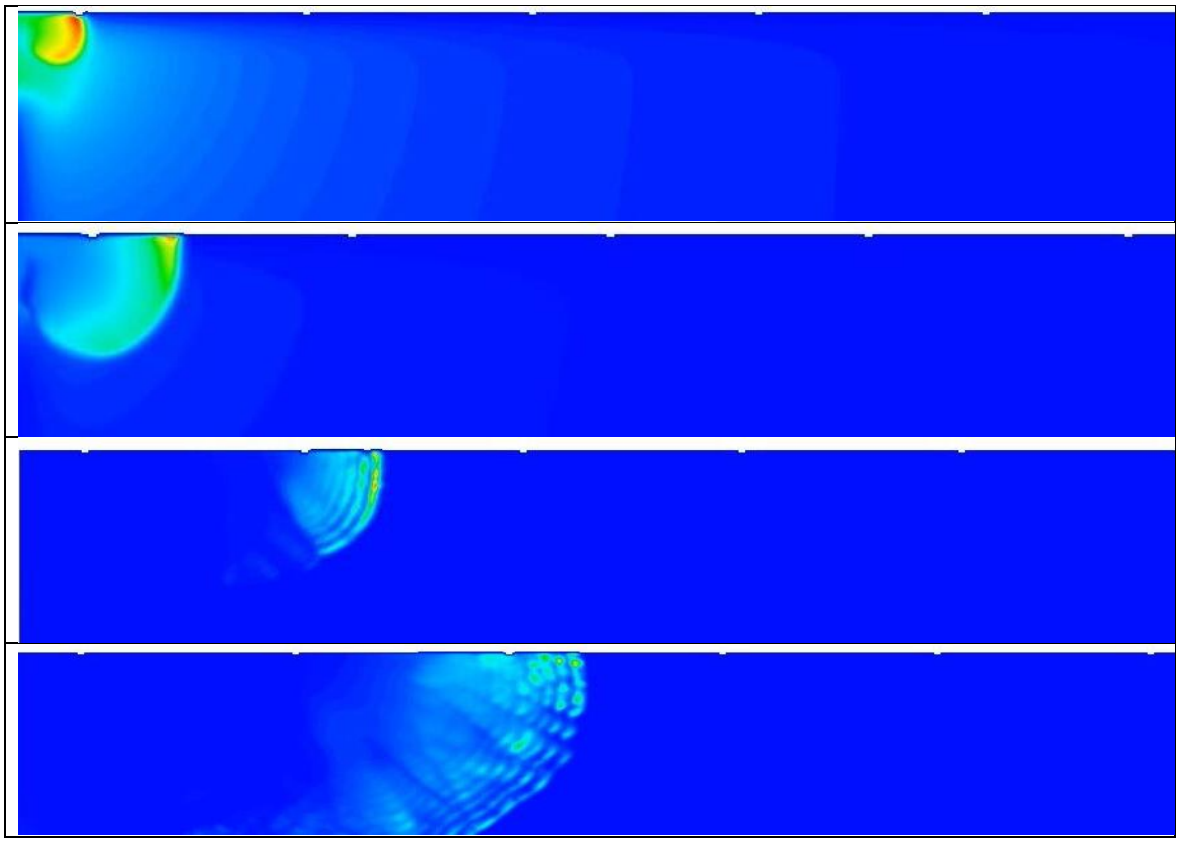

RESULTS and DISCUSSION

Within the framework of the thesis, CFD experiments were carried out for 6 different C/H ratios, 5 different blockages, and 3 different equivalency values in the pre-detonator.

The shock wave was generated firstly at 0.036 milliseconds with acetylene at equivalency 1, and it leaves the PDE 0.067 milliseconds after formation, according to an analysis of the shock wave formation times. Hydrogen at equivalence 0.5 was identified as the fastest fuel, with the shock wave departing the PDE after 0.051 milliseconds from its formation. The shock wave formed at equivalence 1.5 for Ethylene with a formation time of 1.16 milliseconds. Although the shock wave formation in Ethane at equivalence 1 took the longest time at 0.66 milliseconds, it was the second fastest among all fuels in departing the PDE after 0.057 milliseconds from its formation. The shock wave departure time from the PDE was observed to be the fastest for Acetylene and Ethylene fuels at equivalence 1, equivalence 0.5, and equivalence 1.5, respectively. For Kerosene fuel, the PDE departure time was the fastest at 0.534 milliseconds for equivalence 0.5 and the slowest at 0.656 milliseconds for equivalence 1. In the analysis results of Acetylene fuel, it was observed that there is a decrease in pressure, temperature, and velocity at non-stoichiometric equivalence ratios. At each obstacle height, Acetylene fuel exhibited minimum pressure, temperature, and velocity values. Furthermore, across all equivalence ratios, the shock wave was observed to occur between the start and the middle of the first obstacle.

In Ethylene fuel at equivalence ratio of 0.5, the presence of micro-explosions has been observed, leading to localized stresses. These micro-explosions can disrupt the shock structure and generate significant vibration loads, which should not be overlooked. For Ethylene fuel at equivalence ratios 1 and 1.5, although the shock waves formed at different times, they both left the PDE within 0.61 milliseconds. In detail, the shock wave at equivalence ratio 1 occurred right at the entrance of the first obstacle, while at equivalence ratio 1.5, it formed around the middle of the first and second obstacles. It has been determined that an increase in the equivalence ratio prolongs the shock wave formation time and the length of PDE.

In Ethane fuel, at an equivalence ratio of 0.5, the occurrence of micro-explosions was observed, and at an equivalence ratio of 1.5, no shock wave formation was detected. Although the formation of the shock wave in Ethane fuel takes longer compared to other fuels, it is the second fastest fuel to leave the PDE after the shock wave is formed. The shock

wave in Ethane fuel was found to occur right after the first obstacle. At equivalence ratio 1, maximum pressure, temperature, and velocity were reached at a 0.75 mm obstacle height. Additionally, at equivalence ratio 1, Ethane fuel exhibited the highest velocity at all obstacle heights.

It has been observed that shock waves do not occur in our geometry at various blockage rates and equivalent ratios since methane fuel is stable. The temperature, which was initially set as a patch, gradually decreased and reached equilibrium with the ambient conditions. However, when a small amount of oxygen was added to the driver section, micro-explosions occurred, leading to potentially dangerous local pressure and temperature spikes. These micro-explosions can cause vibration loads and may pose a risk to the design. Therefore, it is important to be cautious about introducing additional oxygen in this setup.

Shock waves were found not to form at an equivalency ratio of 1.5 when testing Kerosene fuel. However, at an equivalence ratio of 0.5, the shock wave occurred earlier than in stoichiometric conditions but did not leave the tube as rapidly. The maximum pressure, temperature, and velocity values were found to be consistent with stoichiometric conditions. For an equivalence ratio of 0.5, the shock wave was observed to form around the midpoints between the first and second obstacles, whereas at an equivalence ratio of 1, it formed right at the entrance of the first obstacle. Unlike ethylene, it was determined that a lower equivalence ratio prolonged the formation time of the shock wave. Maximum values for pressure and temperature were observed at all obstacle heights.

In Hydrogen fuel, shock waves were observed to occur only at an equivalence ratio of 0.5. At this equivalence ratio, additional shock waves were detected propagating in the opposite direction within the PDE at obstacle heights of 1.25 mm and 1.5 mm. For equivalence ratios of 1 and 1.5, bi-directional shock waves were observed. As the equivalence ratio increased, the bi-directional shock waves were drawn towards the left side of the PDE. It was also observed that the mutually colliding shock waves dampened each other's intensity during propagation.

It was observed that shock waves did not form at an equivalence ratio of 1.5, whereas micro-explosion trends were evident at an equivalence ratio of 0.5. Furthermore, varying obstacle heights did not result in significant differences in pressure, temperature, or velocity values. For equivalence ratios of 1, where shock waves were observed, all fuels exhibited

maximum values in pressure, temperature, and velocity. It was found that the height of the obstacles caused more differences between the fuels than the pressure.

Detonation engines have been found to produce high pressure, temperature, and velocity values in general. Higher thrust values can be achieved by expanding the high-pressure and high-temperature gas in the nozzle. However, the current material technology falls short at these high-temperature levels. Nevertheless, with the continuous advancement in material technology, it will be possible to reach these temperature levels to generate higher thrust. As a result, detonation engines will be more efficient and powerful. Introducing and adopting developing detonation engines on a global scale will propel our country forward in the fields of space and aviation. It is believed that this postgraduate thesis has contributed valuable data to the literature for future experimental studies on detonation engines. Acquiring and implementing detonation engine technology in our country will be crucial for making advancements in the fields of space and aviation.

REFERENCES

Ahumada, C., Wang, Q., & Petersen, E., (2020). Effects of unequal blockage ratio and obstacle spacing on wave speed and overpressure during flame propagation in stoichiometric H_2/O_2. *Shock Waves.*

Alam, N., Sharma, K. K., & Pandey, K. M., (2020). Numerical investigation of flame propagation in pulse detonation engine with variation of obstacle clearance. *Journal of Thermal Analysis and Calorimetry*, 140(5), 2485-2495.

An Introduction to Computational Fluid Dynamics The Finite Volume Method Second Edition H K Versteeg and W Malalasekera 186-197

Anderson, J. D., (1990). Modern Compressible Flow. McGraw-Hill, Second Edition.

Basu, S., & Miglani, A., (2016). Combustion and Heat Transfer Characteristics of Nanofluid Fuel Droplets: A Short Review. *International Journal of Heat and Mass Transfer*, 96, p. 482-503.

Besser, H. L., & Strecker, R., (1993). Overview of Boron Ducted Rocket Development. International Journal of Energetic Materials and Chemical Propulsion, 2, 133-178.

Brophy, C. M., Dvorak, W. T., Dausen, D. F., & Myers, C. B., (2012). Detonation Initiation Improvements Usin Swept-Ramp Obstacles. Orlando: 48th AIAA Aerospace Sciences Meeting.

Bussing, T., & Pappas, G., (1994). An Introduction to Pulse Detonation Engines. Nevada: AIAA 94-0263. 32nd Aerospace Sciences Meeting & Exhibit.

Bussing, T., & Pappas, G., (1994, January). An introduction to pulse detonation engines. In 32nd Aerospace Sciences Meeting and Exhibit (p. 263).

Cao, H. V., (2013). Parametric Cycle Analysis of Continuous Rotating Detonation Ejector-Augmented Rocket Engine. 49th AIAA/ASME/SAE/ASEE Joint Propulsion Conference.

Cheng, J., Zhang, B., Liu, H., & Wang, F., (2021). The precursor shock wave and flame propagation enhancement by CO_2 injection in a methane-oxygen mixture. Fuel.

Courant, R. and K. O. Friedrichs., (1967). Supersonic Flow and Shock Waves. Inter science Publishers, Inc., New York

Fickett, W. and W. C. Davis., (2001). Detonation Theory and Experiment. Dover Publications Inc.

Frolov, S. M., Aksenov, V. S., & Skripnik, A. A., (2011). Detonation Initiation in a Natural Gas-Air Mixture in a Tube with a Focusing Nozzle. Doklady Physical Chemistry, 436(1), 10-14.

Frolov, S. M., Basevich, V. Y., Aksenov, V. S., & Polikhov, S. A., (2003). Detonation Initiation by Controlled Triggering of Electric Discharges. 19(4).

Gamezo, V. N., Ogawa, T., & Oran, E. S., (2009). Deflagration-to-Detonation Transition in H_2- Air Mixtures: Effect of Blockage Ratio. Orlando: 47th AIAA Aerospace Sciences Meeting.

Ge, G., Deng, L., Ma, H., Liu, X., Jin, L., & Zhou, C., (2019). Effect of Blockage Ratio on the Existence of Multiple Waves in Rotating Detonation Engine. Acta Astronautica.

Glassman, I., & Yetter, R. A., (2008). Combustion. San Diego: Elsevier Inc.

Hayashi, A., Kimura, Y., Yamada, T., Yamada, E., Dzieminska, J., Wolański, P., Tsuboi, N., Tangirala, V., & Fujiwara, T., (2009). Sensitivity Analysis of Rotating Detonation Engine with a Detailed Reaction Model.

Kindracki, J., (2008). Badania Eksperymentalne I Symulacje Numeryczne Procesu Inicjacji Wirującej Detonacji Gazowej [Experimental Investigations and Numerical Simulations of the Gas Detonation Swirl Initiation Process]. Ph.D. Thesis (in Polish), Politechnika Warszawska, Warsaw, Poland.

Khokhlov, A. M., Austin, J. M., Pintgen, F., & Shepherd, J. E., (2004). Numerical Study of The detonation wave structure in ethylene-oxygen mixtures. Reno: AIAA 2004-792. 32nd Aerospace Sciences Meeting & Exhibit.

Konnov, A. A., (1998). Detailed Reaction Mechanism for Small Hydrocarbons Combustion. Release 0.4. http://www.homepages.vub.ac.be/~akon

Korytchenko, K., Krivosheyev, P., Dubinin, D., Lisniak, A., Afanasenko, K., Harbuz, S., Buskin, O., Nikorchuk, A., & Tsebriuk, I., (2019). Experimental Research Into the Influence of Two Spark Ignition on the Deflagration to Detonation Transition Process in a Detonation Tube. Eastern-European Journal of Enterprise Technologies.

Kumar, R., (2019). Pulsed Detonation Engine Nozzle Design and Analysis (Doctoral dissertation, The University of Texas at Arlington).

Launder, B. E., Reece, G. J., & Rodi, W., (1975). Progress in the Development of A Reynolds-Stress Turbulence Closure. *Journal of fluid mechanics,* 68(3), 537-566.

Lee, J. H. S., (1984). Dynamic Parameters of Gaseous Detonations. Annual Review of Fluid Mechanics 16, 311–336.

Lee, J. H. S., (2008). The Detonation Phenomenon. Cambridge University Press, Cambridge.

Lee, S., Conrad, C., Watts, J., Woodward, R., Pal, S., & Santoro, R., (2000). Deflagration to Detonation Transition Study Using Simultaneous Schlieren and OH Plif Images.

Liu, X.-Y., Chen, Y.-L., Yao, S.-B., & Wang, J.-P., (2019). Numerical Study of Reverse-Rotating Wave in The Hollow Rotating Detonation Engines. The Proceedings of The 2018 Asia-Pacific International Symposium on Aerospace Technology (APISAT 2018), 1677–1684.

Liu, X.-Y., Luan, M.-Y., Chen, Y.-L., & Wang, J.-P., (2020). Flow-field Analysis and Pressure Gain Estimation of a Rotating Detonation Engine with Striped Distribution of Reactants. AIAA Propulsion and Energy 2020 Forum

National Center for Biotechnology Information., (2021). PubChem compound summary.

National Center for Biotechnology Information., (2023). PubChem Compound Summary for CID 896, Ethylene.

National Center for Biotechnology Information., (2023). PubChem Compound Summary for CID 783, Hydrogen.

National Center for Biotechnology Information., (2023). PubChem Compound Summary for CID 786 Kerosene.

National Center for Biotechnology Information., (2023). PubChem Compound Summary for CID 297, Methane.

National Center for Biotechnology Information., (2023). PubChem Compound Summary for CID 6324, Ethane.

Nikitin, V., Dushin, V., Phylippov, Y., & Legros, J., (2009). Pulse detonation engines: Technical approaches. Acta Astronautica.

Panicker, P. K., (2008). The Development and Testing of Pulsed Detonation Engine Ground Demonstrators. Doctoral Dissertation, The University of Texas at Arlington.

Peng, H., Liu, W., Liu, S., Zhang, H., & Huang, S., (2020). The Competitive Relationship Between Detonation and Deflagration in the İnner Cylinder-Variable Continuous Rotating Detonation Combustor. Aerospace Science and Technology.

Rankin, B., Fotia, M., Naples, A., Stevens, C., Hoke, J., Kaemming, T., Theuerkauf, S., & Schauer, F., (2017). Overview of Performance, Application, and Analysis of Rotating Detonation Engine Technologies. *Journal of Propulsion and Power.*

Saputra, F., & Mahaputra, M. R., (2022). Building Occupational Safety and Health (K3): Analysis of the Work Environment and Work Discipline. *Journal of Law, Politic and Humanities*, 2(3), 105-114.

Simmons, F., Quigley, D., Whyte, H., Robertson, J., & Freshwater, D., (2009). Chemical safety: Asking the right questions. Journal of Chemical Health & Safety, 16(3), 34-39.

Soloukhin, R. I., (1966). Shock Waves and Detonations in Gases. Baltimore, MD: Mono Book.

Thompson, P. A., (1988). Compressible Fluid Dynamics. Advanced Engineering Series, Rensselaer Polytechnic Institute, pp. 353–354.

Thompson, P.A., (1988). Compressible Fluid Dynamics. Advanced Engineering Series, Rensselaer Polytechnic Institute, pp. 347–359.

Tsuboi, N., Asahara, M., Kojima, T., & Koichi Hayashi, A., (2017). Numerical Simulation on Rotating Detonation Engine: Effects of Higher-Order Scheme. Detonation Control for Propulsion, p. 77–107.

Wilcox, D. C., (1998). Turbulence modeling for CFD. La Canada, CA: DCW Industries. pp. 103-217.

Wintenberger & Shepherd, Thermodynamic Cycle Analysis for Propagating Detonations,. 2005.

Wintenberger, E., & Shepherd, J. E., (2006). Thermodynamic cycle analysis for propagating detonations. *Journal of propulsion and power*, 22(3), 694-698.

Wolański, P., (2021). RDE research and development in Poland. *Shock Waves*, 31(7), 623-636.

Yang, C., Wu, X., Ma, H., Peng, L., & Gao, J., (2016). Experimental Research on Initiation Characteristics of a Rotating Detonation Engine. *Experimental Thermal and Fluid Science*, 71, p. 154–163.

Zheng, H., Meng, Q., Zhao, N., Li, Z., & Deng, F., (2020). Numerical investigation on H_2/Air non-premixed rotating detonation engine under different equivalence ratios. *International Journal of Hydrogen Energy*.

RESUME

Name Surname: Mehmet Ali ADIGÜZEL

Profession: Mechanical Engineer

INTERESTS AND RESEARCH AREAS:

General Areas:	Special Topics:
Thermodynamics	Detonation Engines
Fluid Mechanics	Traditional Rocket Engines
Heat Transfer	Gas Turbine Engines
Internal Combustion Engines	Computational Fluid Dynamics
Differential Equations	Fuels and Combustion
Combustion Technique	Alternative Fuels

EDUCATION:

Degree	University	Department	Year
3.33/4	Afyon Kocatepe University	Mechanical Engineering (Undergraduate)	4
3.94/4	Tarsus University/Kielce University	Mechanical Engineering (Graduate)	2

ENGINEERING PROGRAMS EXPERIENCE

- ANSYS Fluent
- SolidWorks
- Matlab-FEA
- AutoCAD
- EES

- Microsoft Office

WORK EXPERIENCE

Polat Machinery Inc. - Intern/ Time Study September 2021 / January 2021

OKT Trailer Inc. - Intern/ Machining June 2020 / August 2020

Savrukoğlu Agricultural Machinery Inc. - Intern/ Machining June 2019 / August2019

LANGUAGE SKILLS

English: Professional Working Proficiency (B2+)

Turkish: Native speaker

PUBLICATIONS

Master Thesis:

The Impact of Changing Obstacle Sizes On Shock Wave Generation For Various Fuel Types In Detonation Engines

Article:

Yontar, A. A., Üstün, D., Özgüner, A. G., and Adıgüzel, M. A., 2022, '' Combustion Characteristics of Trimethyl Borate, Diesel, and Trimethly Borate-Diesel Blend Droplets.'', Journal of the Energy Institute 2022.

Conferences:

Yontar, A. A. and Adıgüzel, M. A., 2022, '' Investigation of the Effect of Fuels with Different Hydrogen-Carbon Ratios on Shock Wave in Pre-Detonator of Rockets with Detonation Engine.'', INCOS2022, 16th National Combustion Symposium, September 08-11, Aydın, Turkey.

Yontar, A. A. and Adıgüzel, M. A., 2022, '' "Investigation of the Effect of Obstacles on Shock Wave in Pre-Detonator of Rockets with Detonation Engine.'', UHUK2022, 9th National Aviation and Space Conference, September 14-16, Izmir, Turkey.

Yontar, A. A., Adıgüzel, M. A., and Özgüner A.G, 2023, '' Investigation of the Effect of Equivalence Ratio on Shock Wave in Kerosene Fuel in Pre-Detonator.", AIAC2023, 12th Ankara International Aerospace Conference., 13-15 September 2023- METU, Ankara Turkey

Environmental and Energy Technologies FINALIST

❖To lead the computer-aided calculation, computer-aided design, and production of Turkey's first micro jet engine capable of generating 124 N of force, which was produced using our own organaBORon and benefiting from the training of the Aviation Engines School of TEI, in the field of environmental and energy technologies at Teknofest.

Second Place in Technology Faculty

❖Afyon Kocatepe University Faculty of Mechanical Engineering and Technology, second place and awarded with honor certificate.

Undergraduate Thesis

❖ Modeling and Control of a Turbojet Engine for Anka-S Model

Certificates

❖Aerospace Engines School, TEI-TUSAS Engine Industry Inc., TEI Academy **12.02.2022-04.06.2022**
❖ANSYS Fluent-CFD Analysis Engineer Training, Engineering Academy **Mar 2020-Jul 2020**
❖MS-Excel-Basic/Intermediate/Advanced All Levels, Engineering Academy **Sep 2020-Jan 2020**
❖Ansys Workbench-Analysis Engineer Training, Engineering Academy **Jan 2020-Sep 2020**
❖Introduction to ANSYS SpaceClaim (Fluids), NUMESYS, **Feb 2023-Mar 2023**
❖ANSYS Fluent Meshing, NUMESYS, **Feb 2023-Mar 2023**
❖Introduction to ANSYS Fluent, NUMESYS, **Feb 2023-Mar 2023**
❖Ansys Meshing, NUMESYS, **Feb 2023-Mar 2023**

References

❖Assoc. Prof. Dr. Ahmet Alper YONTAR, +90 (324) 600 0033, aayontar@tarsus.edu.tr, Tarsus University

❖Assoc. Prof. Dr. Ceyhun Yılmaz, +90(272) 228 1446, ceyhunyilmaz16@gmail.com, Afyon Kocatepe University.

Hobbies: Writing Poetry, Reading Books, Hiking in Nature, and Amateur Mountaineering.

Please visit my LinkedIn profile to learn more about my work: https://www.linkedin.com/in/mehmet-ali-ad%C4%B1g%C3%BCzel-12a78a1a1/

APPENDIX

Appendix 1. Detonation Rates for Various Premixed Gases at 1atm and 25°C

Mixture	Detonation velocity (m/s)
Stoichiometric H_2–O_2	2840
Stoichiometric H_2–air	1970
1.12 Stoichiometric H_2–O_2	3390
0.37 Stoichiometric H_2–O_2	1760
Stoichiometric CH_4–O_2	2320
Stoichiometric CH_4–air	1800
1.5 Stoichiometric CH_4–O_2	2530
1.2 Stoichiometric CH_4–O_2	2470
Stoichiometric C_2H_2–air	1870
Stoichiometric C_2H_2–O_2	2430
Stoichiometric CO–O_2	1800
Stoichiometric C_3H_8–O_2	2350
Stoichiometric C_3H_8–air	1800

Appendix 2. Detonation Characteristics Calculated for Various Gas Mixtures at 1atm and 25°C

Reactants							
Fuel (1 mol)	C_2H_2	C_2H_2	CO	H_2	H_2	CH_4	C_3H_8
O_2 (mol)	2.5	2.5	0.5	0.5	0.5	2	5
N_2 (mol)	0	9.32	0	0	1.88	7.52	18.8
Detonation Products (Mole fraction)							
CO_2	0.0930	0.0880	0.4033	0	0	0.0696	0.0836
H_2O	0.0872	0.0615	0	0.5304	0.2943	0.1721	0.1384
O_2	0.1167	0.0221	0.1659	0.0486	0.0078	0.0098	0.0116
CO	0.3463	0.0660	0.3813	0	0	0.0235	0.0300
OH	0.1157	0.0146	0	0.1370	0.0183	0.0097	0.0099
O	0.1288	0.0056	0.0495	0.0386	0.0021	0.0012	0.0015
H	0.0746	0.0039	0	0.0811	0.0060	0.0017	0.0017
NO	0	0.0169	0	0	0.0078	0.0072	0.0085
H_2	0.0370	0.0062	0	0.1641	0.0317	0.0085	0.0072
N_2	0	0.7152	0	0	0.6319	0.6967	0.7076
Detonation Parameters							
V_D (m/s)	2425	1867	1799	2841	1971	1804	1801
Ma_D	7.36	5.41	5.24	5.28	4.84	5.11	5.31
T_{prod} (K)	4214	3113	3525	3682	2949	2780	2823
ρ_{prod} / ρ_{react}	33.87	19.13	13.98	18.85	15.62	17.20	18.27
γ_{prod}	1.152	1.157	1.125	1.129	1.163	1.169	1.166
a_{prod} (m/s)	1317	1027	977	1545	1092	999	994
M_{prod}	23.3	28.4	34.5	14.5	23.9	27.0	27.7

Appendix 3. Calorific Values of Some Typical Fuels at 1atm and 25°C

	HHV		LHV	
Fuel	**(MJ/m³)***	**MJ/kg**	**(MJ/m³)***	**MJ/kg**
Hydrogen (H_2)	11.7	142.2	9.9	121.2
Carbon monoxide (CO)	11.6	10.1	11.6	10.1
Methane (CH_4)	36.4	55.5	32.8	50.0
Ethane (C_2H_6)	63.8	51.9	58.4	47.8
Propane C_3H_8)	90.8	50.4	83.6	46.4
Butane (C_4H_{10})	117	49.5	108	45.8
Ethylene (C_2H_4)	57.7	50.3	54.1	47.2
Acetylene (C_2H_2)	53.2	49.9	51.4	48.2
Propylene (C_3H_6)	84.2	48.9	78.8	45.8
Natural gas (typical)	38.3	53.5	34.6	48.3
Coal producer gas (typical)	5.2	5.3	4.3	4.4
Wood producer gas (typical)	4.8	5.1	4.0	4.2

Source: Soloukhin,1996.

Example

A large volume contains a stoichiometric mixture of Acetylene and Oxygen at 1 atm and 25°C. Using the data provided in Supplementary Table 1, approximate values for the pressure, temperature, and gas velocity immediately behind the detonation wave can be calculated.

Solution

The stoichiometric equilibrium equation for the Acetylene-Oxygen reaction is

$$C_2H_2+2.5O_2 \longrightarrow 2CO_2+H_2O$$

Hence, the molecular weight of a stoichiometric methane-air mixture

$$M_{react} = \frac{\left[\frac{1kgmol_{C2H2}}{1}\cdot\frac{26kg_{C2H2}}{kgmol_{C2H2}} + \frac{5kgmol_{C2H2}}{1}\cdot\frac{32kg_{O2}}{kgmol_{O2}}\right]}{3kgmol_{react}}$$

$$M_{react} = 62\ kg/kgmol$$

If we extract the velocity of the detonation wave velocity for Acetylene-Oxygen from Appendix Table 1

$$V_D=V_{react}=2430m/s$$

Calculate the speed of sound of reactants

$$a_{react} = (\gamma R_{react} T_{react})^{\frac{1}{2}} = \left[1.4\left(\frac{8314kg.m^2}{kgmol.K.s^2}\cdot\frac{kgmol}{62kg}\right)(298K)\right]^{\frac{1}{2}}$$

$$a_{react} = 236.6 m/s$$

And Mach number

$$Ma_{react} = \frac{2430}{236.6}$$

$$Ma_{react} = 10.27$$

From equations (2.17) and (2.19),

$$\frac{P_{prod}}{P_{react}} = \frac{\gamma Ma_{react}^2 + 1}{\gamma + 1} = \frac{1.4(10.27)^2 + 1}{1.4 + 1} = 61.94$$

$$P_{prod} = 1(61.94) = 61.94\ atm$$

$$\frac{T_{prod}}{T_{react}} = \frac{(1 + \gamma Ma_{react}^2)^2}{(\gamma + 1)^2 Ma_{react}^2} = \frac{(1 + 1.4(10.27)^2)^2}{(1.4 + 1)^2 (10.27)^2} = 36.38$$

$$T_{prod} = 298(36.38) = 10841.24K$$

$$a_{prod} = (\gamma R_{react} T_{react})^{\frac{1}{2}} = \left[1.4\left(\frac{8314 kg.m^2}{kgmol.K.s^2} \cdot \frac{kgmol}{62kg}\right)(10841.24K)\right]^{\frac{1}{2}}$$

$$a_{prod} = 1426.6\ m/s$$

Now let's calculate the velocity behind the detonation at room conditions using the Chapman-Jouguet condition

$V_{prod}=V_D-a_{prod}=2430-1426.6=1003.4 m/s$

Mach number of the wave at room conditions

$$Ma_{prod} = \frac{1003.4 m/s}{2430 m/s}$$

$$Ma_{prod} = 0.413$$

Let's solve the same question using the lower calorific value of acetylene and compare the results.

Appendix Table 3 shows that the lower calorific value of acetylene is 48.2 MJ/kg. The stoichiometric equilibrium equation for the acetylene-oxygen reaction is as follows

$$C_2H_2+2.5O_2 \longrightarrow 2CO_2+H_2O$$

Estimated heat release

$$\frac{q}{\dot{m}} = \frac{48.2MJ}{kg_{C2H2}} \cdot \frac{26kg_{C2H2}}{(26+2(32))kg_{react}}$$

$$\frac{q}{\dot{m}} = 13924kj/kg_{react}$$

Equation (2.20) ve $\gamma = 1.4$ ve $C_{p,react}$ =1.0kj/kgK

$$Ma_{react} = [\frac{2(\gamma+1)}{C_pT_1}(\frac{q}{\dot{m}})]^{\frac{1}{2}} = [\frac{2(1.4+1)}{\left(\frac{1.0kj}{kgK}\right)298K}(13924)]^{\frac{1}{2}}$$

$$Ma_{react} = 14.98$$

Let's calculate the Mach number for the stoichiometric Acetylene fuel as performed in the thesis. If we use the pressure ratio, we can find the average pressure from Table 4.1 as 4227.71 kPa. By applying Equation (2.17), we can calculate the Mach number.

$$Ma_{react} = \left[\frac{\left(\left(\frac{P_{prod}}{P_{react}}\right)(\gamma+1)-1\right)}{\gamma}\right]^{\frac{1}{2}} = \left[\frac{\left(\left(\frac{4227.71}{101.325}\right)(1.4+1)-1\right)}{1.4}\right]^{\frac{1}{2}}$$

$$Ma_{react} = 8.42$$

In Appendix Table 2 the experimental value of Ma_D (detonation Mach number) was measured as 7.36. In our initial calculations, we obtained a Mach number of 10.27 using the specific heat ratio (γ) and 14.98 from the lower calorific value. However, when we calculated the Mach number using the data obtained from the analyses conducted in the thesis, we obtained a value of 8.42. The high error rate among the Mach numbers can be attributed to assumptions made, such as constant specific heat ratio (γ) and constant molecular weights, as well as heat release and product dissociation effects. Among all these solutions, the CFD results obtained in the thesis showed the closest match to the experimental data with an error rate of 12.6%. Although the explosion model calculated using constant specific heat release overestimated the explosion Mach number, it still provided accurate trends.

Appendix 4. File Creation Code

```
# encoding: utf-8

# Release []

SetScriptVersion(Version="[]")

Open(FilePath="[]")

Extensions.UnloadExtension(

Id="5e7e01a6-8601-11e8-9f8c-28f10e13ffe6",

Version="1.3",

Format="Binary")

designPoint1 = Parameters.GetDesignPoint(Name="0")

parameter1 = Parameters.GetParameter(Name="P1")

designPoint1.SetParameterExpression(

Parameter=parameter1,

Expression="[1]")

parameter2 = Parameters.GetParameter(Name="P2")

designPoint1.SetParameterExpression(

Parameter=parameter2,

Expression="[2]")

parameter3 = Parameters.GetParameter(Name="P3")

designPoint1.SetParameterExpression(

Parameter=parameter3,

Expression="[3]")

parameter4 = Parameters.GetParameter(Name="P4")

designPoint1.SetParameterExpression(

Parameter=parameter4,
```

```
Expression="[4]")
parameter5 = Parameters.GetParameter(Name="P5")
designPoint1.SetParameterExpression(
Parameter=parameter5,
Expression="[5]")
parameter6 = Parameters.GetParameter(Name="P6")
designPoint1.SetParameterExpression(
Parameter=parameter6,
Expression="[6]")
parameter7 = Parameters.GetParameter(Name="P7")
designPoint1.SetParameterExpression(
Parameter=parameter7,
Expression="[7]")
parameter8 = Parameters.GetParameter(Name="P8")
designPoint1.SetParameterExpression(
Parameter=parameter8,
Expression="[8]")
backgroundSession1 = UpdateAllDesignPoints(DesignPoints=[designPoint1])
Parameters.ExportAllDesignPointsData(FilePath="[]")
Save(
FilePath="[]",
```

Appendix 5. Integrated Code

```
tic
clc; clear;
%% Parameters
1=[];
2=[];
3=[];
4=[];
5=[];
6=[];
7=[];
8=[];
%% Create new journal
fid=fopen('base journal.wbjn','r');
f=fread(fid,'*char')';
fclose(fid);
f=strrep(f,'1',num2str(1));
f=strrep(f,'2',num2str(2));
f=strrep(f,'3',num2str(3));
f=strrep(f,'4',num2str(4));
f=strrep(f,'5',num2str(5));
f=strrep(f,'6',num2str(6));
f=strrep(f,'7',num2str(7));
f=strrep(f,'8',num2str(8));
fid=fopen('finaljournal.wbjn','w');
fprintf(fid,'%s',f);
fclose(fid);
%% Calculate Parameters
system('');
```

```
%% Output
Pressure=xlsread('export data.csv',' ',' ');
toc
```

Appendix 6. Fuel Spray Code Using Square Wave Function

```
/* velocity with time as  square wave*/

#include "udf.h"

DEFINE_PROFILE(inlet_1, ft, var)

{

real flow_time;

face_t f;

flow_time = CURRENT_TIME;

begin_f_loop(f, ft)

{

while(flow_time>[])

flow_time=flow_time-[];

if(flow_time<[])

F_PROFILE(f, ft, var) = [];

else

F_PROFILE(f, ft, var) = [];

}

end_f_loop(f, ft)

}

DEFINE_PROFILE(inlet_2, ft, var)

{

real flow_time;

face_t f;

flow_time =CURRENT_TIME;

begin_f_loop(f, ft)
```

```
{
while(flow_time>[])
flow_time=flow_time-[];
if(flow_time<[])
F_PROFILE(f, ft, var) = [];
else
F_PROFILE(f, ft, var) = [];
if(flow_time>[])
F_PROFILE(f, ft, var) = 0;
}
end_f_loop(f, ft)
}
DEFINE_PROFILE(inlet_3, ft, var)
{
real flow_time;
face_t f;
flow_time =CURRENT_TIME;
begin_f_loop(f, ft)
{
while(flow_time>[])
flow_time=flow_time-[];
if(flow_time<[])
F_PROFILE(f, ft, var) = [];
Else
F_PROFILE(f, ft, var) = [];
```

```
if(flow_time>[])

F_PROFILE(f, ft, var) = [];

}

end_f_loop(f, ft)

}
```